Universidade de Aveiro Departamento de Física
2011

Pedro Manuel
Parracho Salomé

Filmes Calcogenetos para células solares: Crescimento e Propriedades

Chalcogenide Thin Films for Solar Cells: Growth and Properties

Universidade de Aveiro Departamento de Física
2011

Pedro Manuel
Parracho Salomé

Filmes Calcogenetos para células solares: Crescimento e Propriedades

Chalcogenide Thin Films for Solar Cells: Growth and Properties

Dissertação apresentada à Universidade de Aveiro para cumprimento dos requisitos necessários à obtenção do grau de Doutor em Física, realizada sob a orientação científica do Doutor António F. da Cunha, Professor Auxiliar do Departamento de Física da Universidade de Aveiro.

24/01/2011

Apoio financeiro da FCT - POPH/FSE

There's no certainty - only opportunity.
V, 2006

o júri

presidente

Prof. Doutor José Joaquim de Almeida Grácio
professor catedrático da Universidade de Aveiro

Prof. Doutor António Manuel Barros Gomes de Vallêra
professor catedrádico aposentado da Faculdade de Ciências da Universidade de Lisboa

Prof. Doutor Alessandro Romeo
assistant professor, Faculty of Science, University of Verona

Prof. Doutor Hugo Manuel Brito Águas
professor auxiliar da Faculdade de Ciências da Universidade Nova de Lisboa

Prof. Doutor Antonio Ferreira da Cunha
professor auxiliar da Universidade de Aveiro

acknowledgements

I would like to thank Professor António F. da Cunha for accepting me to be his student and for his teachings. I also would like to thank Professor Celeste do Carmo for encouraging me to continue my studies and for accepting me in the I3N as a Ph.D. student.

I acknowledge and appreciate the acceptance of Professor António Vallêra, Professor Hugo Águas and Professor Alessandro Romeo for being part of the jury of this thesis.

I have to thank several people for their technical and social support: Eng.ª Marta Ferro for the help with SEM; Doctor Rosário Soares for the help with the XRD measurements; Professor Rosário Correia for being always available to help dealing with the Raman system and the talks about the institution and life in general; António Fernandes for the help with the Raman system; Miguel Rocha and Ivo Mateus for the technical help in the workshop; Professor Juan Gonzales for the talks, the support and the measurements done in Minas Gerais; Professor Joaquim Leitão for the PL measurements and for listening to my usual disagreements regarding the decay of the institution as a team; Doctor Alfons Weber, Ing. Björn Schubert and Christiane Stephan for receiving me in Berlin and for the comradeship; Professor Armando Lourenço for the good company in the laboratory; Emanuel Santos for the help with some images and the good coffee at FISUA; Francisco Reis for the help with IT; last but not the least, all my laboratory colleagues during the time of work that lead to this thesis: Fábio Vinagre, Catarina Cardoso, Gabriela Cardoso, Isabel Fernandes, Paulo Fernandes, André Sartori, João Malaquias, Mário Lima and Marta Ferreira.

My mother, my father and my São-Marcos family including my sister for supporting me in the good and in the bad days.

FCT and Fundação Gulbenkian for the financial support.

Many others could be mentioned, for those a sincere thank you.

Above all, thank you Ana for your warmth and love. Without you, I would have struggled much more to keep going. You listened patiently when was needed, talked harsh when was needed, proofread part of this thesis but most importantly always stayed on my side. Having you makes it all worthwhile.

Finally, a special thank you for the I3N, the University and the Physics department secretariat for not letting this adventure going without the joy of all the administrative stuff.

keywords

Solar cells, thin films, chalcogenides, Cu(In,Ga)Se_2, CIGS, $Cu_2ZnSnSe_4$, CZTSe, $Cu_2ZnSn(S,Se)_4$, CZT(S,Se), hybrid system, growth and characterization of semiconductors.

abstract

Thin film solar cells have in recent years gained market quota against traditional silicon photovoltaic panels. These developments were in a large part due to CdTe solar panels on whose development started earlier than their competitors. Panels based on Cu(In,Ga)Se_2 (CIGS), despite being more efficient in a laboratory and industrial scale than the CdTe ones, still need a growth technology cheaper and easier to apply in industry. Although usually presented as a good candidate to make cheap panels, CIGS uses rare and expensive materials as In and Ga. The price evolution of these materials might jeopardize CIGS future.

This thesis presents three different studies. The first is the study of different processes for the incorporation of Ga in a hybrid CIGS growth system. This system is based on sputtering and thermal evaporation. This technology is, in principle, easier to be applied in the industry and solar cells with efficiencies around to 7% were fully made in Aveiro.

In the second part of this thesis, a new material to replace CIGS in thin film solar cells is studied. The growth conditions and fundamental properties of $Cu_2ZnSnSe_4$ (CZTSe) were studied in depth. Suitable conditions of temperature and pressure for the growth of this material are reported. Its band gap energy was estimated at 1.05 eV and the Raman scattering peaks were identified. Solar cells made with this material showed efficiencies lower than 0.1%.

Finally, preliminary work regarding the incorporation of selenium in Cu_2ZnSnS_4 (CZTS) thin films was carried out. The structural and morphological properties of thin films of $Cu_2ZnSn(S,Se)_4$ have been studied and the results show that the incorporation of selenium is higher in films with precursors rather with already formed Cu_2SnS_3 or Cu_2ZnSnS_4 thin films. A solar cell with 0.9 % of efficiency was prepared.

palavras-chave

Células solares, filmes finos, calcogenetos Cu(In,Ga)Se_2, CIGS, $Cu_2ZnSnSe_4$, CZTSe, $Cu_2ZnSn(S,Se)_4$, CZTSSe, crescimento e caracterização de filmes finos.

resumo

As células solares de filmes finos têm nos últimos anos ganho cota de mercado aos tradicionais painéis fotovoltaicos de Silício. Estes desenvolvimentos devem-se em grande parte ao painéis baseados em CdTe cujo desenvolvimento começou mais cedo que os seus competidores. Os painéis baseados em Cu(In,Ga)Se_2 (CIGS), apesar de serem mais eficientes tanto numa escala industrial como em laboratório, necessitam de uma tecnologia de crescimento que seja barata e de fácil aplicação na indústria. Apesar de se apresentarem como um bom candidato para painéis baratos o CIGS usa materiais caros e raros na crosta terrestre como o In e o Ga. A evolução do preço destes materiais podem comprometer o seu futuro.

Nesta tese são apresentados três estudos diferentes. O primeiro é o estudo de diferentes processos de incorporação de Ga em CIGS crescido por um sistema híbrido de pulverização catódica e evaporação térmica. Esta tecnologia é, em princípio, mais fácil de ser aplicada a nível industrial e células solares feitas em Aveiro com eficiências próximas dos 7% foram produzidas.

Numa segunda parte, outro material cujas propriedades o aponta como possível substituto ao CIGS é estudado. As condições de crescimento e propriedades fundamentais do $Cu_2ZnSnSe_4$ (CZTSe) foram estudados. São apresentadas condições de temperatura e de pressão para o crescimento reprodutível deste material. O seu hiato energético foi estimado em 1.05 eV e descobriu-se que podem existir flutuações de bandas de potencial que influenciam as suas propriedades ópticas. As células preparadas com CZTSe mostraram eficiências baixas, inferiores a 0.1%

Finalmente uma abordagem inicial à incorporação de Selénio em filmes finos de Cu_2ZnSnS_4 é feita. As propriedades estruturais e morfológicas de filmes finos de $Cu_2ZnSn(S,Se)_4$ foram estudadas e os resultados mostram que a incorporação de Selénio é maior em filmes precursores do que directamente em filmes finos de Cu_2SnS_3 ou Cu_2ZnSnS_4. Uma célula solar com eficiência de conversão de 0.9 % foi preparada.

Contents

List of abbreviations and symbols

Symbol	Explanation
α	absorption coefficient (cm^{-1})
ζ_A	quasi electric field in CIGS graded films
A	ideal diode factor of a solar cell
AFM	atomic force microscopy
AM1.5	standard terrestrial solar spectrum ‘Air Mass 1.5’
CBD	chemical bath deposition
CIS	tetragonal $CuInSe_2$
CIGS	tetragonal $Cu(In,Ga)Se_2$
CTS	tetragonal Cu_2SnS_3
CTSe	cubic Cu_2SnSe_3
CZTS	tetragonal Cu_2ZnSnS_4
CZTSe	tetragonal $Cu_2ZnSnSe_4$
CZTSSe	tetragonal $Cu_2ZnSn(S,Se)_4$
EDS	energy dispersive spectroscopy
E_g	band gap energy (eV)
EPD	end point detection
ETH	Swiss federal institute of technology Zurich
FWHM	full width at half maximum
GI-XRD	gracing-incident X-ray diffraction
HZB	Helmholtz-Zentrum Berlin für Materialien und Energie
ICP-MS	inductively coupled plasma mass spectrometry
ITO	tin doped indium oxide In_2O_3:Sn
j_0	saturation current
j	electrical current
j_{sc}	short circuit current
N_a	concentration of acceptors (cm^{-3})
N_d	concentration of donors (cm^{-3})

n_r	refractive index
PV	photovoltaic
PID	proportional–integral–derivative
q	electron charge
SLG	soda lime glass
SEM	scanning electron microscopy
TCO	transparent conductive oxide
V	voltage
V_{oc}	open circuit voltage (V)
XPS	X-ray photoelectron spectroscopy
XRD	X-ray diffraction
W_p	"peak Watt" is the rating is the power (in Watts) produced by a solar module illuminated under the following standard AIM 1.5 conditions
W_D	depletion width
W_{Dp}	depletion width of a junction in a p-type semiconductor
W_{Dn}	depletion width of a junction in an n-type semiconductor
ZGO	gallium doped zinc oxide – ZnO:Ga

Units

°C	degree Celsius
Å	Ångstrom
A	Ampere
eV	electron volt
GW	gigawatt
MW	megaWatt
MW/yr	megaWatt per year
Nm	nanometer
s	second
TW	terawatt
W	watt
Wp	peak watt
Yr	year

Unit conversions

Energy	1 eV =1.6022 x 10^{-19} J
	1 eV =1280 mm
	1 cm^{-1} ≈ 8 meV
Flow	1 sccm = 1 ml/min (milliliter/minute)
Length	1 Å = 0.1 nm (nanometer) = 1×10^{-10} m (meter)
Pressure	1 Torr = 133.3224 Pa (Pascal) = 1.333224 mbar (milibar)
	1 kgf/mm^2 = 9.807 x 10^6 Pa
Temperature	0 º C (degrees Celsius) = 273.15 K (Kelvin)

1 Introduction

1.1 The world's ever increasing demand for energy

The world we live in is hungry for more and more energy. Economical, social and humanitarian reasons lead to an increase in energy consumption worldwide. Most of the energy used nowadays is coming from polluting and limited fossil fuels. There is an evident group of problems concerning pollution and shortage of resources that will get even worse in the near future if nothing changes in the energy supply systems. Not only the demand for energy is increasing, both in developed and developing countries, but also the reserves of some fuels, such as oil [1] and uranium [1] are limited and scarce when comparing with the actual consuption. Oil, for instance, is located in limited regions of the planet, and its consumption causes the green house effect through the CO_2 emission. Its location, already verified by historic events, can cause wars and tensions among countries. In addition, the emission of more CO_2 into the atmosphere can cause irreparable damages to the world climate. The dependency on limited resources has already started to trigger huge changes in the way of living. If these facts were not enough to raise awareness that swift measures have to be taken to tackle the issue of limited resources, the world's wealth is not equally spread across the population. In fact, in the beginning of the 21st century there are still people facing death by hunger mainly in developing countries in Africa. For these people, basic conditions like affordable electricity could improve their life immeasurably.

Some countries have expressed concerns over these facts and several renewable energy and energy efficiency measures have started to be put into action in order to foster their implementation and exploitation. Recently in the Copenhagen Climate Conference 2009, a minor agreement has been reached to set reduction targets in CO_2 emissions. Although this agreement is noble, it is simply a decision and not a solution, the way to do it is unclear and uncertain. Efficiency energy actions are limited and the forthcoming actions leave the major changes to be taken by renewable energy.

Renewable energy sources depend on nature and cannot be switched on at any desired time. They depend on solar insulation and wind for instance. Therefore, it is more likely to have electricity derived from renewable energy sources if there are several types in use. In the case of solar energy, for example, the energy that arrives at the earth's surface during one hour, 4.3×10^{20} J, is greater than the world's consumption during one year, 4.1×10^{20} J [2]. This energy is spread around the earth's surface, it is dependent on the weather and varies during the day. Despite this supply variation problem, photovoltaic (PV) technologies can play a major role among the different production systems that renewable energy needs in order to be a solid solution for production of electricity.

1.2 Evolution of photovoltaics and its market

A PV module is an array of solar cells connected in series and/or in parallel. In general terms, a solar cell is a device that converts light into electricity. The PV effect is known since 1839 and was discovered by Edmund Becquerel [3] who observed that when illuminated, a silver coated platinum electrode immersed in an electrolyte, produced an electric current. The first "modern" solar cell was made of silicon and was produced at Bell Laboratories in 1954 [4] with an efficiency of conversion of light into electricity around 6%. In the years following the first silicon solar cell, namely in the 1960s, solar cells started to be used to power up communication satellites [5] making it a real "*space technology*". With the energy crisis of the 1970s they started to be used to produce electricity in remote areas on earth and, since then, have been seen as a clean and renewable energy source. Typical turn-key PV systems prices have decreased from 30 €/Wp to 3-4 €/Wp [6]. With some feed-in tariffs, PV is now affordable in home systems connected to the electrical grid and it is a competitive solution for off grid systems [7]. As a reference, the actual price of installation for off-shore wind energy is around 5 €/Wp.

Since 2005 the PV market is seen as a billion dollar business (it passed a market sales value of 1000 million US dollars) [8] and in 2008 almost 8 GW were sold [8]. In 2008, out of the total PV panels production, 75 % were panels based on crystalline silicon [9] while the rest were thin films. Crystalline silicon solar cells can be of two types, mono-crystalline and poly-crystalline silicon. In spite of their different growth methods, they both require expensive solar grade silicon and they share the same production line to make cells and panels. So, although they may not have similar efficiency values, most of the production line is shared and therefore their price is correlated. In 2006 more than 50% of silicon wafers produced were used as solar cells and that value continued to grow, meaning that the solar industry is taking the lead in the material use from the multi-billion dollar micro electronic industry.

1.3 Different types of solar cells

Because silicon is an indirect band gap semiconductor, its absorption coefficient is relatively low, around 10^3 cm^{-1}, and therefore a thick absorber layer around 160 μm is required. This fact and its costly preparation methods, like the Czochralski method, make silicon an expensive material for solar cell applications. The first modern thin film solar cell was made in 1963 and was based in a junction of CdTe/CdS already with an efficiency close to 7.5 % [10]. Earlier, in the 1950s, the photoconductivity of CdTe was presented along with some optoelectronic devices [11-13]. Since then much has improved and in the recent years photovoltaic modules using thin films have been affirming themselves with several industrial initiatives. There are several types of thin film PV technologies like amorphous silicon (a-Si), cadmium telluride (CdTe) and copper indium di-selenide (CIS). All these technologies have one feature in common, which is the use of materials with a higher absorption coefficient than crystalline silicon and as a result thinner layers are needed. This reduces the amount of material used and consequently a reduction in the price of solar modules is expected. Among the thin film technologies referred to, the one that shows the highest conversion efficiency value of light to electricity is the CIS [14]. CIS has a laboratory champion cell with an efficiency of 20.3 % [15], the other thin films are CdTe with an efficiency of 16.7 % and amorphous silicon 10.1 %, whereas in solar modules CIS has an efficiency of 13.8%, CdTe has 10.9% and amorphous silicon has 8.2 % [14]. Despite the apparent technological lead, economical, historical and industrial reasons created a PV market where CIS is not the dominant technology in thin films. In fact that place belongs to amorphous silicon. But in recent years, this appears to be changing. *First*

Solar[1] alone will have a production line of over 1 GW/year in 2010 making it the largest PV producer in the world. Also, recently, several CIS companies appeared with rather small pilot plants, a few MW/year [9], and since 2009 *Centrotherm*[2] sells a turn-key CIS factory of 50 MW/year. Although CIS appears to be behind when compared with the other two technologies, it is gaining momentum in industry and in the markets.

The reason why *First Solar* has been economically successful and has such high manufacturing capabilities is the price of its modules. Although the modules have a lower efficiency than traditional crystalline modules, they are much cheaper. *First Solar* has announced in 2010 that its fabrication costs are around 0.80 US$/W and other thin film solar cell companies are announcing that they will reach such values in the coming years [16]. For the author, the more important players in the market are the Japanese *Sharp* company using a-Si and micro-amorphous Si; the Swedish CIGS based *Solibro* owned by the German and previous leading PV manufacturer *Q-Cells*, if they are able to recover from the financial restructuration of 2009-2010 which made them have highly negative turnovers; the North-American *NanoSolar*, a roll to roll CIGS company if they finally start selling what they promised and last but not least the Japanese and Dutch Oil company *Showa Shell* which is seriously investing in CIGS. The lack of investment in CIGS is what is deemed to be its main drawback in arriving at the markets [16]. Smaller companies like *Avancis, SulfurCell, Würth Solar, Global Solar, EPV,* among many others, either are not large enough for the high investments alone or lack the aggressive American style of getting highly funded and the politically needed connections. Despite this, the efficiencies of CIGS laboratory solar cells and modules continue to rise and can hopefully draw more attention from the investors.

Finally, it is worth mentioning that one of the CIGS and other thin film technologies' major advantage over crystalline Si that is the capability of controlling the production chain from cell to module through the monolithic integration of the cells. That procedure is done by including patterning steps along the production line [17]. This procedure reduces the number of operations and intermediaries that exist in the traditional Si industry.

---

[1] First Solar, Inc. (Nasdaq: FSLR): CdTe PV company.

[2] Centrotherm photovoltaics AG , Photovoltaics Equipment.

1.4 CIS solar cells

The absorber layer for thin film CIS based solar cells can actually be a family of compounds derived from CIS. CIS has the structure of the chalcopyrite and several variations of this material can be used, $CuInSe_2$, $CuInS_2$, $Cu(In,Ga)Se_2$ or even $Cu(In,Ga)(S,Se)_2$[3]. All share a high absorption coefficient and so only a few micrometers of material are needed in order to absorb most of the incident light. That fact, together with cheaper growth techniques and easy transfer to an industrial application, makes the CIS compound family a promising candidate for cheaper PV.

The first device based in this family of compounds was made in 1974 by Wagner et al. [18]. The cell was prepared from a p-type $CuInSe_2$ single crystal with an evaporated n-type CdS thin film. It took 36 years, but in 2010 laboratory solar cells with efficiencies greater than 20% [19] were reported for the first time.

CIS solar cells are semiconductor p-n hetero-junction devices. When illuminated, electrons and holes are created and some are separated by the electrical field existing in the depletion region of the junction. These carriers are then collected at electrodes and so when illuminated electrical power can be extracted from the device.

In Figure 1-1, a typical CIS solar cell in the substrate configuration is represented. These cells are usually grown on soda lime glass (SLG) and the back electrode is usually a layer or a bilayer of molybdenum with thickness between 0.5 μm and 1 μm. The absorber layer comes next with a thickness ranging from 1 μm up to 3 μm. To complete the junction an n-type material is required and CdS with a thickness of around 50 nm is used, this layer is called the buffer layer. Atop the buffer layer a window layer is deposited, for this a transparent conductive oxide layer such as aluminium doped - zinc oxide (ZnO:Al), gallium doped zinc oxide (ZnO:Ga) or tin doped indium oxide (ITO) are used. At the top there can be a metallic grid for better charge collection, for this, usually a grid of nickel and aluminium is used, afterwards an anti-reflection layer, generally made of magnesium fluoride, can also be used.

---

[3] In this thesis the chosen nomenclature for $CuInSe_2$ with and without Ga is CIGS and CIS.

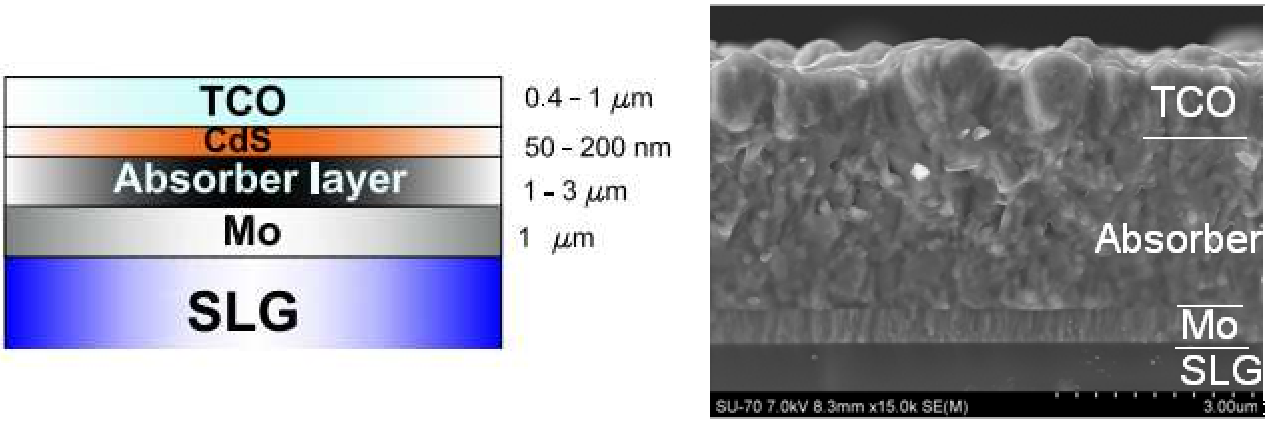

Figure 1-1: a) Layer sequence of a thin film solar cell device with the following sequence: SLG/Mo/absorber layer/CdS/TCO. The figure is not to the scale. b) SEM micrograph of a thin film solar cell cross section, the CdS layer is not visible.

This typical solar cell structure was first described in 1985 by Potter et al. [20]. Since then some modifications have been made to improve the efficiency but the structure of the cell is the same and the changes were focused rather on the understanding of the physics of the materials and of the cells.

1.5 The availability of indium

One of the problems that the CIS industry will be facing in the future will be the high prices of indium. Indium is mined as a by-product of Zn [21] and it is quite scarce on the earth's crust, 0.049 ppm [22, 23]. For comparison, one can see in Figure 1-2 the abundance in the earth's crust and prices for different elements. Because In is so scarce, the demand can be larger than the supply and this leads to high variations in the price.

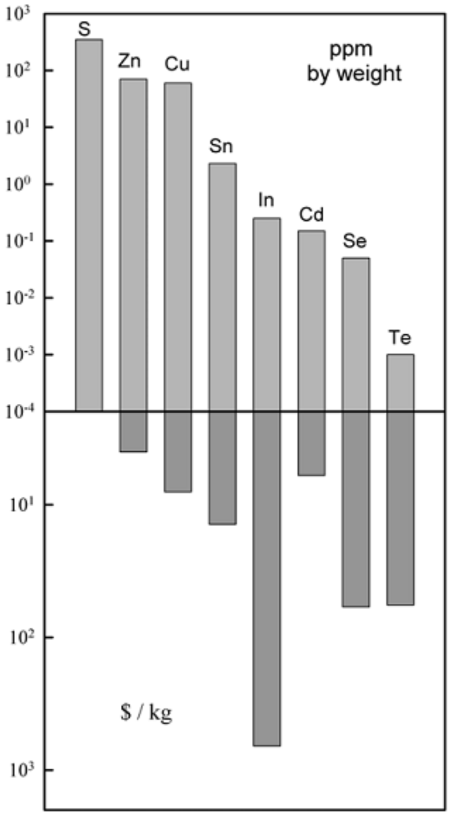

Figure 1-2: Abundance of elements (upper part of the figure) and 2007 prices of raw elemental materials (lower part of the figure) for thin film PV. Adapted from [23].

Green has estimated that in order to keep the contribution of In below 0.20 US$/W in the cost of a solar module, indium prices would have to be lower than 1600 US$/kg [21]. As B. Schubert et al. point out, by dividing the known indium reserves by its current annual consumption, indium will be exhausted within the next 14 years [24]. However, if the same calculation had been done 10 years ago, predictions would indicate that indium would have been completely exhausted by now. Both these statements make us realize that estimating the future prices and availability of a resource and its influence on an industry is a hard task. If one considers the scarcity of indium and assumes that in the near future, CIS will have production plants with capacities of GW/year, it is quite clear that indium will be a limiting factor for reduction of the cost per Watt of a solar module. Some short term solutions for the problem rely on raising the efficiencies of the solar modules or use thinner layers of the absorber material. These actions are already being taken in the industry but will not solve the problem.

Another alternative solution for the indium problem is to replace the absorber layer with a material that does not use scarce elements. $Cu_2ZnSnSe_4$ (CZTSe) or Cu_2ZnSnS_4 (CZTS) are possible options. These materials started to be studied in the late 1980s and 1990s [25-28] but it was in the last decade that they gained more attention. They are both p-type materials and only need a few microns of material in order to absorb almost all the incident light. Moreover their crystalline structure is similar to the CIS one.

1.6 Scope of this thesis

This thesis focuses on two subjects: the optimization of CIGS's growth by the hybrid method which is the follow up of previous work, and the study of $Cu_2ZnSnSe_4$ and $Cu_2ZnSn(S,Se)_4$ as possible alternatives as absorber layers for solar cells.

Different approaches for Ga incorporation in CIGS have been studied in this work. Three different setups were analysed: sputtering of Ga using a liquid target, direct evaporation of Ga and the use of a CuGa target.

Regarding CZTSe, different approaches have been addressed during this work as well. At the beginning of these studies, almost no thermodynamic growth data was available for the latter material, therefore a large part of the studies conducted focused on finding the right conditions to grow single phase CZTSe. After the right conditions to grow CZTSe were found, more detailed studies of the properties of this material were possible and solar cells were prepared. In the last part of the thesis, preliminary work on the growth of $Cu_2ZnSn(S,Se)_4$ was carried out and some results are shown.

A significant part of the work leading to this thesis aimed at improving the solar cell base-line production of the research group and therefore some work on the other layers was also done. The most important and detailed one was the study of the molybdenum bilayer.

The thesis is divided in 6 chapters. Chapter 1 is the introduction followed by chapter 2 where a review of the state of the art and the properties of CIGS and CZTSe is done. In chapter 3 the experimental techniques used in this work are described and in chapter 4 the growth and properties of the absorber layers are presented. The solar cell results, as well as the optimization studies for the other solar cell layers can be found in chapter 5. Finally, in chapter 6, the conclusions of the thesis are drawn and suggestions for further work are presented.

2 Solar cells and new absorber materials

This chapter is divided into three different sections. The first one is the electrical considerations of p-n junctions and its relation with solar cells. Then follows a section devoted to each material studied in this work. The most important properties of CIGS are presented in section 2.2. There, the objective was not to have a fully detailed description of the material but rather a small introduction since the studies of CIGS are a follow up of previous works. CZTSe is explored in section 2.3 and CZTSSe is the main topic of section 2.4.

Before addressing each of the subsections, let us consider the several requirements for the absorber material used in thin film solar cells. These will allow a better understanding of some of the concepts explained ahead in the text.

In order to obtain the maximum efficiency, the material used as absorber needs to have a band gap energy close to 1.4 eV as stipulated by the Shockley-Queisser limit [29]. This already limits the efficiency of a p-n junction based solar cell to 33%. Basically this constraint comes from the fact that photons with energy lower then the band gap are not absorbed and the ones with higher energy generate hot carriers, losing their energy to increase the absorber temperature.

Electrically, the material should be capable of delivering charge carriers. For that, high diffusion lengths both for electrons and holes are required, but since the films used are polycrystalline, the life time and diffusion length of the carriers are not as high as in mono-crystalline films, this requires the films to be as thin as possible. Having that in mind, the material has to absorb as much incident light as possible, thus having a high absorption coefficient, α, is crucial. For α close to 10^5 cm^{-1}, 2 μm thick films can absorb most of the incident light.

The material must also form an ohmic contact with the metal used as electrical back contact, and have a suitable band alignment with the n-type material. This will be addressed within each material section.

2.1 Basics of p-n junctions

Solar cells are devices based on p-n junctions. Let one consider a p-n$^+$ junction or a diode. The current that flows through a biased p-n$^+$ junction can be calculated using Shockley's model:

$$j_{diode}(V) = j_0\left(\exp\left[\frac{qV}{AkT}\right]-1\right) \tag{eq 2-1}$$

where *j* is the current density, *k* the Boltzmann's constant, *T* the temperature, *V* the applied voltage, j_0 is a current factor called the saturation current density, *q* the electron charge and *A* is the ideality factor for a diode. In a more realistic model than Shockley's, the losses are accounted for by including a series, R_s, and a parallel, R_p, or shunt, resistance as presented in Figure 2-1. Then the current can be described by:

$$j_{diode}(V) = j_0\left(\exp\left[\frac{qV-qjR_s}{AkT}\right]-1\right)+\frac{V-jR_s}{R_p} \tag{eq 2-2}$$

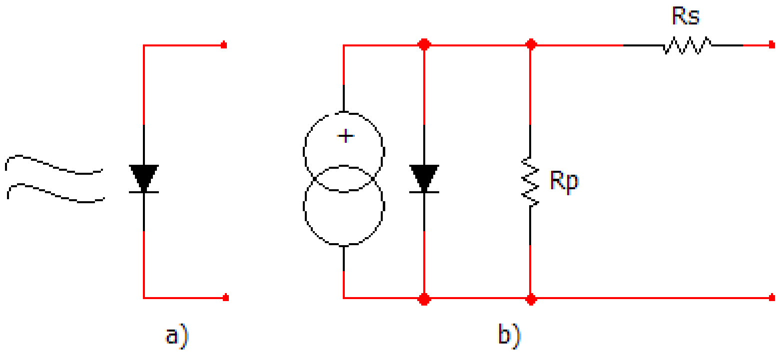

Figure 2-1: a) Solar cell usual schematic symbol, b) solar cell equivalent circuit.

The exact form of j_0 depends on the transport mechanism of the junction. Usually the transport is set by a group of mechanisms rather than by only one. One of the dominant mechanisms that are usually accepted is the diffusion mechanism, there j_0 is described by:

$$j_0 = j_{diif} = \frac{qN_C N_V D_n}{N_A L_D} \exp\left(\frac{qV - E_{gap}}{kT}\right) \tag{eq 2-3}$$

where N_C and N_V are the effective densities of states of the conduction and valence band respectively, N_A is the acceptors' density, L_D the diffusion length of electrons and D_n the diffusion constant for electrons in the p-type material.

Under illumination, the electrical properties of the junction are modified because electron-holes pairs are generated and separated by the electric field existing in the depletion region, thus creating a photogenerated current. Electron-hole pairs are also generated outside the depletion region but only the ones at the distance of the diffusion length contribute significantly to the photogenerated current because the others are lost through recombination. The creation of the photogenerated current happens mostly in the absorber layer due to most of the depletion width being located in this layer. Since in thermal equilibrium the electric field far from the junction at either side must be zero, the total negative charge per unit in the p-side must be equal to the total positive charge per unit area in the n-side [30]:

$$N_a W_{dp} = N_d W_{dn} \tag{eq 2-4}$$

where N_a is the concentration of acceptors in the p-type semiconductor, W_{dp} the depletion width in the p-type semiconductor, N_d the concentration of donors in the n-type semiconductor and W_{dn} the depletion width in the n-type semiconductor. Since the p-type material has a higher absorption coefficient than the n-type material, let us consider a p-n$^+$ junction. In this case, N_d will be much greater than N_a and therefore, W_{dp} will be much larger than W_{dn}. This is why most of the photons that participate in the generation of a photo-current are mostly absorbed in the depletion region of the p-type semiconductor or also called the absorber material. Under illumination, the equation that describes the current of a solar cell is given by:

$$j = j_{diode} - j_{ph} \tag{eq 2-5}$$

where j_{diode} is the current from (eq 2-2) and j_{ph} is the photo-generated current. Note that in the situation where R_s=0, R_p= ∞ and V=0, j_{diode} is zero and then the current that passes trough the cell is the photogenerated current called short circuit current, j_{sc}. If j=0 the open circuit voltage, V_{oc}, takes the value from (eq 2-7):

$$j_{diode} = 0 \Rightarrow j_{ph} = j_{sc} \qquad \text{(eq 2-6)}$$

$$V_{OC} = \frac{AkT}{q} \ln\left(\frac{j_{ph}}{j_0} + 1\right) \qquad \text{(eq 2-7)}$$

Another important parameter to evaluate the performance of a solar cell is its conversion efficiency of light to electrical power. This efficiency, η, is the ratio between the maximum produced electrical power, given by j_m and V_m, and the incident power, P_{inc},:

$$\eta = \frac{j_m V_m}{P_{inc}} = \frac{j_{SC} V_{OC} FF}{P_{inc}} \qquad \text{(eq 2-8)}$$

where *FF* is the fill factor which describes the area of the j-V curve given by the point (j_m, V_m). High values of fill factor means that the cell may provide more power. *FF* is given by:

$$FF = \frac{j_m V_m}{j_{SC} V_{OC}} \qquad \text{(eq 2-9)}$$

2.2 CIGS absorber layers

CIS is a p-type direct band gap semiconductor and is intrinsically doped since the p-type conductivity comes primarily from Cu vacancies [31]. The compound $CuIn_{1-x}Ga_xSe_2$ derives from the chalcopyrite compound $CuInSe_2$ by replacing some of the In by Ga atoms. CIGS has a high absorption coefficient, around 10^{-5} cm^{-1} and a band gap energy that changes with the quantity of Ga present. Since on chemical grounds Ga and In are similar, CIGS has properties close to the ones of CIS. The introduction of Ga into the structure is used because its presence increases the band gap value by changing the minimum of the conduction band. The band gap value of CIS is 1.02 eV and $CuGaSe_2$ has a band gap value of 1.69 eV. The band gap value of $CuIn_{1-x}Ga_xSe_2$ where x is [Ga]/([Ga]+[In]) varies according to the following equation [32]:

$$E_{gap}(x) = 1.02 + 0.67x + 0.11x(x-1)[eV] \qquad \text{(eq 2-10)}$$

Thus band gap engineering is achieved by changing the in-depth Ga concentration. Through this band gap engineering it is possible to enhance the solar cell's performance.

Usually when growing CIGS, Ga has the tendency to accumulate in the back of the film [33-34]. This, in fact, leads to cells with better efficiencies [35] and the normal explanation for this is due to the formation of a quasi-electric field which leads to reduced recombination at the back contact.

The quasi electric field, ξ_A, is the effect created by a Ga profile as seen in Figure 2-3. This variation in the concentration of Ga creates a gradient of the electronic affinity since the conduction band is changing and thereby electrons are directed towards the junction [32]. Since Ga content also increases the band gap, it has been found that the maximum solar cell efficiency is obtained when the Ga concentration is increased at the front as well, creating this way a double graded profile as shown in Figure 2-2. This double grading is only considered beneficial if the top grading does not create a bang gap value higher than at the back and if it is inside the depletion width [33]. There is also the possibility of increasing the band gap at the surface of the film, by replacing Se by S which also increases the band gap. $CuInS_2$ is also an interesting material for solar cell applications, due to its higher band gap energy, but was not studied in this thesis so it is not reviewed here, for more information on this compound the reader can see for instance R. Klenk et al. [36].

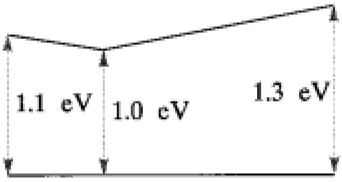

Figure 2-2: Double graded profile on band gap of a CIGS film. The left part is the top of the film and the right part is the back. Adapted from [37].

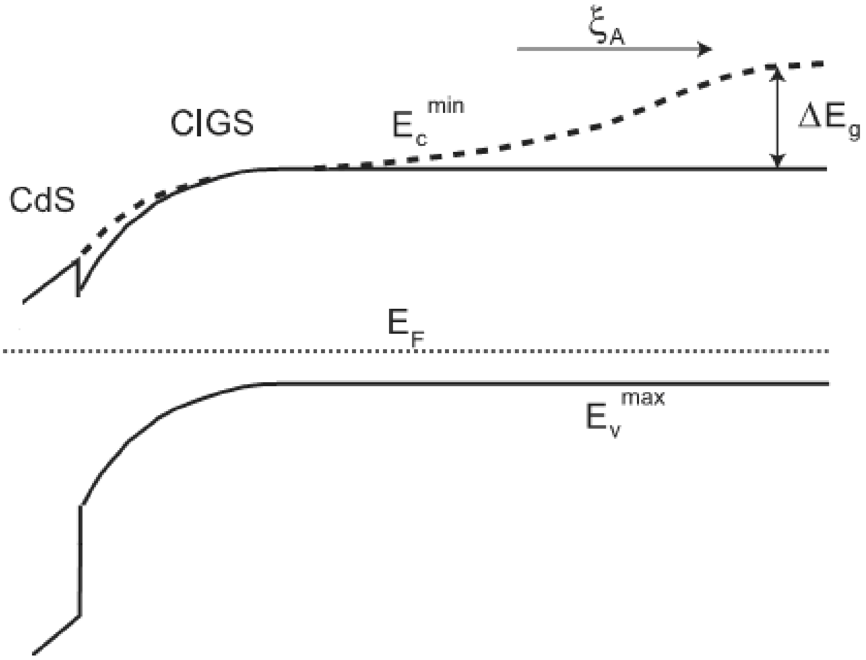

Figure 2-3: Band diagrams of a CIGS thin film solar cell. The dotted line illustrates the effect of increasing the Ga content at the valence band. An additional "electric field" is obtained due to the band gap variation. Adapted from [32].

One of the most important and interesting properties of CIGS is its distinct shift of properties when passing from a Cu-poor phase to a Cu-rich phase. Cu-rich CIGS is formed with large grains and therefore good crystalline properties but its electrical properties are poor to be used in solar cells, mainly because it may grow with n-type conductivity. Cu-poor CIGS films have usually smaller grains and therefore worse crystalline properties but electrically are much more suitable than Cu-rich CIGS [38]. In order to try to use both properties, a bilayer process was first tried by Mickelsen et al. [39]. This process is usually called the Boeing process, and basically consists in growing CIGS using co-evaporation in two steps. The first step is Cu-rich and thereby produces films with large grains, followed by a Cu-poor step where the film reaches the desired stoichiometric point with larger grains and good electrical properties.

Nowadays, the best CIGS thin film solar cells are obtained when the absorber is grown by co-evaporation using a 3-step method. Instead of using the bilayer process, the film is initially grown in a Cu-poor state, then Cu-rich and finally finishes in a Cu-poor state [35, 40-42]. What makes this transition even more interesting is that due to a change in the film's emissivity, the thermal energy, needed to sustain a certain substrate temperature, changes from one state to another [43, 44]. This makes the *in situ* identification of the Cu-poor/Cu-rich transition possible during the growth of the film simply by looking at the substrate temperature or heater power needed during the different steps. This *in situ* technique to evaluate the Cu-state of the films was firstly used by Kohara et al. [45]. Afterwards several research groups started to call it End Point Detection, or EPD [46, 47]. The change of the film's emissivity is associated with abrupt change in the hole concentration caused by the Cu vacancies [43].

The author with this section does not intend to make an exhaustive review of the CIGS's properties but rather an introduction to this type of materials. This is so, mainly because the studies done on CIGS in this thesis were just a small part of the whole work which was focused on CZTSe. Nevertheless, if the reader would like to acquire a more in depth knowledge of CIGS, there are some papers about the properties of CIGS that the author recommends. Theoretically the electronic structure of CIS compounds has been studied by Zunger's group [31, 48]. Regarding the growth of CIGS, there are at least three good reviews that cover most of the techniques used to grow CIGS, Kemmel et al. [49] and Niki et al. [50]. Non-vacuum methods are explored by Hibberd et al. [51]. CIGS structural properties have been the topic of several review papers [52-55]. The electrical properties with a special focus on the grain boundaries have been reviewed by Siebentritt et al. and Hafemeister et al. [56, 57]. The influence of Na was the topic of study of Rudmann's PhD thesis [58]. The Ga profile was studied numerous times by several research groups, see for instance [32] and a detail study on the change of emissivity of the films is done in [59].

Since the Ga profile plays a very important role in the solar cells' performance and is considered a challenge to be used at an industrial scale, in this thesis different incorporations of Ga are tested in the hybrid method. The first one was an attempt of sputtering films of Ga using a target of Ga. The next one was to evaporate Ga and finally the use of a CuGa target to introduce Ga in the films by sputtering.

2.3 CZTSe absorber layers

The idea of using CZTSe as a replacement for CIGS, is the result of an argument for the need to replace In by cheaper elements. Zn and Sn were introduced to replace In and form CZTS for the first time by Ito [25]. CZTSe solar cells were first presented by

Friedlmeier in her Ph.D. thesis [28]. CZTSe appeared as a good replacement, because there were some reports that showed the material to be p-type and had a high absorption coefficient.

The CZTSe structure is somewhat similar to the CIGS structure. CIGS crystallizes in the chalcopyrite structure which belongs to the tetragonal system. Basically it is a tetragon made of two sphalerite structures on top of each other. This makes *a=b* and *c~2a*. The stannite structure is obtained by lowering the symmetry of chalcopyrite and replacing the element of group III by two of groups II and IV. This decrease of symmetry is obtained by the substitution of the metals, but also by changing the metal ordering, i.e. the arrangement of the cations on the structural sites of the unit cell. The kesterite structure is obtained by further changing the order of the cations. These modifications can be seen in Figure 2-4.

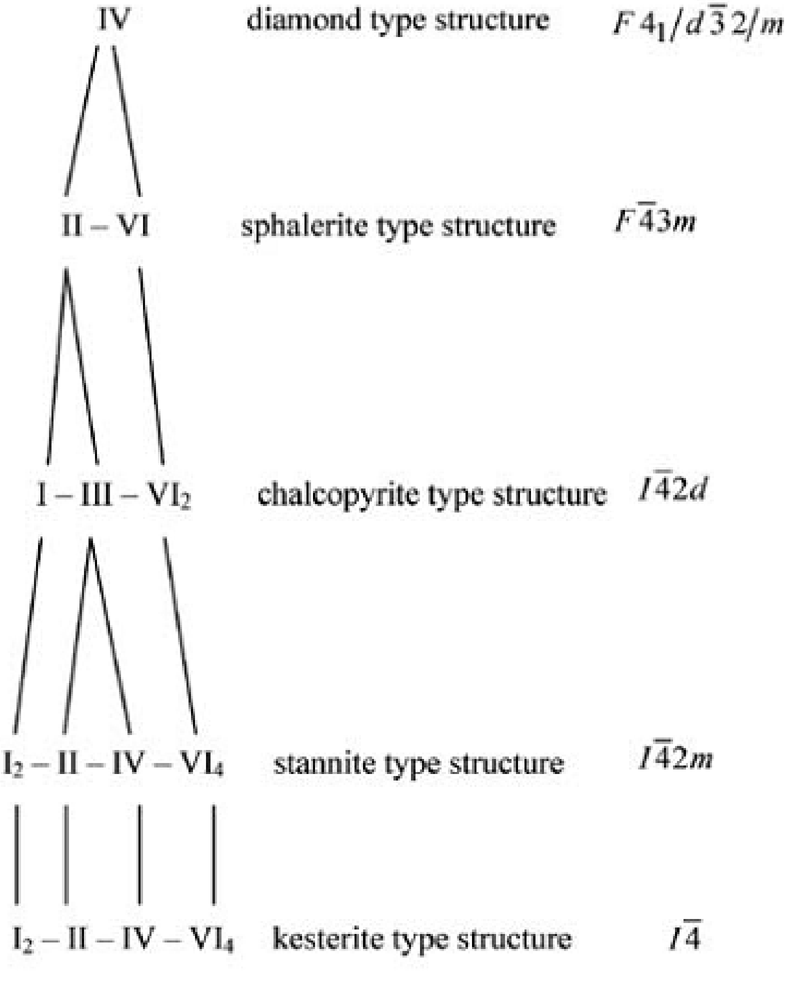

Figure 2-4: Evolution of the adamantine family. Adapted from [60].

The names of these structures come from the mineral names, kesterite is Cu_2ZnSnS_4 and stannite is Cu_2FeSnS_4. The mineral kesterite was first mentioned in the literature in 1958 by Orlova [61]. As stated before, both structures are derived from the chalcopyrite structure, mineral $CuFeS_2$. The family of all these compounds is called adamantine. These materials were studied by Pamplin [62] where he first described that these materials should obey the octet rule, i.e., there should always be eight electrons around each chalcogen atom.

The difference between stannite and kesterite is seen in Figure 2-5 and in Table 2-1. The CIS chalcopyrite structure is represented in Figure 2-5 as well. The difference of the two structures relies on a switch of positions between Cu and Zn, being the kesterite structure more disordered. The ions Cu^+ and Zn^{2+} have the same number of electrons and these elements are neighbours in the periodic table. Their atomic scattering factor, which is proportional to the measured intensity in an X-ray diffraction experiment, is identical. Hence these ions are not distinguishable by conventional X-ray diffraction (XRD). Schorr [60] has suggested using neutron diffraction as a possible technique to distinguish between stannite and kesterite.

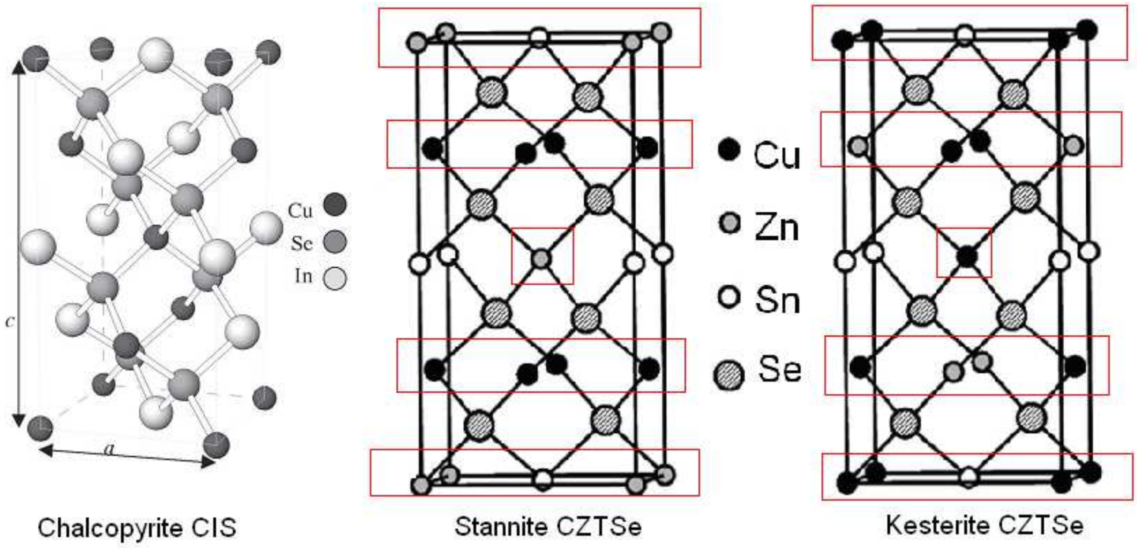

Figure 2-5: Crystal structure of chalcopyrite, kesterite and stannite. Highlighted in red, the differences in the Zn and Cu atoms are shown. Adapted from [54, 63].

Table 2-1: Position of atoms for the stannite and kesterite structures.

Position	I-42m Stannite Wyckoff / atom	I-4 kesterite Wyckoff / atom
(0,0,0)	2a Zn^{2+}	2a Cu^{1+}
(½,½,0)	2b Sn^{4+}	2b Sn^{4+}
(0, ½, ¼)	4d Cu^{1+}	2d Cu^{1+}
(0, ½ , 3/4)	-	2c Zn^{2+}
(x,x,z)	8i Se^{2-}	-
(x,y,z)	-	8g Se^{2-}

Despite this identification problem, several studies assign CZTSe to the stannite structure as is shown in the historical overview of Table 2-2. This historical overview shows that regardless of the identification problem, several research groups stated that the structure is stannite. This probably happened in a cascade process where the first author stated to have the stannite structure. After that and since the position of the peaks for stannite and for kesterite are exactly the same, other research groups followed the same interpretation. To complicate even further the problem, in the International Centre for Diffraction Data, there is only a datasheet for stannite CZTSe. Later in this thesis, this identification problem will be addressed.

Table 2-2: CZTSe structural identification reported.

Year	Reference	a	c	c/2a	Structure
1965	64	5.681	11.34	0.998	stannite
1974	65	5.681	11.34	0.998	stannite
1979	62	5.69	-	-	sphalerite
1980	66	5.681	10.843	0.954	stannite
1997	28	-	-	-	kesterite
2000	67	5.693	11.333	0.995	stannite
2002	68	5.689	11.337	0.996	stannite
2005	69	5.597	11.21639	1.002	stannite
2005	70	5.693	11.33	0.995	?
2006	71	-	-	-	stannite
2007	72	5.776	11.677	1.011	stannite
2008	73	5.68	11.36	1.000	kesterite
2008	74	5.69	11.41	1.003	kesterite
2009	75	5.684	11.353	0.999	stannite

The growth of CZTSe thin films has been firstly reported by Pamplin et al. [62]. Guen et al. [66] reported the growth of CZTSe by iodine transport with the objective to study electrical and magnetic properties. After this early work, only Friedlmeier [28] in 1997 presented results on the growth of CZTSe solar cells grown by co-evaporation with an efficiency of 0.6%. Although it was never calculated directly, Friedlmeier estimated the band gap energy to be around 1 eV. Matsushita [67] grew CZTSe crystals and obtained samples with a p-type conductivity, a band gap energy of 1.44 eV and a melting point around 805 ºC. Olekseyuk [68] studied single crystals and reported Ritveld analysis proving that the crystallization of CZTSe was done in the stannite structure. The first and only thermodynamic study of the CZTSe phase equilibria was done by Dudchak in 2003 [76]. Using ab-initio calculations Raulot [69] estimated the band gap energy of CZTSe around 0.9 eV. Matsushita [70] estimated the band gap energy of CZTSe single crystals to be 1.5 eV. In 2006 Altosaar [71] reported preparation of CZTSe monograins solar cells. In the latter they show different studies and properties: a photoluminescence emission at 0.81 eV; a XRD diffractogram in which the stannite structure was presented; express doubts over the band gap energy which is as high as 1.5 eV and present solar cells with an efficiency of 1.8%. Wibowo et al. [72] presented the growth of CZTSe thin films by RF magnetron sputtering from binary chalcogenide targets at a substrate temperature of 175 ºC, then they show a XRD diffractogram with 5 reflections. In that work a band gap energy of 1.56 eV was also reported. In 2007 Wibowo et al. [77] have also grown CZTSe thin films by selenization of sputtered binary compounds, it was basically an annealing of the samples grown in the previous report. Still in 2007, Wibowo et al. [78] reported the growth of CZTSe thin films by pulsed laser deposition of a quaternary target. In that work, the best films were grown at a substrate temperature of 500 ºC and the following properties were calculated: band gap energy of 1.5 eV, a free carrier density of 2.2 x 10^{17} cm^{-3} and a Hall mobility of 1.5 $cm^2V^{-1}s^{-1}$. In 2007 Herbert et al. [79] predicted that there are two paths for the formation of CZTSe:

Path 1 $Cu_2Se/CuSe + ZnSe + SnSe/SnSe_2$ (+/-Se) → CZTSe

Path2: a) $Cu_2Se/CuSe + SnSe/SnSe_2 \rightarrow Cu_2SnSe_3$

Path2: b) $Cu_2SnSe_3 + ZnSe \rightarrow$ CZTSe

Later in this thesis, it will be shown that it is likely that in some cases, both paths happen at the same time. Babu et al. [73] grew CZTSe thin films by co-evaporation and estimated that the best growth temperature under those conditions was 350 ºC without an annealing step, and 450 ºC with an annealing step. They obtained XRD peaks as broad as 0.3º and by looking at the (1 1 2) peak they were able to identify CZTSe and ZnSe. A band gap energy of 1.48 eV and an optical absorption coefficient higher than 10^5 cm^{-1} were reported. The same results were presented by Babu et al. in another paper [74]. In 2008 Altosaar [80] revealed for the first time Raman scattering studies of CZTSe. They identified the peaks at 173 cm^{-1}, 196 cm^{-1} and 231 cm^{-1} as CZTSe Raman scattering peaks. In the same work, the authors saw a PL emission at 0.85 eV and presented solar cells based in mono-grains with an efficiency of 2.16 %.

With the record efficiency of a CZTS solar cell of 6.7 % reported by Katagiri et al. in 2008 [81], the whole family of materials, CZTS and CZTSe, started to attract more attention from the research community. In 2009 the number of papers with the main topic being CZTSe suddenly increased.

The photoluminescence emission from CZTSe monograins was studied by Grossberg et al. [82] in 2009 and a broad emission at 0.946 eV was found for the CZTSe. With these experiments, they estimated the band gap energy of CZTSe to be around 1.02 eV. Volobujeva et al. [83, 84] presented in 2009 CZTSe thin films grown by selenization of metallic evaporated precursors. In the same work the authors showed Raman and XRD studies and only obtained good quality CZTSe films at temperatures higher than 370 ºC but were not able to grow single phase films. Wahab et al. [85] studied CZTSe films grown by the melt quenching technique. They showed very poor quality films with a band gap energy of 1.7 eV. In 2009 Zoppi et al. [75] reported an efficiency of 3.2 % for a CZTSe solar cell grown by selenization of metallic precursors deposited by magnetron sputtering. They estimated the band gap energy to be 0.94 eV using the external quantum efficiency. Until the date of writing of this thesis, this is still the best reported efficiency for solar cells using CZTSe thin films. The electronic structure of CZTSe was studied using first principles calculations by Nakamura et al. [86], they reported a band gap energy of 1.7×10^{-5} eV. Liu et al. [51] grew slightly Cu-rich CZTSe crystals to study its thermoelectric properties. Shi et al. [87] analysed CZTSe ingots and reported the following parameters: electrical conductivity of 4500 Sm^{-1}; a Seebeck coefficient of 130 μVK^{-1}, a thermal conductivity of 3.2 $Wm^{-1}K^{-1}$ and a hole concentration of 1 x $10^{19}cm^{-3}$. An additional possible structure has been suggested to appear in CZTSe by Chen [88]. They have suggested that not only kesterite (KS), I-4, and stannite (ST), I-42m, could appear but a primitive mixed CuAu-like (PCMA), P-42m was also possible. They have estimated, by first principles calculations, that KS is the most stable structure because of its lowest formation energy value, however the difference to ST is only 3 meV. To complicate even more, the same research group suggested another structure, a partially disordered KS (PD-KS). They estimated the band gap energy to be 0.96 eV and despite all these phases, the ordering of the Cu and Zn atoms should not influence strongly the electrical properties since the band structure barely changes. Using density functional theory, Sevik et al. [89] stated that the density of states and band structures of the different possible structures, KS, ST and PCMA, is so similar that no changes in the structure, mechanical and electronic properties should be seen. Chen et al. presented two different papers [90, 91] where the results for the properties of CZTSe and other materials were calculated by density-functional theory. Their main conclusions were: kesterite has a value of *c/2a* lower than 1 and it is the most likely structure, the reported stannite structure in the literature is probably a partially disordered KS, the band gap energy was estimated to be 1.0 eV for the kesterite and there should not be a difference larger than +0.2 eV in the band gap energy for the stannite structure.

In 2010 a high number of publications with CZTSe as the main topic continued to appear. CZTSe nanocrystals were chemically deposited by Shavel et al. [92]. Krustok et al. [93] found a value for the band gap energy of 1.0 eV by analysing the quantum efficiency curves on CZTSe monograin solar cells and estimated that the material had spatial potential fluctuations with an average depth of 25 meV. Todorov et al. [94] announced a new record for kesterite based solar cells grown using a non vacuum ink process. He presented a solar cell with a conversion efficiency of 9.66% with an absorber layer consisting of $Cu_2ZnSn(S,Se)_4$ (CZTSSe). It is expectable that this value, which is close to 10%, will bring even more research groups into the area. Krustok et al. [95] continued the analysis of monograin CZTSe solar cells and reported a degradation of the V_{oc} with temperature of -1.97 mV/K. Babu et al. [96] continued to grow CZTSe thin films by co-evaporation and presenting XRD diffractograms showing films with broad peaks. The latter authors estimated a band gap energy ranging between 1.37 eV and 1.62 eV for samples with a ratio [Cu]/([Zn]+[Sn]) of 1.14 to 0.83, respectively. CZTSe nanocrystals formed by hot injection were presented by Hao Wei et al. [97]. The first interesting theoretical in-depth study of CZTSe and CZTS was done by Person et al. [98]. Their main conclusions were: both structures have similar electronic band structure, dielectric functions and optical absorption coefficients; from the possible different structures, kesterite structure is the most likely because of the lower internal energy; the band gap for the kesterite was calculated to be 0.89 eV and for the stannite 1.05 eV; the dielectric constant is between 8.2 and 9.0 and the effective masses of holes and electrons were estimated. Very recently, Ahn et al. [99] using a different method has reported the band gap value of CZTSe to be between 1.02 eV and 1.05 eV which is in accordance with the findings of this thesis. In the same work they used not only XRD but also Raman scattering to confirm the presence of CZTSe.

2.3.1 Phase identification problem with XRD

A problem that is usually overlooked in the publications where CZTSe is addressed is its XRD peak assignment. Resolving CZTSe from unwanted secondary phases is difficult using XRD data. In Table 2-3 the unit cell sizes for CZTSe, cubic ZnSe, cubic Cu_2SnSe_3 and cubic Cu_2Se, are presented and one can see they are almost the same. Other phases, namely CuSe, SnSe and Sn_2Se are also presented, but these can be identified using XRD analysis. The biggest difference is for Cu_2Se which can be resolved using XRD. The difference in the lattice parameter a, is less than 0.004 Å for the cubic Cu_2SnSe_3 and less than 0.02 Å for ZnSe. Given that CZTSe has the stannite or the kesterite structure that comes from the tetragonal family which is basically a double-cubic structure, most of its reflections are in the same position as the above mentioned phases. This is seen in Table 2-4 where the most intense peaks for these phases are presented. There is also a row where the angular differences between the position of the unwanted phases and the position of CZTSe are shown. For ZnSe, the largest difference is 0.15º. For CZTSe the peak is situated at 72.48 º with an intensity of 76, whereas the ZnSe peak is situated at 72.63º with intensity 331. Note that these intensities are normalized to 1000, which means that these peaks are quite weak. Usual system resolutions for XRD systems are close to these angular differences. With broad peaks, this distinction is even harder to detect. For the cubic

Cu_2SnSe_3, the biggest difference is 0.16º. The two presented copper-selenide phases are easier to identify since the differences to CZTSe are bigger than the previous compounds. For the cubic and for the hexagonal phase the peak positions are quite dissimilar as they have different structures. Despite the fact that all the cubic ZnSe and cubic Cu_2SnSe_3 diffractions peaks are extremely close and/or superimposed with those of CZTSe, the latter possesses additional peaks that are not common with these unwanted phases. Such examples are the peaks at 15.61º and 17.42º and the double peaks at 53º, 65º and 72º. Usually, the intensity of the single peaks and the double peaks at 65º and 72º is low and therefore the double peaks at 53.39º and 53.53º can be used to evaluate the presence or absence of CZTSe. Using these peaks, one can then say whether CZTSe is present or not. However, nothing can be said regarding the other phases. Most of the works reported before, only use XRD to evaluate the presence of secondary phases and so, the author believes that some of the presented properties, supposedly belonging to CZTSe, may be, in reality, the effect of unwanted phases. Such example is the band gap energy, for which until 2010 there were reports for values ranging from 1.0 eV to 1.5 eV. As reference, the band gap energies for CZTSe and other phases likely to appear during its growth are presented in Table 2-3 .

In order to overcome the identification problem, the author has suggested the use of Raman scattering as a complementary technique to analyse the different phases present [I]. Raman scattering can provide phase identification and in well studied materials can be used to assess nano-scale structural changes. For more information on Raman scattering the review paper of Gouadec is recommended [101].

Table 2-3: Unit cell properties: differences between CZTSe, ZnSe, CTSe, Cu_2Se and CuSe.

Compound	CZTSe	ZnSe	Cu_2SnSe_3	Cu_2Se	CuSe	SnSe	$SnSe_2$
structure	tetragonal	cubic	cubic	cubic	hexagonal	orthorhombic	hexagonal
a (Å)	5.6882	5.669	5.684	5.763	3.984	4.460	3.8108
b Å)	5.6882	5.669	5.684	5.763	3.984	11.570	-
c (Å)	11.3378	5.669	5.684	5.763	17.288	4.190	6.1410
cell volume (Å^3)	366.8	182.17	183.64	191.4	237.64	216.21	77.23
ICDD ref [100]	04-010-6295	04-007-4741	03-065-4145	01-071-4843	00-027-0185	04-004-4281	01-089-3197
Band gap energy (eV)	1.05	2.6	0.74-0.84	1.4 indirect 2.2 direct	1.4 indirect 2.2 direct	1.26	0.92
Reference	This thesis [99]	[102]	[80, 103,104]	[105, 106]	[105]	[107]	[108]

Table 2-4: XRD peak positions for different selenide compounds [100].

CZTSe angle (º)	Intensity (arb. units)	Planes	ZnSe angle (º)	Intensity (arb. units)	Planes	Difference to CZTSe (º)	Cu_2SnSe_3 angle (º)	Intensity (arb. units)	Planes	Difference to CZTSe (º)	Cu_2Se angle (º)	Intensity (arb. units)	Planes	Difference to CZTSe (º)
27.16	999	112	27.22	999	111	-0.06	27.15	999	111	0.01	26.88	473	111	0.28
45.12	493	204	45.2	585	220	-0.08	45.07	597	220	0.05	44.61	999	220	0.51
53.39	230	312	-	-	-	-	-	-	-	-	-	-	-	-
53.53	233	116	53.57	315	311	-0.04	53.41	321	311	0.12	52.86	152	311	0.67
65.59	52	400	-	-		-	-	-	-	-	-	-	-	-
65.84	34	8	65.84	70	400	0	65.64	71	440	0.2	64.92	117	400	0.92
72.36	42	332	-	-	-	-	-	-	-	-	-	-	-	-
72.48	76	316	72.63	94	331	-0.15	72.41	96	331	0.07	-	-	-	-
83.19	87	424	-	-	-	-	-	-	-	-	-	-	-	-
83.35	57	406	83.46	110	422	-0.11	83.19	113	422	0.16	82.2	180	422	1.15

2.3.2 Phase diagrams, band diagrams and electrical properties

For the CZTSe system there is a work done by Dudchak et al. [76] that covers most of the binary and ternary combinations of Cu-Sn-Zn-Se phases. Among many results, the most significant one showed that there was low solubility of CZTSe with binaries and the composition intervals where it is formed are narrow. This shows that the formation of non-stoichiometric CZTSe is hard, if not almost impossible.

Regarding the electrical properties, for CZTSe there is not yet a detailed study, but there is a theoretical one made by Chen et al. [109] for CZTS. CZTS and CZTSe should have some similarities in the electronic structure and therefore it is relevant to take a look at those studies. Chen et al. reported that the dominant p-type defect is Cu_{Zn} with an acceptor level higher than the one for the chalcopyrites, which suggests that p-type doping in CZTS is more difficult than other chalcogenide compounds such as $CuInSe_2$. They propose the growth of CZTS in Cu-poor/Zn-rich conditions, and thus V_{Cu} and Zn_{Cu} should become the dominant defects in the system since its formation energies are lower, however this condition may lead to the formation of unwanted phases like ZnS. Similar studies for CZTSe are needed to understand if the underlying physics is the same or not. It is necessary to correlate that future information with the one provided by Dudchak et al. [76] to evaluate if the intrinsic doping of single phased CZTSe is possible and under what conditions.

There are still a considerable number of problems dealing with the growth of the CZTSe absorber and thereby the optimization or even the study itself of the solar cell structure is something that has not yet been done. Thus, the best solar cells made with an absorber layer of CZTSe, CZTS or even CZT(S,Se) are still made with the structure: SLG/Mo/CZTS/CdS/i-ZnO/ZnO:Al, which has been optimized for CIGS.

The problem of finding the right conditions for the growth of the absorber bring severe problems to the optimization of cells since the absorber layer’s properties are unknown and hence there is less freedom to explore different approaches to the cell structure. In order to start grasping the band diagram of the actual structure, some of the chalcogenides properties need to be known: band gap energy, electron affinity, the Fermi energy level, carrier concentrations, effective masses for electrons and holes, density of states and the work function. Some experimental measurements like X-ray photoelectron spectroscopy (XPS) or C-V measurements of the cells may provide some insight on the band alignments.

Without the experimental values, some theoretical calculations could be made in order to estimate the band alignments, Avellaneda et al. [110] and Nukala et al. [111] have both done attempts to draw them for the case of CZTS. In our research group, Malaquias [112] predicted that the band gap alignment of CZTS/CdS should be close to the one formed by CIGS/CdS. He was able to do such predictions with regards to CZTS because there are already some published values for the electron affinity and the band gap value is widely accepted to be around 1.5 eV. For the case of CZTSe however, one cannot say the same and therefore better absorbers still need to be obtained to start estimating some of these parameters.

2.4 CZT(S,Se) absorber layers

The idea of using a mixture of CZTS and CZTSe comes from the same usage of replacing selenium for sulphur in CIGS. By replacing Se for S in CIGS, the band gap energy increases and as a result a band gap grading can be achieved. Having this fact in mind and considering that the band gap of CTZS and CZTSe is around 1.5 eV and 1 eV, respectively, it might be possible to make a grading as well in this family of materials. Henceforth, this material will be referred to as CZTSSe.

There are not many reported papers with $Cu_2ZnSn(S,Se)_4$ (CZTSSe) being the main topic of study, mainly due to the fact that CZTS alone has been leading the record cell efficiencies until 2010. The first report of CZTSSe was done by Guo et al. [113]. They have grown CZTSSe nanocrystals and reported a shift to lower diffraction angles of the CZTS (1 1 2) peak towards the CZTSe peak position. Krustok et al. [95] reported solar cells made from CZTSSe “mono grains”, with the composition $Cu_{1.9}Zn_1Sn_1(Se_{0.3}S_{0.7})_{3.9}$, with efficiencies higher than 5%. Todorov et al. [94] reported solar cells with an efficiency of 9.7% with a replacement of 60% of S for Se. This solar cell absorber had a band gap energy of 1.2 eV, which using a simple direct calculation of band gap estimations, 40% x 1.5 eV + 60% x 1eV gives 1.2 eV, which is a further evidence for the 1.0 eV band gap value of CZTSe. But exactly how the bands change from one material to another is important to know because of band alignments. In Todorov's work [94], the absorbers were obtained by sulphurization of an "ink" prepared using hydrazine based solutions. In that work, a solar cell with 9.3% efficiency with a Se content of 94% and 6% of S was also reported which indicates that CZTSe alone is capable of achieving high efficiencies as well.

Those 3 papers are the only detailed studies of the growth of CZTSSe but if the individual materials, CZTS and CZTSe, are still quite unknown, the amount of knowledge of the material is even lower.

In this thesis, some preliminary work concerning the formation of this alloy was done and it is presented in section 4.3.

3 Experimental techniques

3.1 Growth of CIGS

The growth of CIGS was done using the hybrid method. This method combines sputtering and evaporation. The main objective was to test different approaches to incorporation of Ga into CIS. Three different setups were tested, in the first Ga was evaporated and in the second the incorporation of Ga was done using an alloy of CuGa, in the last sputtering using a target of Ga was tested.

3.1.1 CIGS growth using the hybrid system

The vacuum chamber where the growth was carried out is schematically represented in Figure 3-1. The base pressure of the chamber was 1 x 10^{-5} mbar but since there was no load-lock installed the vacuum was broken each time the substrate was replaced. Two magnetrons and two evaporators were installed in the chamber. On the first magnetron an In target was installed and on the second one, a Cu or CuGa target was installed. Ga pellets were used in the evaporator. The purity of the used materials is shown in Table 3-1. The sample holder was moveable so it could be positioned over the magnetrons or the evaporation source, it also has a coupled heater that enables the substrate temperature to change from room temperature up to 600 ºC. The temperature and power supplied to the heater were monitored using a thermocouple. Typical maximum temperatures were 580 ºC. At higher temperatures the bending of the substrate occurred. A Se evaporator was attached to the sample holder, therefore the distance between them was kept constant at 5 cm, regardless of any movement. High purity Se pellets were evaporated at temperatures of 255 °C and the heating rates were of 10 °C per minute for every situation. The depositions were performed at a pressure of 4.8 x 10^{-3} mbar and the sputter gas was Ar. Similar growth systems but without the EPD have been reported by other groups [114, 115].

More detailed information on the exact growth conditions for each method is presented in section 4.

Table 3-1: Purity of the used materials.

Elements	Purity
CuGa	99.99%
Cu	99.99%
In	99.99%
Sn	99.99%
Zn	99.99%
Se pellets	99.999%
Ga pellets	99.999%

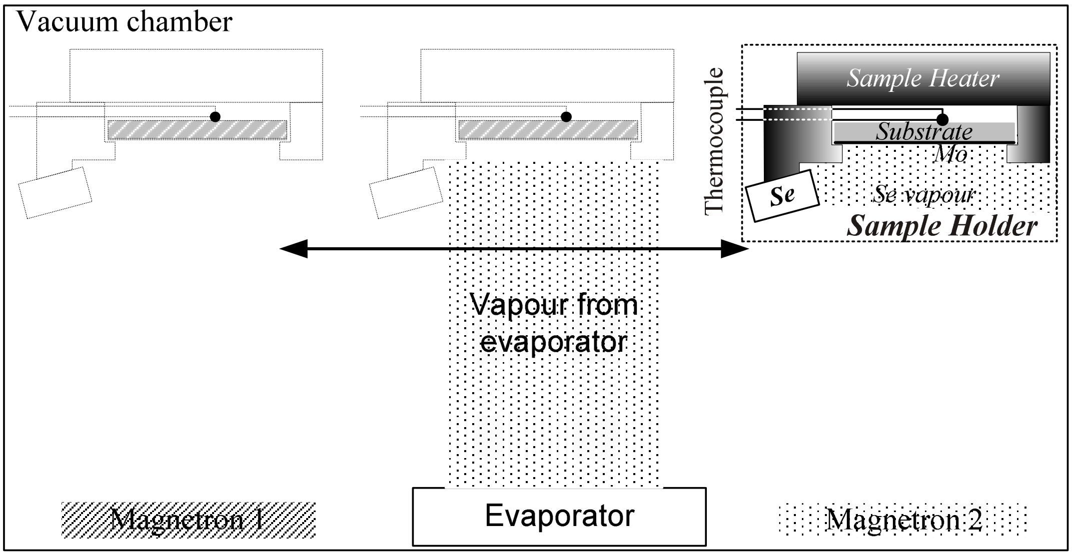

Figure 3-1: Schematic representation of the chamber used in the growth of the absorbers.

3.1.2 CIGS growth through Ga sputtering

In the traditional 2-step or 3-step methods to grow CIGS by co-evaporation, the control of the Ga quantity is possible because all elements are evaporated individually. The incorporation of Ga in the hybrid system can be a drawback, thereby sputtering from a target of Ga was tested. The advantage of using this method would be the ability to control the Ga quantity during the deposition which does not happen in traditional sputtering systems using only one CuGa target. There, the only way to control the quantity of Ga during the growth would be to use several targets with different quantities of Cu and Ga.

The problem arising from this method is that Ga is a liquid for temperatures above 32-36 ºC. After melting, Ga suffers from super cooling and keeps the liquid state down to temperatures as low as 15 ºC depending on the purity of the material. Considering the temperature conditions that the sputtering targets are exposed to, it is evident that Ga will be liquid during depositions. This raises a few questions, is it possible to sputter atoms from a liquid target and deposit a film? Is the liquid stable enough to allow the deposition? In the literature, there are the reports of Dunke et al. [116] and Beshenkov et al. [117] that reported the successful sputter of atoms from targets of a liquid In-Ga alloy and pure liquid Ga targets, respectively. However, these works make no reference to deposition of films. Ränsh et al. [118] report that after 200 ºC Ga is extremely reactive with steel and in the presence of RF plasmas it has the tendency to form round shaped droplets.

On the first depositions it was noticed that after a few minutes of sputtering at very low power settings, Ga started to change from solid to liquid, therefore it was necessary to take the target out of the chamber and cool it down with liquid nitrogen to ensure its solidification. In some attempts the power was kept on after the target melted and after a few minutes some round drops were formed leaving part of the magnetron exposed, see Figure 3-2. This was probably due to the strong surface tension of liquid Ga. After the power was turned off the droplets didn’t change shape or move. During the short period of time on which the drops were not formed, less than 4 minutes, there was a thin film of Ga deposited on the substrates. After the drops were formed, the sputtering power was turned off since the target holder was exposed to the plasma and it was being damaged.

This experiment showed that if there was a way to prevent the target holder to be exposed, then sputtering from a liquid Ga target would be possible. To do so, it would be necessary to have a mass of Ga sufficiently large so that its gravitic force would overcome its surface tension. Due to technical limitations such experiment was not done and therefore this technique to incorporate Ga into CIGS films was not used.

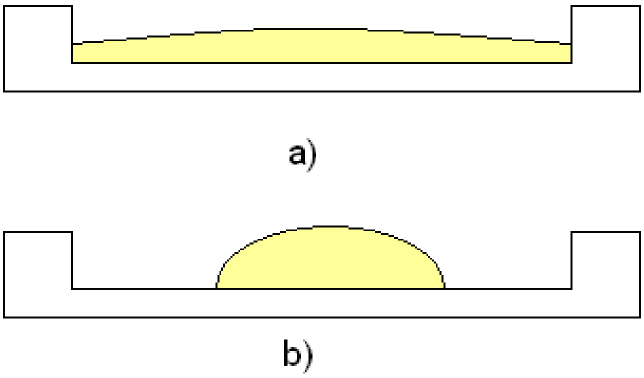

Figure 3-2: Cross section views of the Ga liquid target before a) and after the formation of the droplets b).

3.2 Growth of CZTSe

Two different methods have been tested for the growth of CZTSe, the hybrid method and selenization of metallic precursors. In the hybrid method the objective was not only to grow single-phased CZTSe but also to evaluate if an EPD signal was detected.

3.2.1 Growth of CZTSe using the hybrid method

For the hybrid growth, the same deposition chamber described before has been used. This chamber is schematically illustrated in Figure 3-1. The targets used were Cu and Sn whilst Zn was evaporated. The deposition of these three different materials was done sequentially. The description of each different profile is further explained in section 4. All the depositions were performed using a pressure of 4.8 x 10^{-3} mbar, a substrate temperature of 375 ºC, and Se was evaporated at 255 ºC.

3.2.2 Growth of CZTSe by selenization of metallic precursors

The growth of CZTSe by selenization of metallic stacked precursors was also studied. This growth method consists in two steps. The first step is the preparation of the metallic precursors and the second step is their selenization to form CZTSe.

The precursors were deposited by DC-magnetron sputtering on 3×3 cm^2 on Mo coated soda lime glass (SLG). The purity of the targets was N3 for Mo, N5 for Cu and N4 for Zn and Sn. The base pressure of the chamber was 5×10^{-6} mbar. All the precursors were deposited with the same settings, namely power density of 0.16 W.cm^{-2}, working pressure of 2×10^{-3} mbar and a substrate to target distance of 10 cm. Thicknesses were monitored with a crystal monitor Intellemetrics IL 150.

The selenization was done with elemental Se vapour thus avoiding the use of toxic H_2Se, and in the same chamber as previously described. Different combinations of substrate temperature, pressure and Se evaporation temperature were tested and the details for each study are presented in section 4.

3.3 Growth of CZTSSe

For the growth of CZTSSe, the only tested procedure was the selenization of precursors that already contained sulphur. Several types of films were selenized: binary sulphide precursors; ternary Cu_2SnS_3 + Zn/ZnS films and finally CZTS films. The growth method can be divided into four steps. Firstly two precursors are evaporated and in a second step are sulphurized to form CTS. The third step consists on the deposition of a Zn or ZnS layer by RF magnetron sputtering. In some cases a sulphurization was performed in order to from CZTS and then the fourth step was the selenization to form the CZTSSe layer.

In the first step, precursors were sequentially deposited on a Mo coated soda lime glass (SLG) in a PVD system, at the HZB, with elemental sources of Sn, S and Cu, therefore allowing the deposition of different sulphides. The deposition order was SLG/Mo/SnS_2/$Cu_{2-x}S$. During the Sn deposition, the temperature of the S source was 500º C, whilst the Sn source was kept approximately at 1200 ºC; the pressure during this step was 1.8×10^{-5} mbar. As for the $Cu_{2-x}S$ deposition, its temperature ranged from 1355 ºC to 1400 ºC at a pressure of 1.70×10^{-5} mbar. The whole process was controlled by time, after a calibration process which involved weighing the test samples. It was aimed at the deposition of 807 nm of $Cu_{2-x}S$ and 810 nm of SnS_2. These thicknesses should give a sample with a [Cu]/[Sn] ratio of 2.

In the second step, a tubular furnace was used. The schematics of that furnace are represented in Figure 3-3. The samples were heated in a N_2 atmosphere with a flow of 40 $ml.min^{-1}$, at an operating pressure of 10 mbar in order to avoid Sn losses by evaporation. The sulphur evaporation source was a quartz tube filled with elemental S pellets. The temperature profiles for the sample holder and for the S evaporator are shown in Figure 3-4. The profile shows the heating of the substrate and the sulphur evaporation starting at the same time. The S evaporator takes 25 minutes to reach 130 ºC and is kept there. Maximum substrate temperature, 525 ºC, is reached in 55 minutes. Then the sample is left at this temperature during 20 minutes and afterwards a natural cooling occurs. The S evaporator is turned off when the substrate reaches 375 ºC. Samples prepared in this process were named CTS since Cu-Sn-S ternaries were formed.

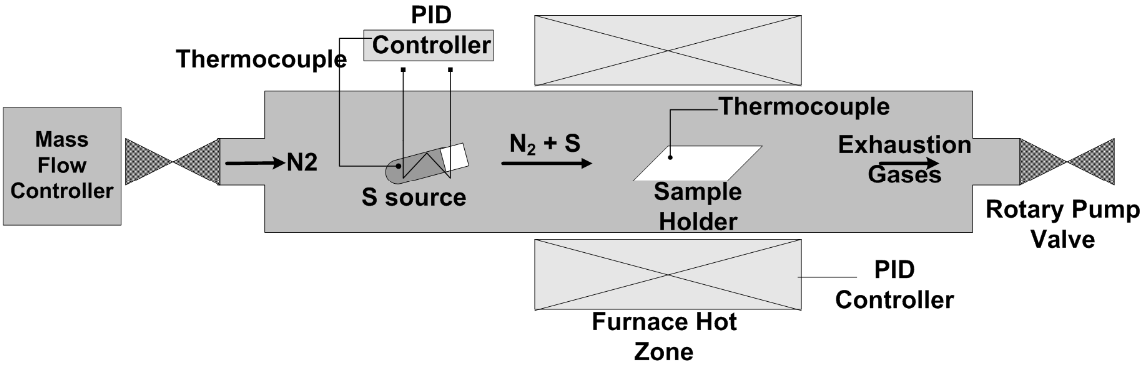

Figure 3-3: Schematic representation of the sulphurization furnace.

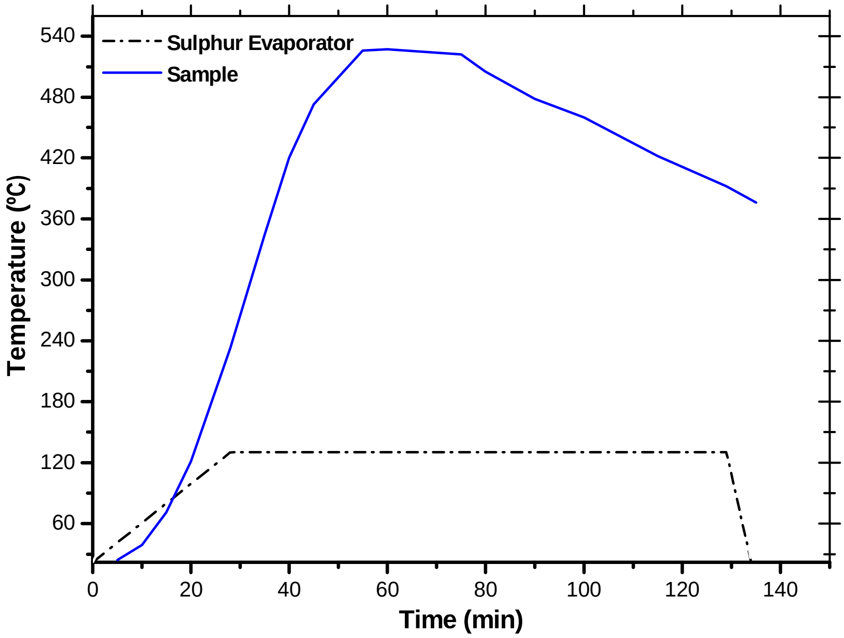

Figure 3-4: Temperature profiles of the S evaporator and the substrate holder for the formation of the CTS films.

In the third step, either Zn or ZnS was deposited by RF magnetron sputtering system. The deposition was performed using an Ar atmosphere at a working pressure of 2 x 10^{-3} mbar. The power density for Zn was 0.41 W.cm^{-2} and for ZnS 0.33 W.cm^{-2}. In situ thickness monitoring was assured by a quartz crystal monitor and it was aimed at the deposition of 220 nm of Zn or 570 nm of ZnS; the results were then confirmed by step profilometry. The sulphurization to form the CZTS was done in the tubular furnace with the same profile and the selenization in the chamber. The selenization profile and conditions were the same used to grow the best CZTSe films and will be described in section 4.

3.4 Removal of $Cu_{2-x}Se$ or $Cu_{2-x}S$ phases

To remove the highly conductive and unwanted $Cu_{2-X}Se$ phases, some films were subjected to KCN etching [119]. This procedure consisted of submitting the films for 2 minutes to the following baths: KCN 10% w/w, ethanol 50% v/v and finally deionised water. The KCN removes the unwanted phases while the other baths are for cleaning purposes. Afterwards the films were dried using a N_2 Flux.

3.5 Characterization techniques

3.5.1 Composition and morphology

The composition of the absorber layers was measured using energy dispersive spectroscopy (EDS). This technique is not very precise but for comparison purposes it is possible to draw useful conclusions. For the EDS measurements, the system used was a S4100 Hitachi electronic microscope equipped with a Rontec EDS system and a typical acceleration voltage of 25 kV was used. It was very important to use the 25 kV acceleration voltage because otherwise the system would not be able to distinguish between the Cu and Zn L_α lines since these emissions nearly overlap around 0.9 keV as it is shown in Figure 3-5. The solution is to use 25 kV as acceleration voltage and analyse the L_α-lines as well. For the CZTSSe samples, the quantity of sulphur is not possible to be measured since the Mo and S L-lines are superimposed. Scanning electron microscopy, SEM, was used for the analysis of the morphology of the surface and of the cross sections.

For the composition of the precursors, both EDS and inductively coupled plasma mass spectrometry, ICP-MS, have been used. The reasons why this was done are explained in section 4. An ICP-MS Thermo X Series was used for these measurements.

ICP-MS dilutions were made with a solution of inverse *aqua Regia*, which is a solution with a molecular ratio of 3:1 of nitric acid and hydrochloric acid.

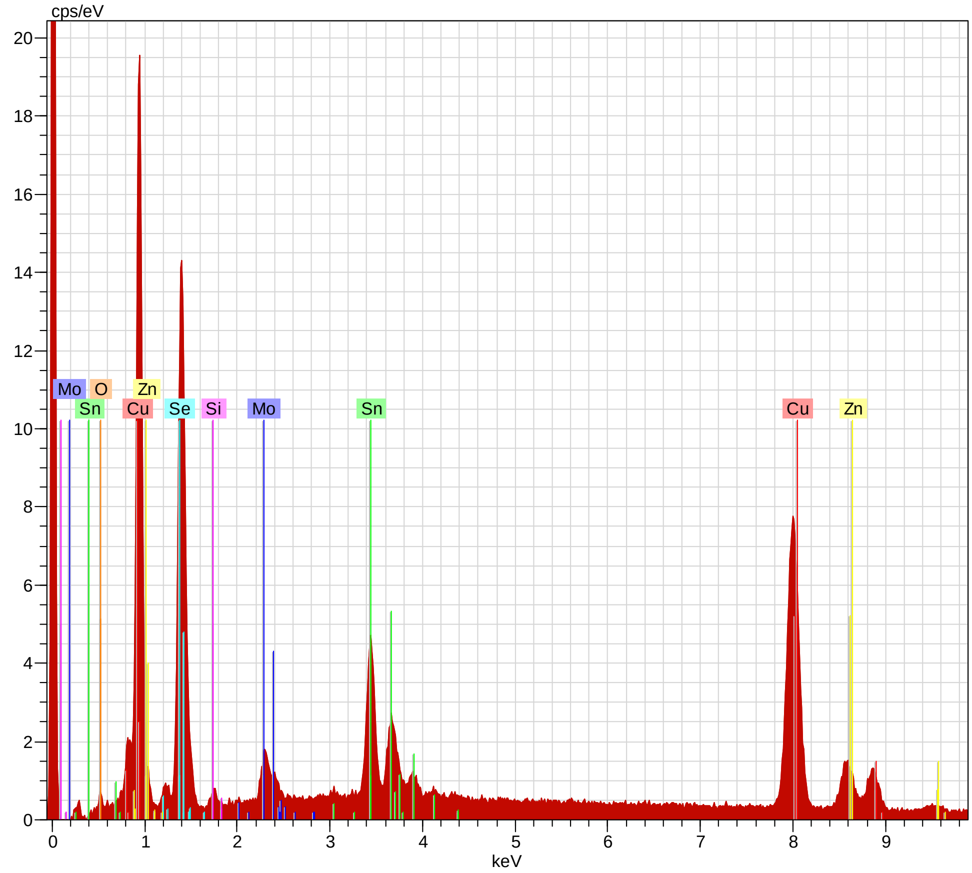

Figure 3-5: Typical energy dispersive spectrum for a SLG/Mo/CZTSe sample.

3.5.2 X-ray diffraction

X-ray diffraction (XRD) was used to identify the phases present in the films. To this end typical θ-2θ measurements were done with a PHILIPS PW 3710 diffractometer using the Cu-K_α line,1.5406 Å.

Texturing studies presented in this thesis were done by comparing the intensity ratios of the peaks of the experimental diffactrograms with the corresponding data from powders databases.

The lattice plane distances, d_{hkl}, are calculated using Bragg's law:

$$n\lambda = 2d\sin(\theta) \qquad \text{(eq 3-1)}$$

where n is an integer, λ the wavelength of the incident wave, d the distance between planes in the lattice and θ is half of the diffraction angle.

For the calculations of the lattice parameters a and c, the tetragonal relation where $a=b\neq c$ was used:

$$\frac{1}{d_{hkl}^{2}} = \frac{h^{2}+k^{2}}{a^{2}} + \frac{l^{2}}{c^{2}} \qquad \text{(eq 3-2)}$$

For the plane (2 2 0) c=0 and so a can be directly estimated. Then, c can be estimated using plane (1 1 2) accordingly to the following equations:

$$a = \sqrt{8}d_{220} \qquad \text{(eq 3-3)}$$

$$c = \sqrt{\frac{4}{\left(\frac{1}{d_{112}^{2}} - \frac{1}{4d_{220}^{2}}\right)}} \qquad \text{(eq 3-4)}$$

These planes were chosen not only to simplify the calculations but also because they correspond to the two most intense peaks and for that reason errors are minimized. From these relations, the parameter *c/2a* can be calculated as well. For the tetragonal structure, *c/2a* gives additional information regarding the form of the unit cell.

3.5.3 Raman scattering

In addition to XRD, Raman scattering was used as a complementary technique to identify the phases present in the studied films. Raman scattering is a technique based in the coupling of the incident light with the vibrating modes of the crystal lattice or phonons. Because this interaction depends strongly on the energy of the phonons and this changes from phase to phase, Raman scattering may be used to identify different phases.

The system used in this work was a Jobin-Yvon T64000 Raman scattering system with an Olympus microscope equipped with a 100 X magnifying lens in the backscattering configuration. The excitation source was an argon ion laser typically operating at the wavelength of 488 nm and with 180 mW output power.

For a semiconductor, the effective light penetration depth, *d*, is roughly evaluated by $d = 1/\alpha$, where α is the absorption coefficient. In the case of Raman scattering analysis using the back scattering configuration, one must consider that the light hast to return and therefore the equation is then $d \sim 1/(2\alpha)$. Using this equation and knowing α, one can roughly estimate the depth to which the Raman scattering analysis extends when using different excitation laser wavelengths. Such estimations are presented in Annex A for CZTSe and Annex B for CZTS.

3.5.4 Photoluminescence

Photoluminescence measurements were performed at various temperatures, from 5 K to 300 K, using a Fourier transform infrared spectrometer Bruker IFS 66v equipped with a Ge detector cooled down to liquid nitrogen temperature. The 488 nm line of an argon ion laser was used as excitation source. These measurements allow a better identification of the band gap energy and possibly the identification of some defects located inside the band gap.

3.5.5 Reflection and transmission

Reflection and transmission measurements were done using a Shimadzu UV3600 spectrophotometer equipped with an integrating sphere. These measurements allow one to estimate the band gap value of the absorbers when grown on SLG. The absorption coefficient, α, is given by:

$$\alpha = \frac{-1}{w} \ln \left[\frac{-(1-R)^2 + \sqrt{(1-R)^4 + 4T^2R^2}}{2TR^2} \right] \qquad \text{(eq 3-5)}$$

where, w is the thickness of the sample, R the reflectance and T the transmittance [120]. For a direct band gap semiconductor [30,120]:

$$\alpha \propto \left(h\nu - E_{gap}\right)^{1/2} \qquad \text{(eq 3-6)}$$

where ν the radiation frequency, h the Plank's constant and E_g the band gap energy. Then, with both equations and by using the linear fit of $(\alpha.h\nu)^2$ v.s. $h\nu$ we obtain the value E_{gap} from R and T. This procedure is known as Tauc's method [121].

An alternative method to estimate the band gap energy relies on the use of diffuse reflectance data alone. In this method, it is considered that in the absorbance region T=0 and the maximum value, R_{max}, of diffuse reflectance, R_{diff}, roughly corresponds to a point of nearly zero absorbance, A:

$$A = R_{\max} - R_{diff} \qquad \text{(eq 3-7)}$$

The band gap energy is then obtained by extrapolating the absorbance curve until it intercepts the zero line [122]. In order to obtain more precise values it is necessary to implement Murphy's model derived from the Kubelka–Munk model [123], however given the greater complexity that was not done in this thesis.

3.5.6 Current-voltage measurements

Current-voltage measurements were done to estimate solar cell electrical parameters. These were performed in a system that measures current and voltage. It uses a tungsten-halogen lamp to simulate the Sun's light. To calibrate the system for the 1000 W/m^2 [4], a calibrated silicon cell was used. To test if the system gave accurate measurements, a comparison, between measurements performed in Aveiro and

---

[4] Standart measurement conditions, AM1.5 global.

measurements made at ETH[5] and at HZB was carried out. A CIGS solar cell presented an efficiency of 12.3% at the ETH and 12.1 % in Aveiro. A CZTS solar cell showed the same efficiency, 1.4% in Aveiro and at the HZB. The variations were mostly due to the differences in the illumination rather than from how the electrical measurements were done.

A typical current density versus voltage curve from where the solar cell parameters can be estimated is shown in Figure 3-6.

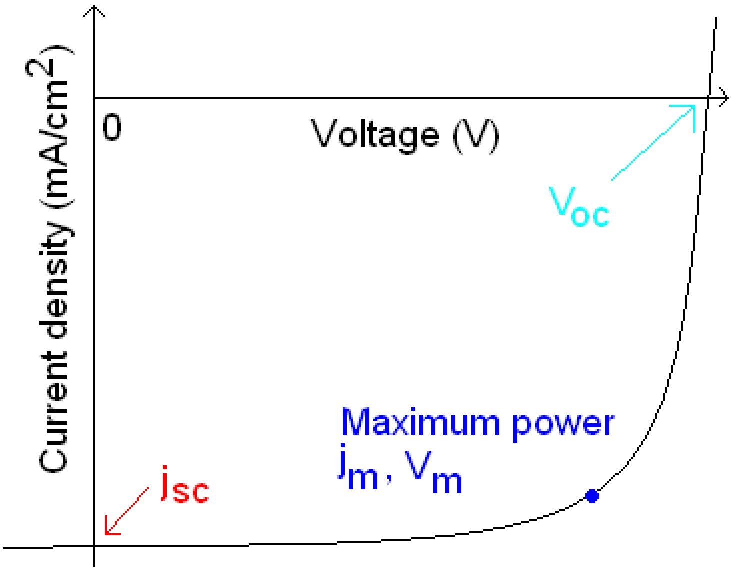

Figure 3-6: Current density versus voltage characteristic behaviour for a solar cell. j_{sc}, V_{oc} and the maximum power point are shown.

---

[5] Swiss Federal Institute of Technology, Zurich.

4 Properties of the new absorber materials

4.1 CIGS

The growth of CIGS was executed using the hybrid method in two different processes with the purpose of studying possible ways to incorporate Ga in a controlled manner into the structure. In the first one, this was done through evaporation of Ga and in the second through sputtering from a CuGa target.

4.1.1 Growth of CIGS using evaporation of Ga

In this study, the deposition of CIGS was carried out using the hybrid system with sputtering of Cu and In and evaporation of Ga and Se. The used deposition sequence was an adaptation of a two stage process which provided the more crystalline films [II, III]. First, a 40 nm thick layer of In was deposited. This was done in order to prevent direct selenization of Mo since contradictory studies on the influence of $MoSe_2$ have been reported [124, 125] . Afterwards the temperature of the Se evaporator was ramped up to 255 ºC. After this step, Cu was sputtered during 30 minutes followed by Ga evaporation during another 30 minutes. Afterwards, the temperature of the substrate was ramped from 300 ºC up to 580 ºC and In was sputtered. Se was evaporated at 255 ºC and Ga at 950 ºC. An example of the substrate heater power profile is shown in Figure 4-1 and the description of the highlighted steps is found in Table 4-1. In all the cases where Ga was deposited right after In, the sample would peel off. It is worth noticing that between point f and g there is a decrease of the power needed to sustain the 580 ºC as seen by the decreasing line and between point g and h the line is horizontal what means that the end point detection is seen. So, the EPD is seen at point *g* and afterwards it was deposited an additional 10 % in time of In in order to obtain the desired Cu-poor film. The following studied samples were grown with a similar profile.

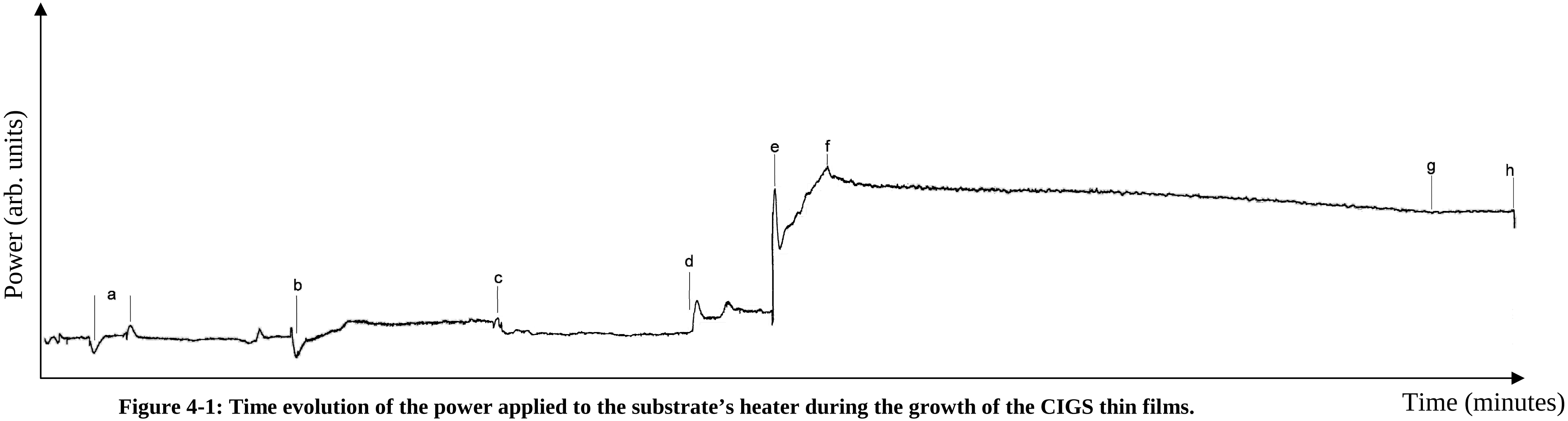

Figure 4-1: Time evolution of the power applied to the substrate's heater during the growth of the CIGS thin films.

Table 4-1: Description of the substrate heater power profile.

	Time (minutes)	Description of the step
a	5	deposition of In, substrate temperature at 300 ºC
a-b	20	ramp of Se evaporator to 255 ºC
b-c	30	sputtering of Cu
c-d	25	evaporation of Ga at 950 ºC
e		start of In sputtering and substrate temperature ramp up to 580 ºC
f		power overshoot due to the temperature controller
g		end of transition
e-h	90	sputtering of In

In Figure 4-2 a) and b) the SEM micrograph of the surface of two selected CIGS samples grown with evaporation of Ga are shown. In those figures one can see two different films, the one in Figure 4-2 a) although with an open structure shows less voids than the one in Figure 4-2 b). In both cross section micrographs, Figure 4-2 c) and d), the films appear to be more compact than showed in the surface micrographs and they both appear to have smaller crystallites at the bottom than at the top. This difference in the crystallite size may be due to nucleation because of the proximity to the Mo or due to change of chemical concentration. It is known that Ga has the tendency to accumulate at the back of the films [33] and induces smaller grains [126]. The chemical composition of the films is shown in Table 4-2 and it reveals films with similar composition. Both samples are Cu-poor, as predicted by the EPD, with values of [Cu]/([Ga]+[In]) close to 0.9 which means that the EPD signal seen is real and not an artefact. Sample 2 appears to have slightly more Ga than sample 1, because [Ga]/([In]+[Ga]) takes the value 0.1 for sample 1 and 0.2 for sample 2. These differences are not big enough to reveal a real difference since the samples have deviations in the morphology and that affects the EDS signal significantly. Sample 2 showed a [Se]/[meta]l ratio of 1 which indicates that the film is fully selenized whereas sample 1 only has a value of 0.9 which may indicate some lack of Se.

Table 4-2: Atomic ratios for the CIGS studied samples grown with evaporation of Ga.

Atomic ratios	**sample 1**	**sample 2**
[Cu]/([Ga]+[In])	0.9	0.9
[Ga]/([In]+[Ga])	0.1	0.2
[Se]/metal	0.9	1.0

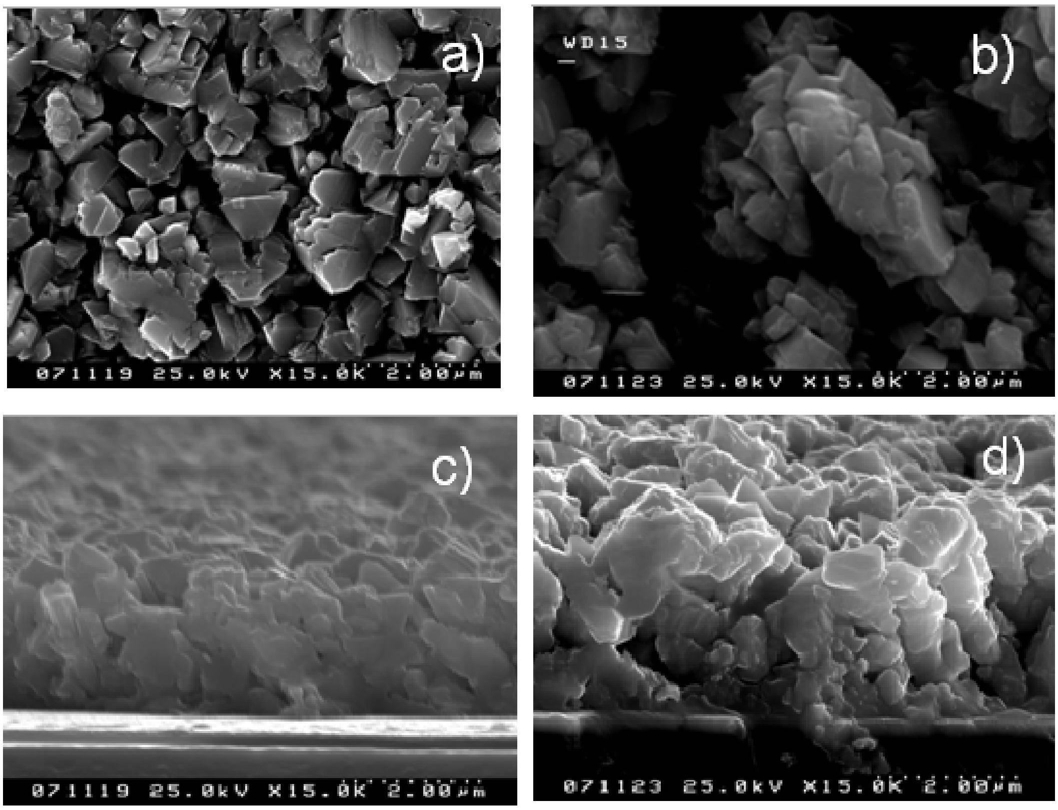

Figure 4-2: a) and b) SEM micrograph of the surface of samples 1 and 2, respectively. c) and d) cross section image for of samples 1 and 2, respectively.

Raman scattering analysis, not shown here, showed that both films had the chalcopyrite structure. This analysis only showed the CIS peak at 175 cm^{-1}. This is an indication that very little Ga is found at the surface since the CIGS main peak shifts to higher energies with higher Ga concentration. Such evidence can also be drawn from Figure 4-3 that shows a transition in the reflectance around 1250 nm which corresponds to 1 eV. If some Ga would be present at the surface, then it would be expected to see a transition at a lower wavelength due to the raise of the band gap energy. XRD measurements would be needed to evaluate the content of Ga in the film, but the XRD system was not available at the time and it was decided to process the film to solar cells rather than waiting.

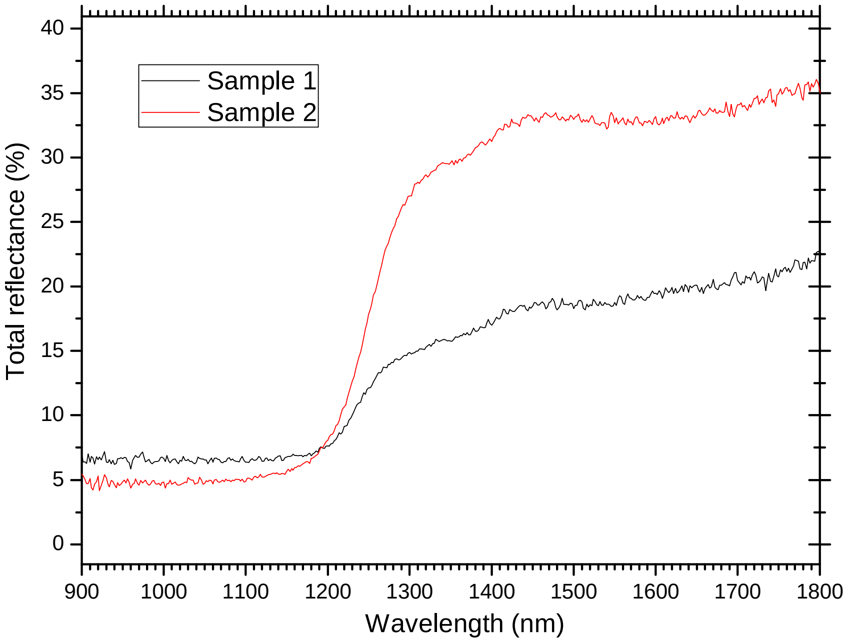

Figure 4-3: Total reflectance of the two analysed CIGS films.

In section 5.2, just one solar cell result is shown for this set of films. This was partly due to the fact that the deposition of the TCO was already poor at that time. Most of the cells made had a TCO with a large resistance, sheet resistivities higher than 500 $\Omega_{\square}$, and so the cells were poor with most of efficiencies in the range of 1-3%. Despite that problem, the hybrid system with evaporation of Ga was capable of growing CIGS films with some reproducibility in composition.

A Cu-poor to Cu-rich growth was tested in order to try to improve the grain size, but the EPD signal was too low to have a reproducible way to growth the films. Different steps and profiles were studied but the described previously was the best one.

4.1.2 Growth of CIGS using a CuGa sputtering target

In this study, the incorporation of Ga was made by sputtering from a CuGa target with 25% of Ga. The used deposition sequence was the same as the described in the previous chapter but without the evaporation of Ga. The transition corresponding to the EPD signal was much lower and so the control was worse.

The first results were disappointing since Ga had the tendency to accumulate to the back of the film. In fact, in most of the films the EDS measurements gave such low values of Ga that practically the system was not receiving any Ga signal. In order to understand if

Ga was disappearing or not, EDS measurements on the back side of the film were performed. The samples were prepared by scratching off parts of the film onto a conductive tape. The EDS measurements then showed a high content of Ga, with a ratio of [Cu]/[Ga] near 2. The composition of the target for the same ratio would be 3. Such high value shows that Ga accumulated at the back of the film and would even probably form a $CuGaSe_2$ layer. Once again, to clarify this point XRD analyses would be needed but were not accessible at the time. The Raman scattering analysis of the surface of the films, not shown here, revealed only CIS to be present with the typical Raman scattering CIS peak at 175 cm^{-1}.

From this set of samples, the only sample where there was some high content of Ga detected by EDS at the surface, was the one presented in Figure 4-4. The likely reason why some Ga was seen was the open structure that the sample revealed. By looking at both the surface and the cross section, it is visible some columnar grains that leave voids in the film exposing the back part. The composition of this film is shown in Table 4-3 and it reveals a Cu poor film with a replacement of less than10% of In for Ga. The [Cu]/[Ga] ratio is 8.6 but the value for the target is 3, this means that even with this open voided structure, some Ga is still hidden to the EDS analysis.

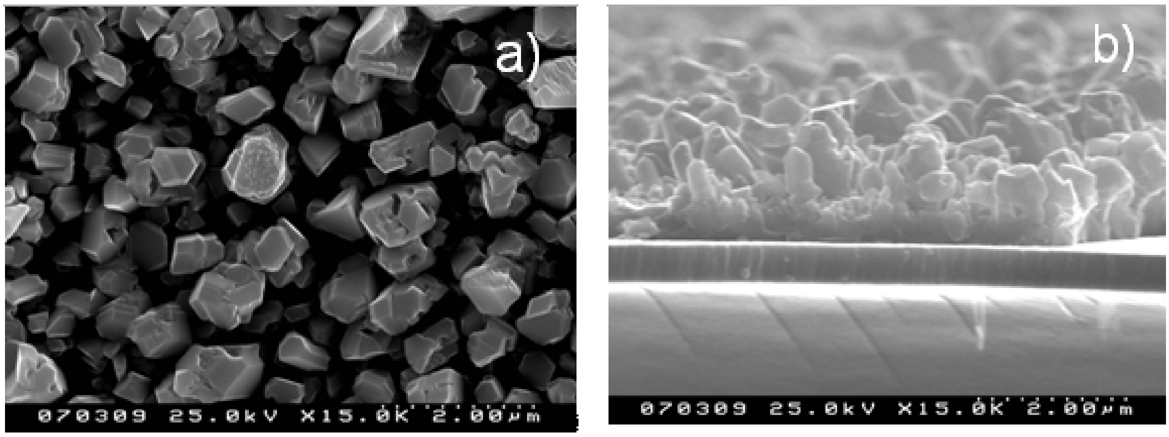

Figure 4-4 a) SEM micrograph of the surface and b) cross section of a CIGS sample grown with a CuGa target.

Table 4-3: Atomic ratios for the CIGS samples grown with a CuGa target.

Atomic ratios	
[Cu]/([Ga]+[In])	0.8
[Ga]/([In]+[Ga])	0.1
[Se]/[metal]	0.9
[Cu]/[Ga]	8.6

The total reflectance spectra of the studied sample is shown in Figure 4-5 and as in the previous samples, the band gap energy transition is located around 1200 nm which corresponds to values around 1 eV confirming that the surface is mostly CIS.

In order to try to have more Ga in the front of the film, it was tried to grow CIGS films using the inverse 2-stage method, i.e. start with a long deposition of In followed by CuGa. In this case the transition seen would be from Cu-poor to Cu-rich. To place the film back to the desired Cu-poor state, an additional layer of In was deposited at the end with duration being 10% of the initial deposition. Several runs were made but in this configuration, the EPD signal was hardly detected and so the control of the composition of the films was non-existent. Due to this no films with the desired composition were grown.

For this Ga incorporation test, due to the poor results, no solar cells were prepared.

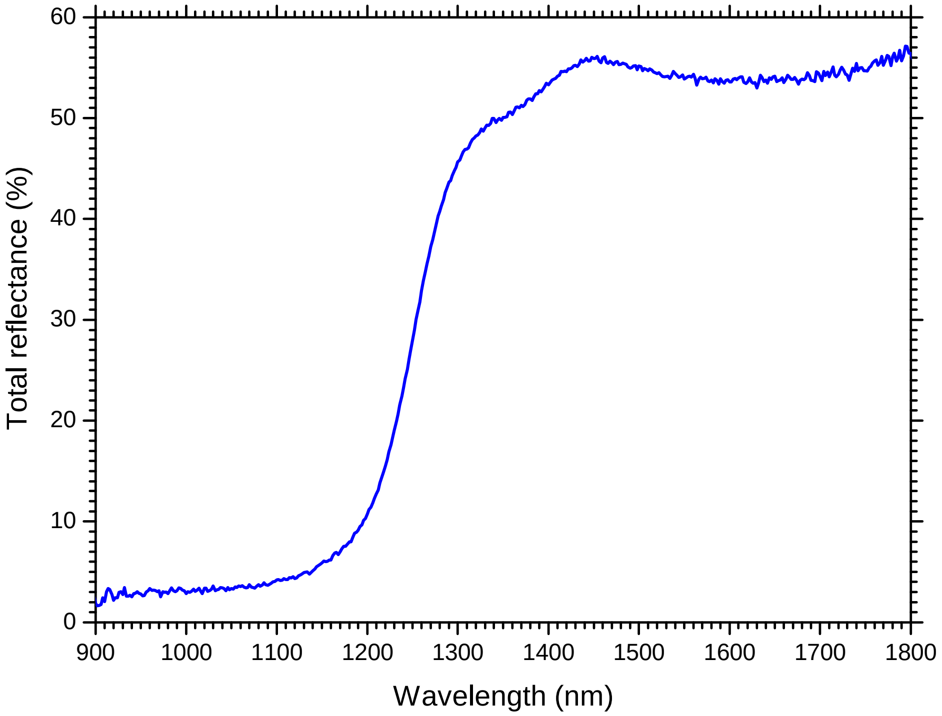

Figure 4-5: Total reflectance for the CIGS films grown with a CuGa sputtering target.

4.2 CZTSe

4.2.1 $Cu_2ZnSnSe_4$ by selenization of precursors

When the author decided to grow CZTSe films little thermodynamic data about the growth of CZTSe could be found in the literature. In addition the few research papers published at that time addressed several different growth conditions, namely temperature and pressure, without a systematic approach. Therefore, it was necessary to study at which temperature and pressure CZTSe could be grown. To tackle this issue, the first method tried was the selenization of metallic precursors.

In one of the few papers studying the growth of CZTSe, Friedlmeier et al. [127], it was reported that the growth of this compound by evaporation was done with poor adhesion to the substrate and with an open structure [28, 127]. Considering these problems the initial idea was to prepare the CZTSe films by a two-step method, where the first step was the preparation of metallic precursors, followed by a second step which consisted of the selenization of the precursors to, consecutively, form the CZTSe. There was already some work done about CZTS regarding the quality of precursors that indicated that there was a strong influence of the precursors' morphology in the CZTS final film quality [128]. Having this in mind it was decided to deposit the precursors by DC magnetron sputtering. Films deposited by sputtering usually are compact and uniform, thus it was hoped to obtain compact precursor films.

4.2.1.1 Preparation of precursors

The successful growth of CZTSe required reproducible deposition of precursors with controlled composition. The desired composition was Cu-poor, with [Cu]/([Sn]+[Zn]) ~ 0.9 and Zn-rich with [Zn]/[Sn] ~1.2 which was the same composition for what Katagiri et al. has the best solar cells [81]. Assuming bulk mass densities and using molar mass values for each element, initial thicknesses of the films were estimated and later deposited.

The first problem encountered was the deposition of Zn. The deposition of this material proved to be unstable, i.e. from one sample to another, during the same round of depositions, the thicknesses of the films could not be predicted either by the crystal monitor or by deposition time. Each round of depositions had four samples deposited sequentially. After the end of each round the vacuum chamber was opened to change the sputtering target. The exact cause of the variation was never identified but it was minimized by cleaning the surface of the target at every round of depositions and by minimizing the air exposure time. The likely cause of this instability was an oxidation of the surface due to the exposure to air. Due to this problem, the thickness of the samples grown at each position changed slightly. This however could be corrected because the deposition of Sn and Cu were reproducible and so the control of the final thickness was possible.

A characterization of the precursors was required for the optimization of the composition since initially it was assumed that the mass density of bulk samples is the same as that of the films, however, this is not true due to roughness. The first samples were characterized by EDS even though it was known that the EDS composition estimation is only valid for samples that are flat and homogeneous. This is a case where the samples may be considered flat, but are not homogeneous in depth due to its layered structure and therefore it is expected that the EDS measurements will be flawed. However, since EDS is an easy and fast technique to use, it was important to see whether measurements would have a big error due to the stacking or not. The ratio of the thicknesses, Cu/(Sn+Zn), and the composition ratio [Cu]/([Sn]+[Zn]) given by EDS of this set of precursors are presented in Table 4-4. The thicknesses were measured using a step profiler. Due to the Zn deposition problem and the composition correction, the four films have different total thicknesses. The results show that for the thicker samples, the EDS yields a higher concentration of Cu when comparing with Sn and Zn while, in fact, the ratio of the thickness shows that there is actually less Cu when comparing with Sn and Zn for the thicker films. These variations are more visible in the double axis plot of Figure 4-6. The figure shows evidence that EDS measurements are being affected by the layered structure since the thickness ratio lowers while the EDS ratio increases with increase of the total sample thickness.

Table 4-4: Total thickness, ratio of the thicknesses (Cu/(Sn+Zn)) and the composition ratio given by EDS of the first set of precursors deposited in the following order SLG/Mo/Zn/Sn/Cu.

Sample	Total thickness (nm)	Thickness ratio Cu/(Sn+Zn)	EDS composition ratio [Cu]/([Sn]+[Zn])
1	810	0.37	1.2
2	955	0.37	1.4
3	1110	0.34	1.6
4	1165	0.35	1.7

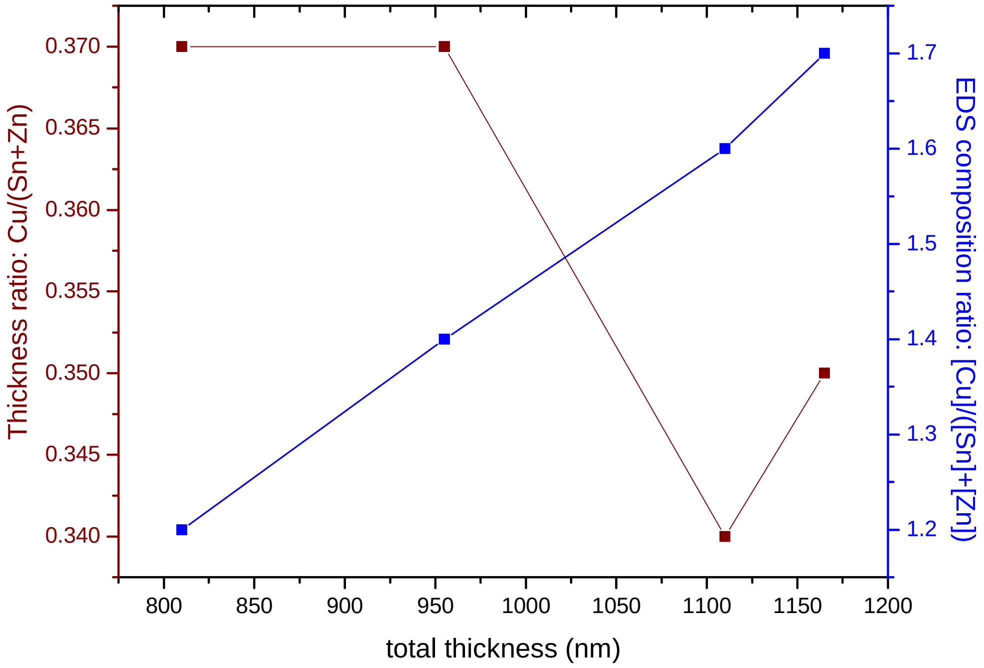

Figure 4-6: Variation of the thickness ratio Cu/(Sn+Zn) and EDS ratio [Cu]/([Sn]+[Zn]) as function of the total thickness for four precursors.

Simulations using the Casino software [129] showed that most of the energy of the incident electrons is absorbed in the Cu layer. In Figure 4-7 it is represented the cross section of an energy absorption iso-energetic mapping for a 25 keV beam of electrons in a structure similar to the one of sample 4 in Table 4-4. Inside the yellow line, which is enclosed by the Cu layer, 50% of the energy of the incident beam is absorbed, and that is why the Cu composition appears to be larger in films where the Cu top layer is thicker. As a result, it is not possible to estimate the elemental composition of the precursors for this layered structure using EDS.

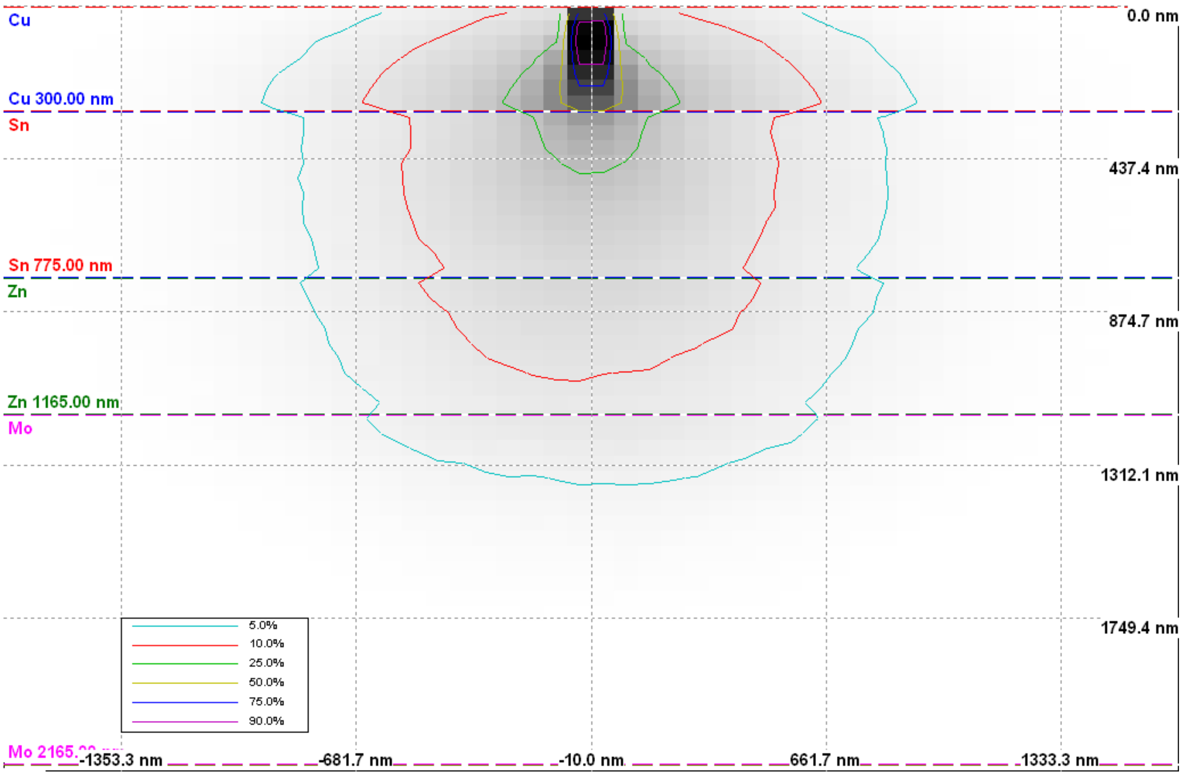

Figure 4-7: Cross section of an iso-energetic mapping for an incident 25 keV beam of electrons simulated using CASINO software. The simulated structure is a stacked precursor with the following order: Mo/Zn/Sn/Cu. The iso-energetic lines represent the energy that is outside the area of the curve. For instance, for the red line, only 10% of the non absorbed energy is outside of this line and 90% of the observed energy is inside of this volume.

The final composition of the films could be controlled if a calibration of the thicknesses ratio measured by the profiler and the final composition of the film was set. Once this was stabilised no further measurements of the composition of the precursors would be required. Another technique that can provide information on the composition of the samples was needed. For this, ICP-MS was chosen. A set of samples with different thickness was prepared. In Figure 4-8 is presented the ratio [Cu]/([Sn]+[Zn]), determined by ICP-MS, versus the thickness ratio, Cu/(Sn+Zn). The plot shows that there is a correlation between the thickness ratio and the composition ratio. It is then possible to control the elemental concentration ratio using the thickness ratio. Samples that have a thickness ratio, Cu/(Sn+Zn), between 0.21 and 0.23 have a compositional ratio,

[Cu]/([Sn]+[Zn]), between 0.85 and 0.95 and therefore the mean value, 0.22, was the aimed value. Furthermore, the same thing was done for Zn and Sn but since the roughness of these layers is greater than the Cu one, there are greater errors when measuring the thickness of these layers and the correlation between the thicknesses and the composition is to some extent lower. Regardless of this, the control of the elemental composition using thicknesses is still possible.

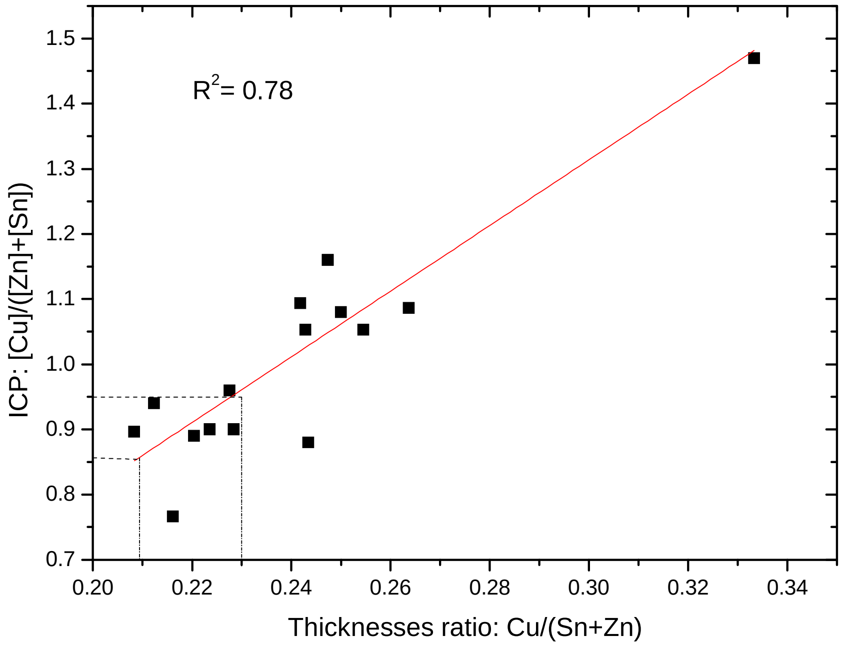

Figure 4-8: Composition ratio, [Cu]/([Sn]+[Zn]), estimated by ICP-MS versus the thickness ratio, Cu/(Sn+Zn). The points between the dashed lines, have the desired composition.

4.2.1.1.1 Order of the precursors

For the CZTSe studies no optimization of the order of the precursor stacking has been done, however, this has been done for CZTS in a parallel work. Two different stacking orders have been studied; Mo/Zn/Cu/Sn and Mo/Zn/Sn/Cu [VI]. In practice, the Zn deposition shows some instability and in light of this situation to have the desired precursors' composition, it was decided to always have the Zn next to Mo. This way the composition could be corrected by varying the thickness of Sn and Cu according to the Zn variation. Furthermore, since Zn is the most volatile of the three elements, it is convenient to have it at the bottom of the stack to minimize its loss during sulphurization or selenization. Since the sulphurization method, applied in this study, is similar to the selenization process and there are similarities between CZTSe and CZTS, it was followed the same stacking order that the study suggested to be the best one, Mo/Zn/Sn/Cu. It must be pointed out that this latter order, when compared with the order Mo/Zn/Cu/Sn showed that the Cu layer at the top could lower the losses of both Zn and Sn during the heating process. It was also pointed out [III] that the Cu atoms were the first to diffuse in the layers, which is a typical case of the Kirkendall effect [130]. In this situation, having the Cu at the bottom could increase the roughness of the samples because it has the tendency to diffuse into the other layers.

4.2.1.1.2 Properties of the precursors

The average roughness values of the resulting films deposited by DC magnetron sputtering are presented in Table 4-5. These results show that Zn and Cu are quite smooth, with values of average roughness between 10 and 40 nm for Zn and between 1 to 10 nm for Cu. Sn is quite rough with values varying from 40 to 100 nm.

Table 4-5: Roughness of metallic layers deposited by DC magnetron sputtering on SLG.

Compound	Average roughness (nm)
Zn	10-40
Sn	40-100
Cu	1-10

In Figure 4-9 a) and b), the SEM micrograph of the surface of a Zn layer grown on SLG is shown. The Zn layer shows a smooth, compact surface with grains smaller than 100 nm. Figure 4-9 c) and d) show the surface of a Sn layer grown on SLG and a rough surface is present. Large crystallites are visible, they can be as big as 2 μm. For the Cu layer no images are shown because the SEM's resolution is not big enough to reveal any features in the surface. In Figure 4-9 e) and f), the surface of a precursor with the order SLG/Mo/Zn/Sn/Cu is shown. The similarities between the Sn layer and the final precursor are evident which proves that the morphology of these precursors is rough due to the rough

Sn film. These SEM micrographs are in accordance with the results of the roughness measured using the profiler. Both methods show that the Sn layer is the one roughest one.

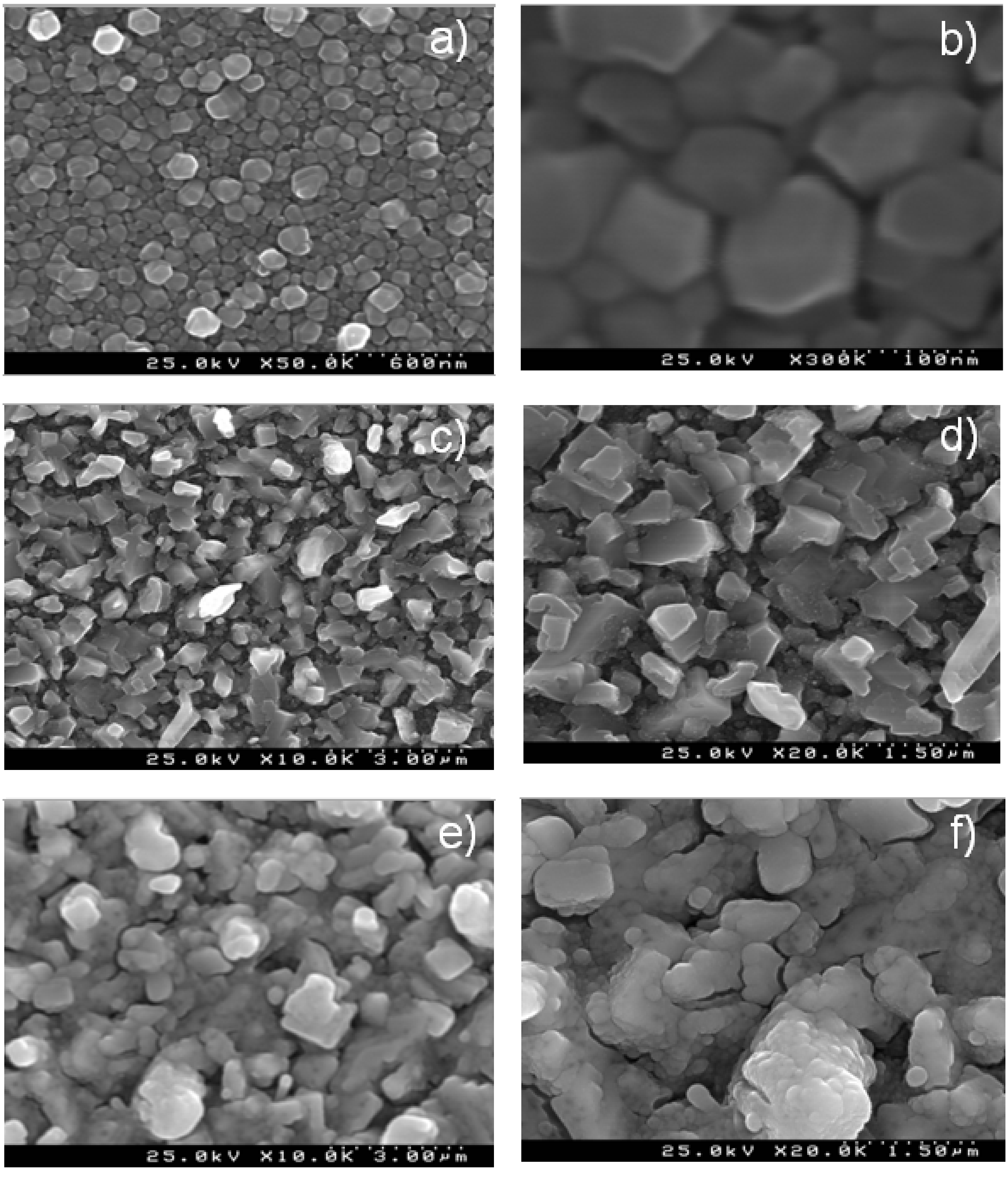

Figure 4-9: SEM micrographs of the surface of the precursors. a) and b) Zn on glass. c) and d) Sn on glass. e) and f) precursors with the stacking Mo/Zn/Sn/Cu.

Several tests have been conducted in order to try to lower the roughness of the Sn layer, namely by varying the deposition pressure and the substrate-to-target distance, but no gains were obtained with these variations. In the case of the pressure, several samples were deposited at 1 x 10^{-3} mbar, 2 x 10^{-3} mbar, 6 x 10^{-3} mbar, 8 x 10^{-3} mbar and 10 x 10^{-3} mbar. The standard deposition was made at 2×10^{-3} mbar and was the one with the lowest roughness. A possible way to lower the roughness would be to deposit the layer using RF-sputtering instead of DC-sputtering. Since for the same power the sputtered atoms with RF are ejected with lower energy than with DC, it is likely that the roughness of the layer decreases. During this work, depositions of Sn by RF-sputtering were tested and confirmed to have a lower roughness, however an extra RF source was not available to be installed.

The XRD diffractogram of a precursor is shown in Figure 4-10, and the following phases are present: hexagonal-Zn, tetragonal-Sn, cubic-Cu, bronze $Cu_{6.26}Sn_5$ and brass Cu_6Zn_5. Cu atoms are sputtered with enough energy to react with Sn and Zn and form bronze and brass. No phases of Zn and Sn are present so these do not react during the deposition of the precursors.

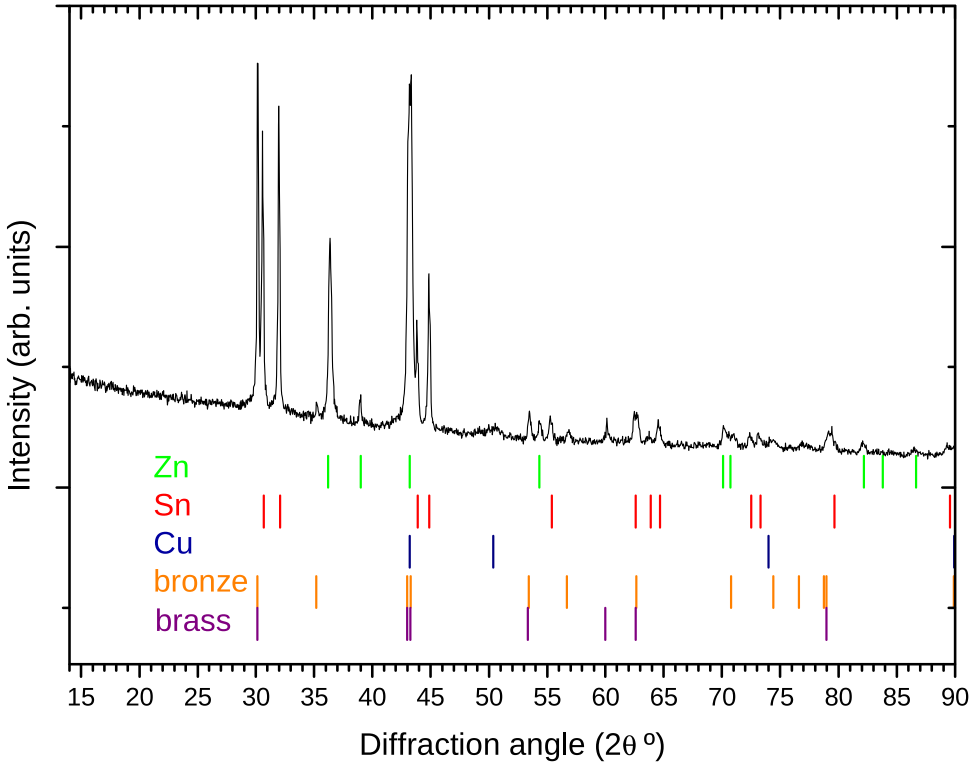

Figure 4-10: XRD diffractogram of a precursor with the following order SLG/Mo/Zn/Sn/Cu. The analysis confirms the presence of the following phases: Zn, Sn, Cu, bronze and brass.

4.2.1.2 Precursors' selenization temperature profile

The goal of this initial study was to establish the influence of the temperature of selenization on the properties of the films. By temperature of selenization we mean substrate temperature. The final objective of this study was to establish the minimal temperature for which single phased CZTSe can be grown.

The precursors were prepared as described before and in the following order: SLG/Mo/Cu/Zn/Sn. They were Cu-poor and slightly Zn-rich with similar thicknesses among them. This test was done before knowing the influence of the precursors' order and that is why the order is different than the other selenizations. In this initial test, 5 precursors were prepared. The heat treatment was started by raising the substrate temperature from room temperature to 150 °C and held at that temperature for 30 min. After this step, the temperature of the Se source was raised to 255 °C, and held there for 30 min. Finally, the substrate temperature was raised to the final value and again held there for 30 min. This heating profile is represented in Figure 4-11, in this case, the maximum temperature was 375 ºC, and afterwards the sample was cooled down naturally.

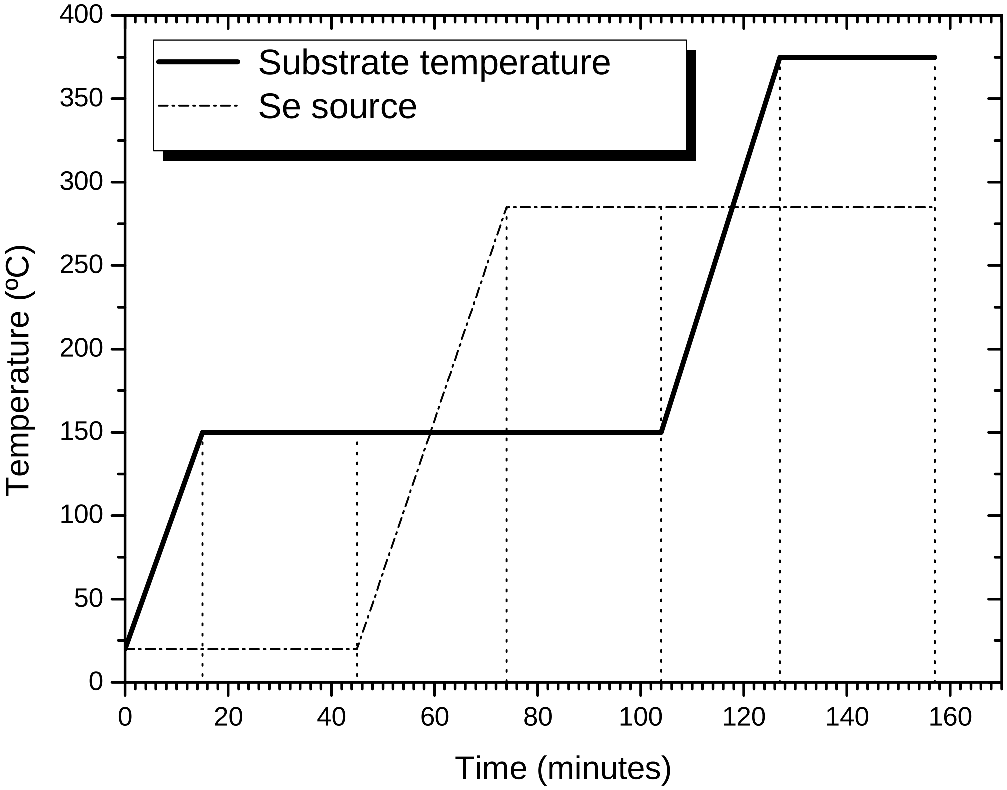

Figure 4-11: Temperature profiles for the selenization process.

The profile was chosen in order to first deposit Se onto the layers and then, with the last temperature increase, form the CZTSe. Elemental Zn and SnSe have low temperature values for a vapour pressure of 10^{-4} mbar, see Table 4-6, and therefore it is likely to occur some losses at high temperatures. This is in agreement with previous works [28]. From those two materials, Zn is the most critical one and therefore the profile described before was chosen to minimize Zn losses by selenization of the layers before the last substrate temperature increase. For the maximum substrate temperature it was used: 200 °C, 255 ºC, 300 °C, 350 °C and 400 °C. The samples were named after their maximum temperature: Se200; Se255, Se 300; Se350 and Se400. All the samples were grown at a pressure of 5 x 10^{-5} mbar.

Table 4-6: Temperature for 10^{-4} mbar of vapour pressure [131].

Element	Temperature (ºC)
Zn	250
Sn	997
ZnSe	660
SnSe	400

SEM images for samples Se255, Se300, Se350 and Se400 are displayed in Figure 4-12. With the temperature increase, it seems that the films are more crystalline and more compact. In the sample Se255, Figure 4-12 a), there are some visible voids. The number of voids tends to decrease with increasing temperature as well as its apparent depth. In sample Se400 almost no dark areas are visible which means that there are few voids and if any they are not as deep as in sample Se255.

By analyzing the films' composition and elemental ratios, Table 4-7 and Table 4-8, it is perceptible that the quantity of Se in the films increases with temperature. But with the temperature increase there are also Sn and Zn losses. These losses are reflected in the increase of the ratio [Cu]/([Zn]+[Sn]). The selenization at low temperatures is preventing the losses of Zn since [Zn]/[Sn] increases, this means that Sn losses are greater than Zn losses. The losses of Sn at 400 °C are in agreement with results reported by others [28, 127]. It is evident that following this procedure at even higher temperatures and at this pressure will not produce CZTSe due to the losses of both Sn and Zn [IV].

Table 4-7: Composition of the films for samples Se200; Se255; Se300; Se350 and Se400.

	Cu (%)	**Zn (%)**	**Sn (%)**	**Se (%)**
Se200	42	21	24	13
Se255	39	26	19	16
Se300	35	25	17	23
Se350	32	18	12	38
Se400	31	14	9	45

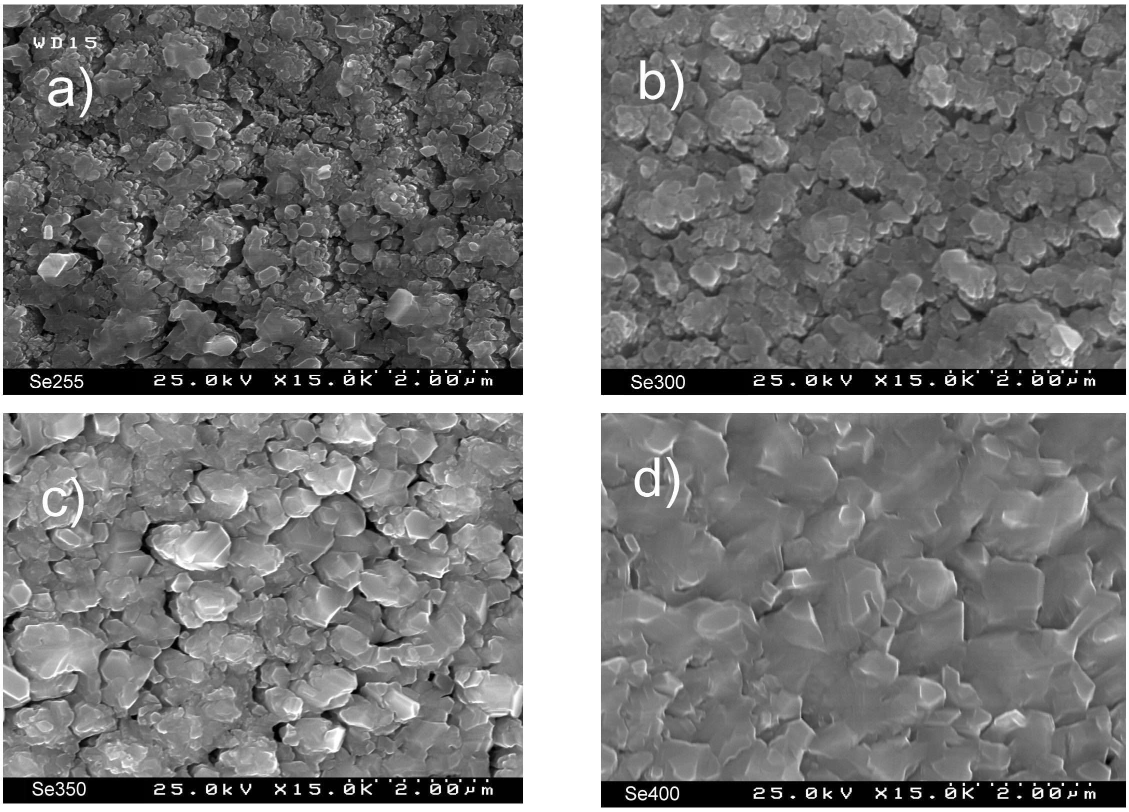

Figure 4-12: SEM surface micrograph of samples: a) Se255; b) Se300; c) Se350 and d) Se400.

Table 4-8: Ratios of the element concentrations and thicknesses for samples Se200; Se255; Se300; Se350 and Se400.

	[Cu]/([Zn] + [Sn])	**[Zn] / [Sn]**	**[Se]/[metal]**	**Thickness (µm)**
Se 200	0.9	0.9	0.15	0.9
Se 255	0.9	1.3	0.20	1.0
Se 300	0.8	1.5	0.30	1.0
Se 350	1.1	1.4	0.61	1.5
Se 400	1.5	2.2	0.82	1.6

In Figure 4-13, the XRD diffractograms of the samples are presented. For the samples grown at the lower temperature, traces of a Cu and Sn compound, $Cu_{6.26}Sn_5$, are found in the XRD analysis with peaks at 30.14° and at 42.89° [100], the same phase was present in the precursors. The amount of this compound tends to diminish with increasing selenization temperature. Moreover, the metallic single layers present in the precursors, Cu, Zn and Sn are not found in any of the films, meaning that even for low temperatures, diffusion of the atoms already occurs. For samples Se255, Se300 and Se350, the compound Cu_4Zn was detected in the XRD analysis with peaks at 37.69°, 41.93° and 43.27° [100]. According to the XRD data, Cu_2Se appears to be present in all samples with peaks at 26.90° and 44.69°. However, the intensity of those peaks is relatively small compared to the peaks of other compounds; this may indicate that there is only a small amount of Cu_2Se in the films. It is also quite clear from Figure 4-13 that the relative intensity of those peaks tends to decrease with increasing temperature. The formation of Cu-Sn and Cu-Zn compounds proves the theory that Kirkendall diffusion occurs under these circumstances as was also seen in the context of CZTS development. Since Cu is so mobile, placing it in other position rather than on top could lower the films' adhesion. In all the films, the XRD showed the Mo peaks. At the temperature of 400 °C there are two XRD peaks at 30.66° and at 32.11° that could not be identified.

Regarding the detection of CZTSe/ZnSe, the only visible difference in XRD is a double peak of CZTSe at 53.39°, planes (3 1 2), and 53.45° planes (1 1 6) while in cubic ZnSe there is only a peak at 53.56° which corresponds to the planes (3 1 1) [100]. Using this double peak difference, it is possible to identify CZTSe in samples Se350 and Se400. Having identified CZTSe one cannot say anything about the presence of ZnSe by looking only at the XRD data. Raman scattering analysis, however, shows the presence of ZnSe with a peak at 252 cm^{-1} and at 202 cm^{-1} for samples Se200, Se255 and Se300 [132], see Figure 4-14. For samples Se350 and Se400 no evidences of ZnSe were found. However, in both samples, the three peaks of CZTSe identified by Altosaar et al. were found: 173 cm^{-1}, 197 cm^{-1}, and 231 cm^{-1} [80]. With these two analyses, it is possible to say that samples Se350 and Se400 contain CZTSe and do not contain ZnSe. For samples Se200, Se255 and Se300 one can say that ZnSe is present, but cannot draw any conclusion about a residual presence of CZTSe because Raman detects a broad peak at 197 cm^{-1}. In the sample Se400, there are two XRD peaks that were not associated with any phase. It may be possible that these peaks are from elemental Se but since no phase did match both peaks, it is difficult to say from which phase they come from exactly.

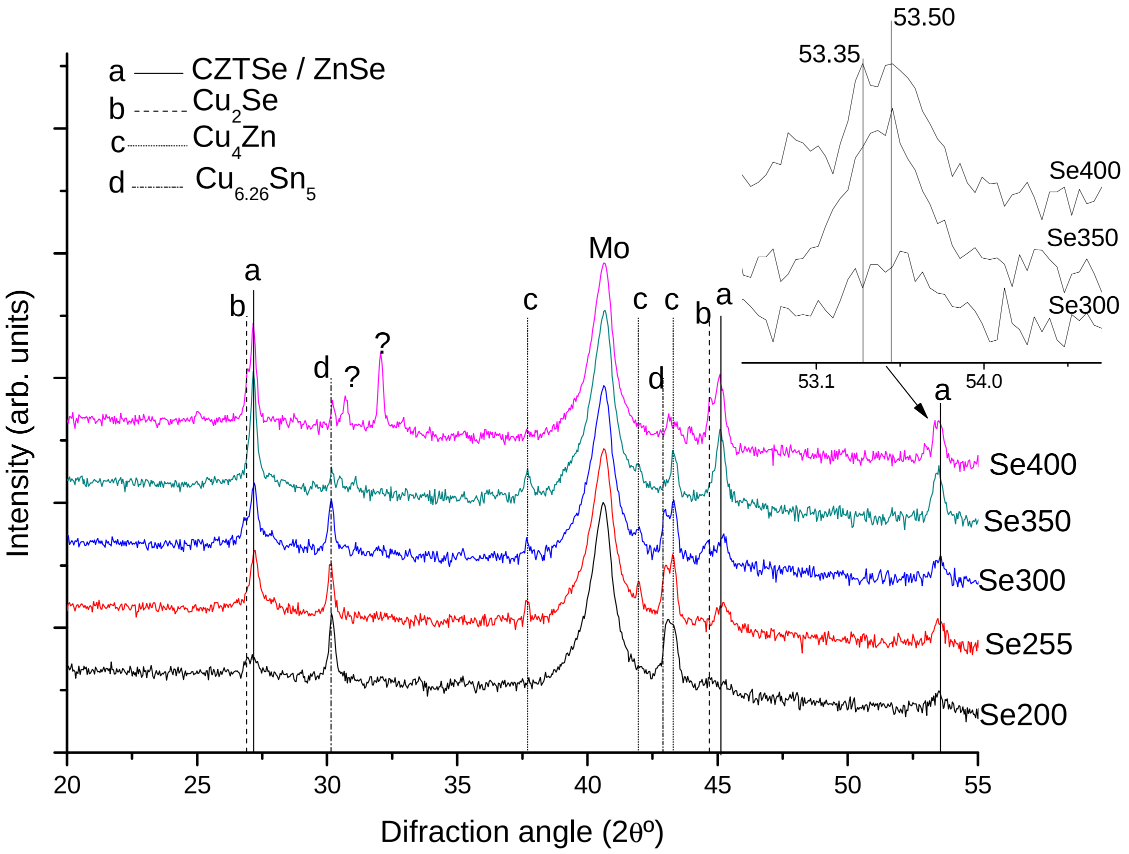

Figure 4-13: XRD diffractogram of samples Se200, Se255, Se300, Se350 and Se400. The inset at the top right corner shows the presence of the double peak of CZTSe observed in samples Se350 and Se400.

In Figure 4-14, it is also visible a small peak at 263 cm^{-1} assigned to Cu_2Se [105] in samples Se200, Se255 and Se300, confirming, thus, that even at low temperatures, some Se is reaching the Cu layer and forming Cu_2Se. Differences in the information obtained from XRD and the Raman scattering may be associated with different points and area of analysis.

In Table 4-8, it is presented the films' thicknesses. The increase of thickness with the temperature even with less material might be considered a paradox but can be attributed to the CZTSe formation with a corresponding expansion of the film. It is known that this material has a smaller density, 5.693 g/cm^3 [68], than the metallic precursors. The thickness values are the highest ones in the films that are believed to contain CZTSe, namely Se350 and Se400.

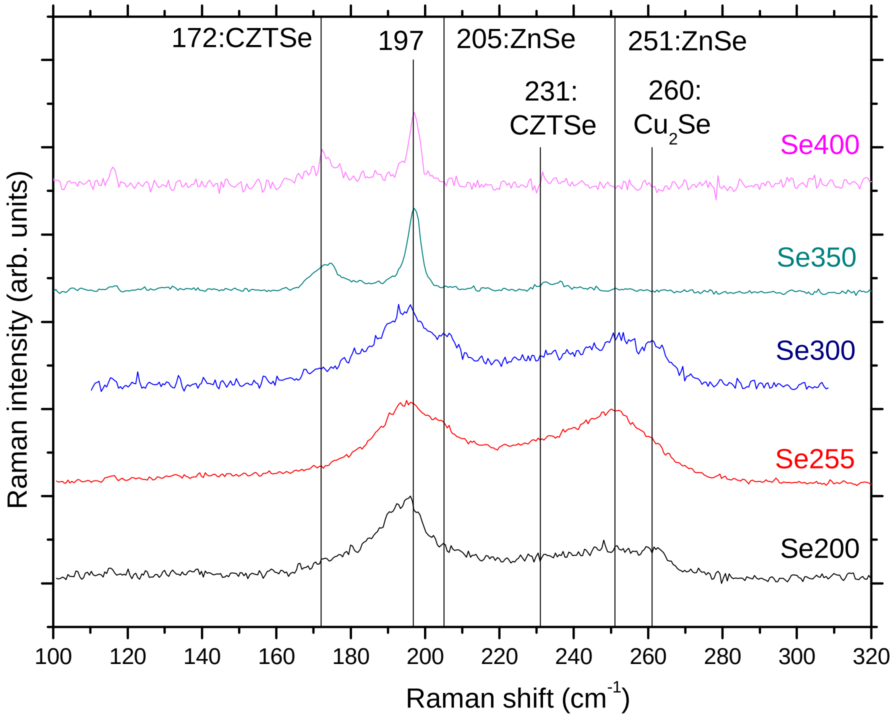

Figure 4-14: Raman scattering spectra of samples Se200; Se255; Se300; Se350 and Se400.

It is important to point out that when using this growth method, all films grown directly on soda lime glass (SLG) peeled off.

To conclude this study, it was shown that at temperatures as low as 350 ºC CZTSe is already formed. However at this working pressure there are losses of elemental Zn and SnSe by evaporation. Also, it seems that even at low temperatures there is the formation of binary compounds of Cu with Se, Sn and Zn. Zn seems to form compounds with Cu and with Se but not with Sn until the temperature reaches 350 °C and CZTSe is formed. The results show that the best temperature to prepare CZTSe films, in these conditions, is between 350 °C and 400 °C. After this initial test, it was important to see whether the conditions were reproducible and capable of growing single phase CZTSe thin films.

Knowing the quantity of Zn and Sn that is evaporated during the growth of CZTSe it is possible to deposit the precursors with enough extra material to compensate for the losses. An intermediate temperature of 375 ºC was chosen because the CZTSe presence was confirmed in Raman scattering spectra for 350 ºC. At this temperature the spectra had a low signal to noise ratio showing the best result of the series regarding the presence of CZTSe, whereas the XRD diffractogram was better for the one grown at 400 ºC, because the CZTSe double peaks at 53 º were more visible.

The final elemental composition desired is the one reported for the best cells by Katagiri et al. and Todorov et al. [81, 94] of [Cu]/([Zn]+[Sn]) ~ 0.8 – 0.9 and [Zn]/[Sn] ~ 1.1 – 1.3. Bearing in mind the losses for both temperatures, a precursor with [Cu]/([Zn]+[Sn]) = 0.5 and [Zn]/[Sn] = 1 was prepared. Both values were estimated considering that the Sn evaporation losses are greater for temperatures closer to 400 ºC due its vapour pressure and the previous results. The ratio [Zn]/[Sn] is expected to have a value higher than 1 because in the temperature test, the Sn losses were greater for all temperatures with the exception of the lowest one. This precursor was selenized with the same temperature profile described before, with a selenization temperature of 375 ºC and at 10^{-5} mbar.

The SEM surface micrograph of the CZTSe is shown in Figure 4-15. It shows an open structure with relatively big voids between crystallites. This situation has been addressed previously and is probably due to the layer of Sn prepared by DC sputtering that is quite rough. This morphology with voids is not consistent with the closed one seen in the last study. There were changes from the last study, mainly the composition and therefore this difference can be explained by the fact that in this case more losses could occur worsening the morphology. The SEM surface characterization of the precursors and the resulting CZTSe films points to a certain correlation between the two morphologies. There is a striking resemblance between Sn crystallites distribution in the precursors' surface, as shown in section 4.2.1.1.2, and the open structure of the CZTSe films.

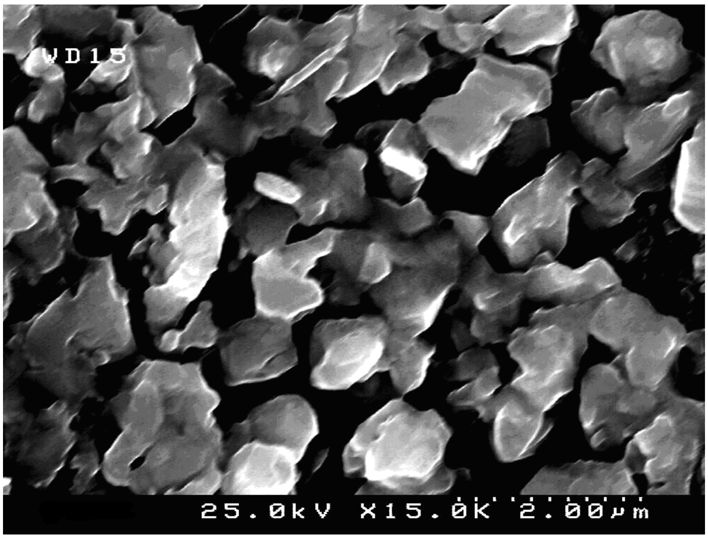

Figure 4-15: SEM micrograph of the surface of the CZTSe film prepared with Cu-poor precursors.

Table 4-9 shows the composition of the film before and after selenization. Before selenization the film shows the desired composition. After selenization the films were Cu rich with the ratio [Cu]/([Zn]+[Sn]) being higher than 1, Sn rich with the ratio [Zn]/[Sn] 0.9 and the selenization of the layers is incomplete given that [others]/[Se] is slightly higher than 1. It seems that under the same conditions the film lost more Zn than Sn seeing that prior to selenization [Zn]/[Sn] was 1.0 and afterwards 0.9. At the same time there were simultaneous losses of Zn and Sn as demonstrated by the fact that the ratio [Cu]/([Zn]+[Sn]) started with a value of 0.5 and went up to 1.1. It is likely that the evaporation losses are not the same from sample to sample inspite of having the same composition. This is because of the different thicknesses the precursors have which results from the lack of reproducibility of the Zn deposition. Since the thicknesses of the films are different detailed studies would be needed to understand how the composition and the thickness of the precursors influence the loss mechanisms of Zn and Sn. This issue is out of the scope of this work and therefore no further growth studies were conducted.

Table 4-9: Elemental composition of the Cu-poor precursors and its resulting selenized films.

Elemental compositional ratios	Before Selenization (ICP – MS)	After Selenization (EDS)
[Cu]/([Zn]+[Sn])	0.5	1.1
[Cu]/[Zn]	1.1	2.4
[Cu]/[Sn]	1.1	2.2
[Zn]/[Sn]	1.0	0.9
[Others]/[Se]	-	1.1

The film was analyzed using GI-XRD with the following incidence angles: 0.3 º, 0.5 º, 0.7 º,1º and 2 º. The results are shown in Figure 4-16. On one hand, with the increase in the incident angle the presence of the Mo peaks are more evident, as expected, meaning that the analysis is being done deeper in the sample. On the other hand for the lower angles, 0.3 º and 0.5 º, the Mo peaks are not visible which means that the analysis is being done closer to the surface. CuSe can be identified at 2 º, 1 º and 0.7 º, even though the peaks are weak and close to the CZTSe main peak, the peaks at 30.36 º and 31.00 º are very distinct. For the incidence angles of 0.3 º and 0.5 º the peaks of CuSe are barely identifiable, which could mean that the phase is not present near the surface, however since the signal to noise ratio is low a definitive conclusion is not possible. There is no evidence of other phases other than CZTSe and CuSe. No evidence of any metallic layers is seen, therefore it can be concluded that the selenization of the precursors was complete.

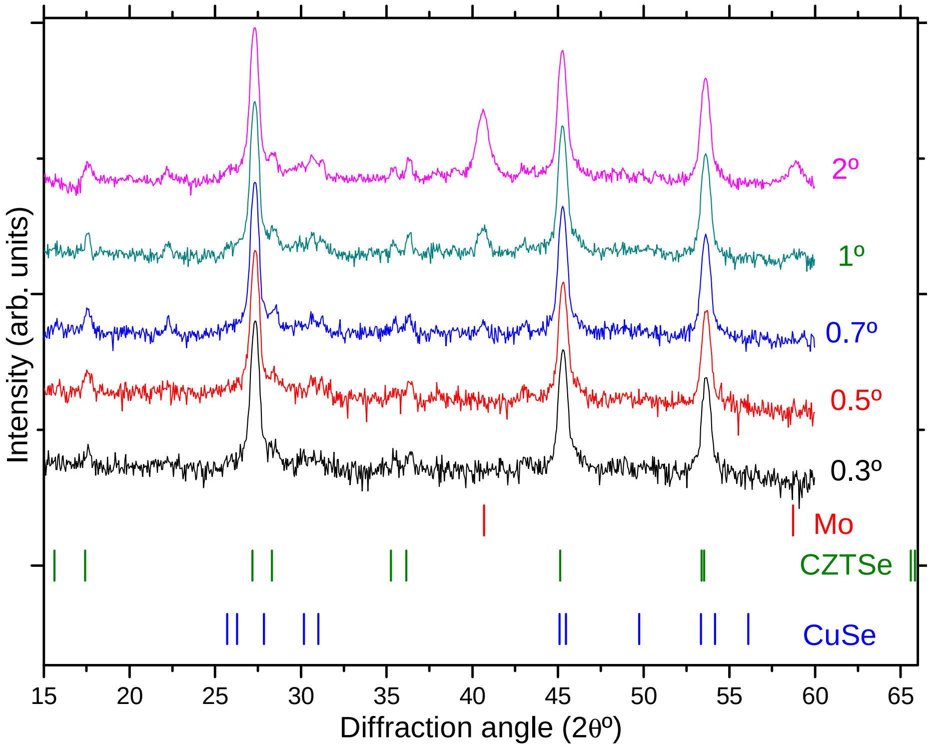

Figure 4-16: Grazing-Incidence XRD diffraction patterns for the CZTSe film.

The XRD pattern of the resulting film using normal incidence is presented in Figure 4-17. A much better signal to noise ratio is obtained and a finer analysis is possible. The CZTSe presence is confirmed by several peaks. The strong peak at 27.14 º corresponds to the plane (1 1 2). This peak is quite stronger than the Mo one and has a full width at half maximum of 0.14º which indicates that the sample has a good cristallinity. Planes (2 2 0)/(2 0 4) and (3 1 2)/(1 1 6) are also quite strong. Other planes are present: (1 0 1), (4 0 0), (4 2 4)/(2 2 8). Traces of CuSe were present with a very small shoulder in the peak (2 2 0)/(2 0 4) of CZTSe at 45.91º, plane (1 1 0) for CuSe, and two small peaks at 30.36º and 31.00º, planes (1 0 3) and (0 0 6), respectively. Regarding the detection of Cu_2SnSe_3 and ZnSe in the top inset there is what seems to be a structure of three peaks. Those peaks may be the CZTSe peaks at 53.39º (3 1 2), 53.53º (1 1 6), or Cu_2SnSe_3 at 53.41º (3 1 1) or even ZnSe at 53.57º (3 1 5). In the region between 83.0 º and 83.6 º it is even more complicated to analyze the differences. A detailed look at this region, shown in the bottom inset, shows the presence of three peaks at 83.12 º, 83.32 º and 83.45 º. The first two peaks, 83.13 º and

83.32 ° can be attributed to the CZTSe's (4 2 2)/(4 2 4) planes and CZTSe (4 0 6) plane, while the peak at 83.45° could be from ZnSe (4 2 2). But these differences are hard to evaluate due to the small number of points of the measurement and because there may be some small shifts of the peaks due to stress.

The lattice constants *a* and *c* of the tetragonal unit cell were estimated and the values found were 5.683 Å and 11.342 Å, respectively. These are in accordance with published data [100] and *c/2a* takes the value of 0.998. This value is close to 1 which means that the cell maintains its tetragonality and is not distorted. The crystallite sizes were estimated using Scherrer's equation and a value of 211.7 nm was obtained. Analysing the SEM surface image it can be seen that the grains observed appear to be larger than the value obtained with Scherrer's equation. However one must keep in mind that the estimated value is an average of the crystallite size and what is visible may be agglomerates of crystallites and not single crystals. The width of the diffraction peaks may also be influenced by stress states which could make this approach invalid. To resolve this, Ritveld or Le bail refinements would be necessary.

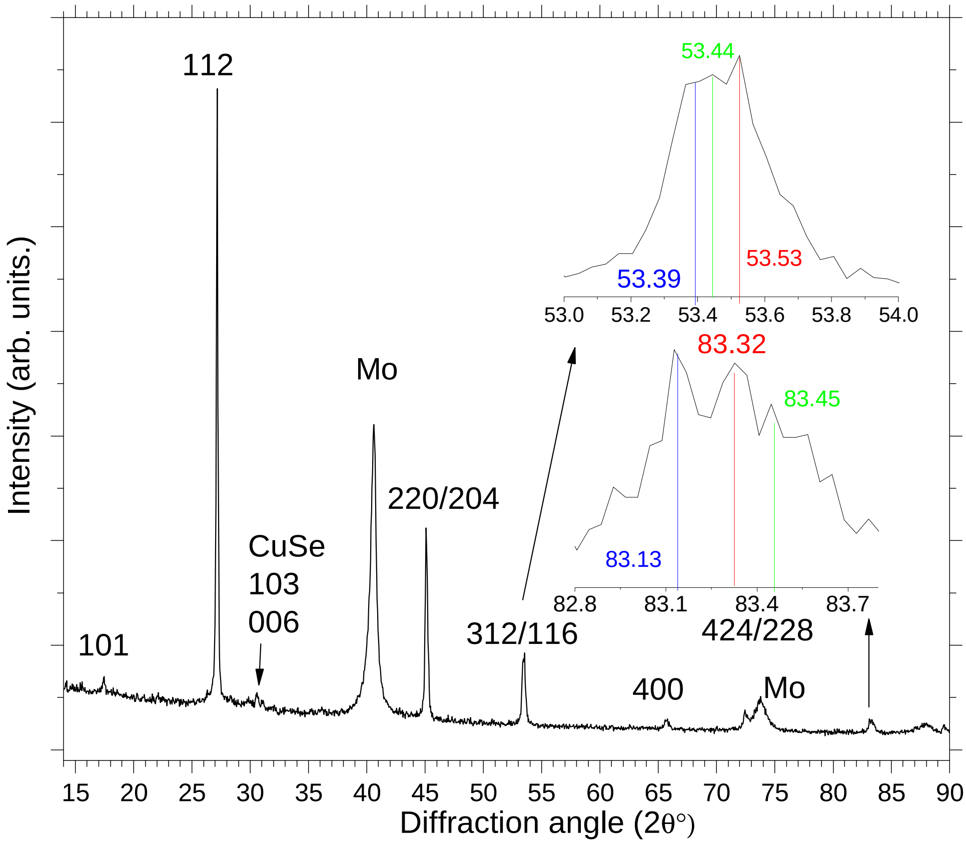

Figure 4-17: XRD diffractogram with the identification of CZTSe phase. The insets are zooms of the double peaks of CZTSe. The colours are only guides to the eye.

Raman scattering analysis confirmed the presence of CZTSe with peaks at 174 cm^{-1}, 195 cm^{-1} and 232 cm^{-1}, see Figure 4-18. Some regions of the sample also presented small traces of $Cu_{2-x}Se$ phases as had already been hinted by the XRD data. This film revealed a value of [Zn]/[Sn] slightly smaller than one, which means that there is an excess of Sn, but even in these circumstances no significant traces of CTSe were found. The strongest peak of CTSe should be seen in the region of 180 cm^{-1}, but with the broadening of the CZTSe peaks at 195 and 172 cm^{-1} it is unclear whether the CTSe peak is hidden or is not there at all. XRD suggested that ZnSe could be present, but Raman scattering discarded that possibility.

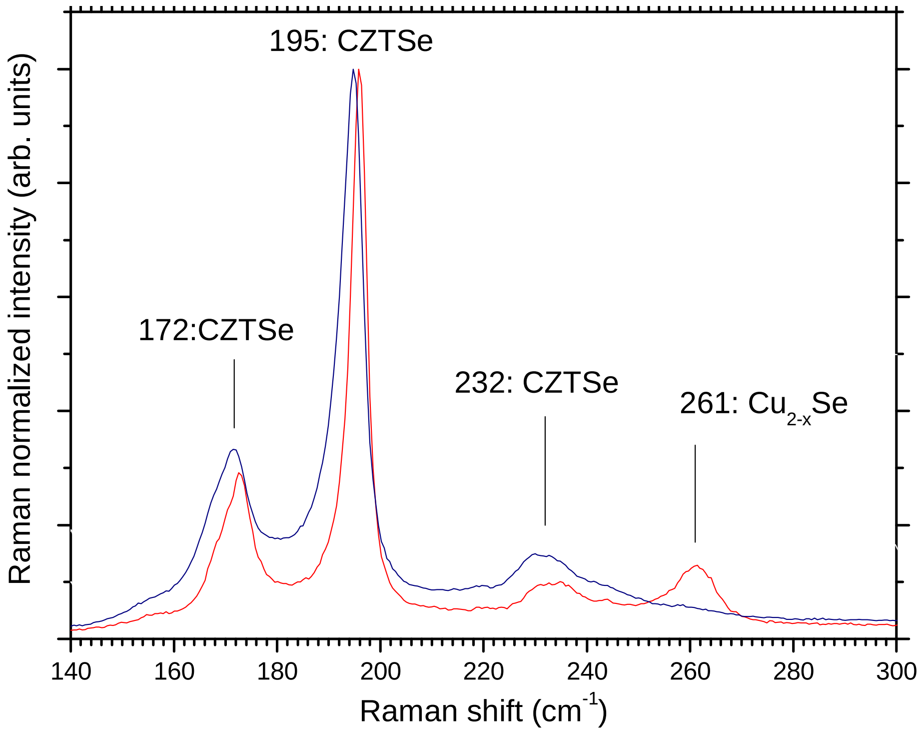

Figure 4-18: Raman scattering analyses for two different points of the same sample.

The growth of CZTSe on SLG glass was tested, but the adhesion of the samples was very poor. Some films peeled-off during the growth, while others presented a visibly non-uniform surface. Samples on Mo showed a better adhesion and uniformity. Since the growth of samples on SLG proved not to be possible using this method, only samples on Mo were available. This is a problem if one wants to estimate the band gap energy from the absorption coefficient since this is normally calculated from transmittance and reflectance measurements. From films grown on Mo it is not possible to measure transmittance therefore only reflectance is available.

The diffuse reflectance measurements were used to estimate the absorbance, the result can be seen in Figure 4-19. Since the slope of the curve is not sharp, the band gap energy estimation is difficult. Different slopes can be fitted and values ranging from 1.13 eV (1130 nm) to 1.42 eV (900 nm) can be obtained. Hence this method proves not to be accurate enough to be used.

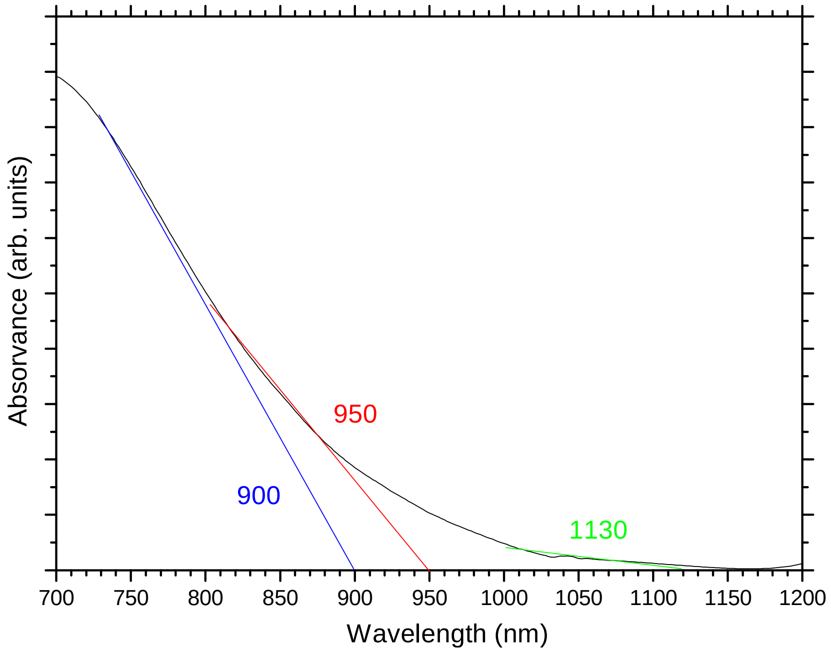

Figure 4-19: Absorvance calculated from the diffuse reflectance.

The results demonstrate that it is possible to achieve CZTSe films with composition close to stoichiometry and the kesterite/stannite structure starting with DC magnetron sputtered Cu-poor stacked elemental precursors. This is a positive result given that this approach is suitable for large scale deposition but it is based in losses of material which are not desired in real life applications. In the next section, the study of the influence of the pressure in the selenization of the precursors is done.

4.2.1.3 Pressure influence on the selenization of precursors

To study the influence of the pressure on the properties of the CZTSe films [V,VI], the precursors were prepared with the following order SLG/Mo/Zn/Sn/Cu. The thicknesses of the layers were: Zn – 380 nm, Sn – 460 nm and Cu – 280 nm. According to the estimations needed for the thickness of the precursors, this should give Cu-rich and Sn-rich films. This set of precursors was selenized at 375 ºC with the temperature of the Se evaporator at 255 ºC and at different pressures.

In Table 4-10 the values of the EDS measurements are presented. In the case of the Sn losses, the ratio of [Cu]/[Sn] varies between 3.4 and 5.3 with no apparent correlation with pressure. This points out to losses of Sn for all the studied pressures. For Zn [Cu]/[Zn] decreases with increasing pressure which indicates that the Zn losses are reduced. For [Cu]/([Zn]+[Sn]) the same pattern is observed and this is mainly due to the Zn losses. At 10^{-4} mbar, all the ratios exhibit a singular behaviour since they do not follow the trends in the other pressures and there are more Zn losses and less Sn losses. This fact is not understood. The selenization of the layers is reduced with the increase of the pressure, this is seen by the increase of the ratio [others]/[Se]. This fact shows that if pressure is increased any further to prevent the losses of Sn, the selenization will be harder. Therefore, at high pressures this temperature is too low to allow the diffusion of Se.

Table 4-10: Elemental composition of films selenized at different pressures at 375 ºC.

Pressure (mbar)	[Cu]/([Zn]+[Sn])	[Cu]/[Zn]	[Cu]/[Sn]	[Zn]/[Sn]	[Others]/[Se]
10^{-5}	2.3	4.2	5.3	1.3	1.1
10^{-4}	2.0	5.0	3.4	0.7	1.3
10^{-3}	1.7	2.5	4.8	2.0	1.6
10^{-2}	1.6	2.4	4.6	1.9	1.7

These conclusions suggest that in the pressure range from 10^{-2} mbar to 10^{-5} mbar, heavy losses of Sn occur and there is a deficiency in the selenization.

A new set of samples was selenized in the pressure range from 10^{-5} mbar to 1 mbar. The samples selenized at pressures lower than 1 mbar had a substrate temperature of 500 ºC, while at 1 mbar were selenized at a substrate temperature of 520 ºC. This time, Se was evaporated at 345 ºC. During the cooling down phase, the Se source was turned off only when the substrate temperature reached 270 ºC. This was done to prevent Se losses by re-evaporation from the film.

For this test, the precursors were selected not according to thickness, but according to the composition measured by ICP-MS for a greater control. Five similar precursors were selected and the elemental ratios were the following: [Zn]/[Sn]=1.1 and [Cu]/([Zn]+[Sn])=0.9. There were some changes in the thickness from film to film but these were small. The resulting films' composition was measured using EDS and the results are shown in Table 4-11. For the first four samples, selenized at low pressures, it is clear that there are significant losses of Sn and Zn. Assuming that there are no losses of Cu in the film, one can compare these losses by looking at the ratios of [Cu]/[Zn] and [Cu]/[Sn]. The value of [Cu]/[Zn] seems to be approximately constant for the three lowest pressures, changing only from 4.4 to 4.7. However, at 10^{-2} mbar that value lowers which indicates that the rise in pressure is preventing evaporation of Zn. At 10^{-1} mbar, this ratio is lower than 2, which indicates no losses of this material. For the Sn losses, in the four lowest pressures the value of [Cu]/[Sn] varies with no apparent relation with pressure as seen in the previous study. This is probably due to measurement uncertainties since in those cases the amount of Sn was so little that EDS may not have had enough resolution. However at 10^{-1} mbar, [Cu]/[Sn] takes a value close to 2 which means that the loss of Sn by evaporation of SnSe was drastically reduced. With little losses of Sn and Zn at 10^{-1} mbar, it is clear why the [Cu]/([Zn]+[Sn]) value is 1. Despite the improvement in controlling the losses of Sn and Zn, the value [others]/[Se], is still 1.4 which indicates that the film is not fully selenized since this value should be close to 1. To overcome this problem the substrate temperature was increased from 500 ºC to 520 ºC what would allow more Se to diffuse to the film. To prevent an increase in the losses due to the temperature rise, the pressure was also increased to 1 mbar.

The film grown at 1 mbar and 520 ºC had an elemental composition very close to stoichiometry as shown in Table 4-11: [Cu]/([Zn]+[Sn])=0.9, others/[Se]=1 and [Zn]/[Sn]=0.9. After this film, several other were grown using the same conditions. Those were the best CZTSe films grown during this work, and its properties are analysed in section 4.2.3.

Table 4-11: Elemental composition ratios of the CZTSe films grown at different pressures, from 10^{-5} mbar to 1 mbar.

Pressure (mbar)	Substrate temperature (ºC)	[Cu]/([Zn]+[Sn])	[Cu]/[Zn]	[Cu]/[Sn]	[Zn]/[Sn]	[Others]/[Se]
10^{-5}	500	3.5	4.4	17.5	3.9	1.5
10^{-4}	500	2.9	4.7	7.7	1.6	1.4
10^{-3}	500	3.3	4.4	13.7	3.1	1.4
10^{-2}	500	2.7	3	21.2	6.9	1.6
10^{-1}	500	1.0	1.8	2.1	1.2	1.4
1	520	0.9	1.9	1.7	0.9	1

4.2.2 Growth of CZTSe using the hybrid method

In the temperature test, section 4.2.1.2, the minimal temperature at which CZTSe was formed was established and so the hybrid method studies are taking this information into consideration.

In the hybrid method, as described previously, there is a combination of sputtering and evaporation. The sputtered materials were Cu and Sn while Zn and Se were evaporated. Zn and Se were chosen to be evaporated because of their high vapour pressures at relatively low temperatures. It is usually argued that using sputtering instead of evaporation leads to lower energy consumptions in the growth process when compared with the sole use of evaporation for all elements [133]. In this method, where Se is evaporated in excess, it is assumed that only the needed Se is captured and the excess is re-evaporated. This is something that occurs both in CIGS [134] and CZTS [128].

As mentioned before, one of the advantages of using the hybrid method when growing CIGS, was the ability to control in real time the final composition of the films. Due to the change in the films emissivity, when passing from Cu-rich to Cu-poor films during the growth, there is a change in the amount of heat that is needed to maintain the sample at a certain temperature. By monitoring the variation in the temperature of the sample or the power needed to sustain the same temperature, it is then possible to predict the Cu-state of the film. This change of emissivity is usually assigned to the change of electrical conductivity of CIGS films from n-type to p-type which occurs when Cu vacancies are introduced [43]. This method is usually called the end point detection, EPD. In the case of CZTSe there are no evidences of this transition in the literature and since the

EPD is quite useful, it is important to verify its presence or not. Since there may be other phases creating this signal before growing the CZTSe it is important to grow Cu-Sn-Se phases to see if there is any EPD.

4.2.2.1 Preparation of Cu-Sn-Se compounds using the hybrid method

For the hybrid growth of ternary phases, a 3-step growth process was established. A phase likely to be present is Cu_2SnSe_3 (CTSe). Table 4-12 shows the substrate temperature, temperature of the Se evaporator, the duration, and what material was being sputtered for each step. Step 1 consisted of deposition of a thin layer of Sn, the purpose of this layer was to prevent the selenization of the Mo. Then, in step 2, the Se evaporator was ramped up to 255 ºC during 15 minutes and at the same time Cu was sputtered. This step lasted 30 minutes. Finally Sn was sputtered again with the duration of 40 minutes. The working pressure was 4.2 x 10^{-3} mbar. Several tests were done with different durations for the final step and in none of them an end point signal was detected.

Table 4-12: Description of the 3-step growth of CTSe.

Step	Temperature of the Se evaporator (º C)	Substrate temperature (º C)	RF magnetron sputtered material	Time (min.)
1	100	200	Sn	5
2	ramp to 255 (15min)	350	Cu	30
3	255	350	Sn	40

The absence of an EPD signal meant that the reproducibility of CTSe growth process was low since no detection of the stoichiometry point is achieved. From this point on, the depositions were controlled using time. There were many variations in the composition of the different samples grown. This was partly due to the variations in the sputtering rates of Cu and Sn that were identified and mainly due to the likely Sn losses during the last stage. The variation of the rates was due to the impedance matching capacitance differences there were in the RF source from deposition to deposition since this was done manually.

The best CTSe samples were analysed in terms of composition, morphology, structure and some electrical measurements. Figure 4-20 shows a SEM micrograph of the surface of a CTSe film, it shows grains with sizes around 200 nm and some voids. The composition of this film was measured using EDS and the elemental ratios were [Cu]/[Sn] = 2.5 and [others]/[Se] = 1.0.

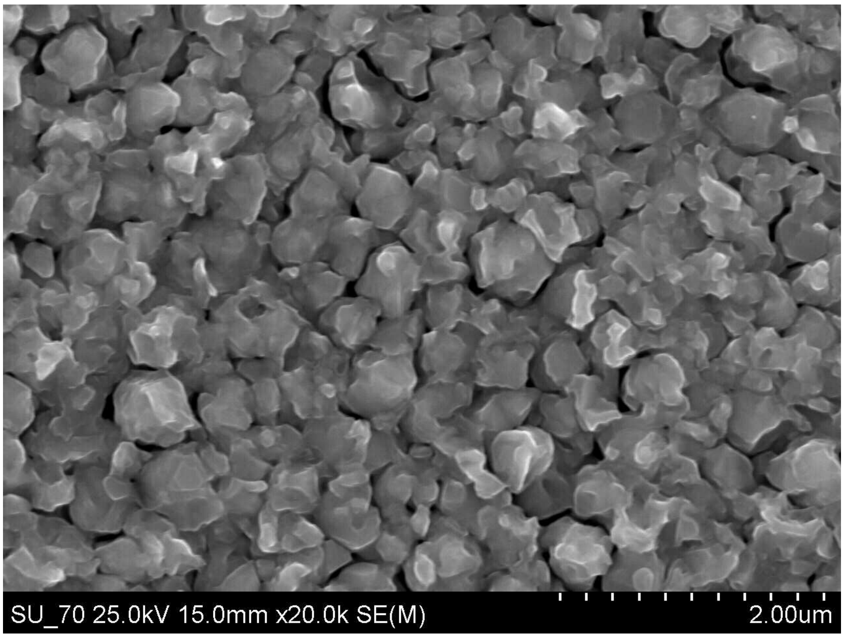

Figure 4-20: SEM surface micrograph of the best CTSe film prepared using the hybrid method.

In Figure 4-21, the XRD diffractogram of one of the CTSe samples is shown. The figure illustrates three different phases present. Cubic CTSe has been identified with the following planes, (1 1 1) at 27.15 º, (2 2 0) at 45.07 º, (3 1 1) at 53.41º, (4 0 0) at 65.64º (4 2 2), (3 3 1) at 72.41º, and (1 1 3) at 83.19 º; cubic Cu_2Se was found with a strong peak at 44.61 º which corresponds to planes (2 2 0) and there is a shoulder at the peak (1 1 1) of CTSe at 26.88º that corresponds to planes (1 1 1) of Cu_2Se. The Mo reflections are seen as well. Since these phases are hard to distinguish in XRD, Raman scattering was performed and it confirmed the presence of CTSe because a broad peak centred at 180 cm^{-1} is present, see Figure 4-22. The Raman scattering peaks belonging to CTSe, 180 cm^{-1} and 236 cm^{-1} were also seen by other groups [80]. For the selected point Raman analysis did not show the presence of $Cu_{2-x}Se$, which means that there are regions of the sample where $Cu_{2-x}Se$ is not present. There were other locations where $Cu_{2-x}Se$ phases were identified. If single phased films would be required for further studies, those could be prepared by a KCN etching to remove the $Cu_{2-x}Se$ phases [119]. The presence of these phases is explained by the excess of Cu in the films, which was seen by the ratio of [Cu]/[Sn] = 2.5 which is greater than 2, the expected value for single phase films of Cu_2SnSe_3.

Regarding electrical properties, the type of conductivity was determined using hot point probe and the measured samples were p-type.

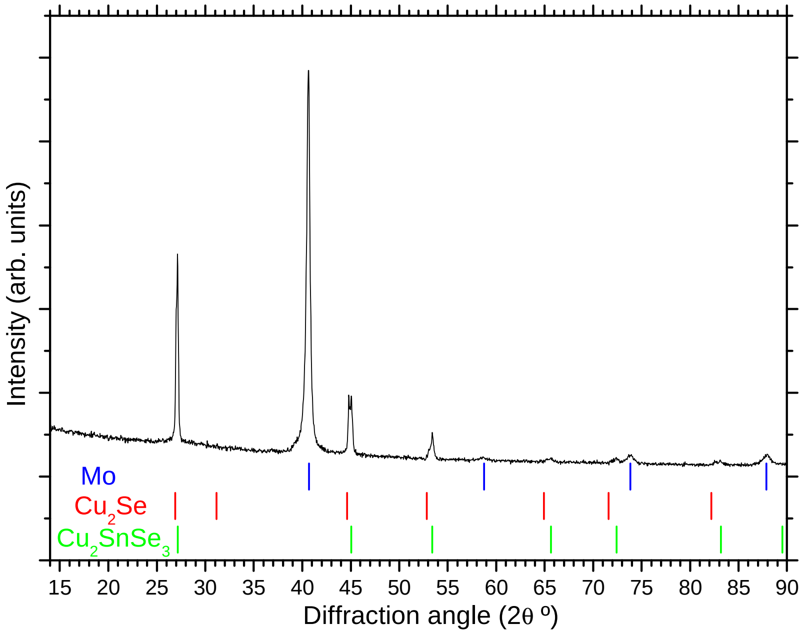

Figure 4-21: XRD diffractogram of a CTSe sample grown with the hybrid system, over Mo. The presence of Mo, cubic CTSe and cubic Cu_2Se is confirmed.

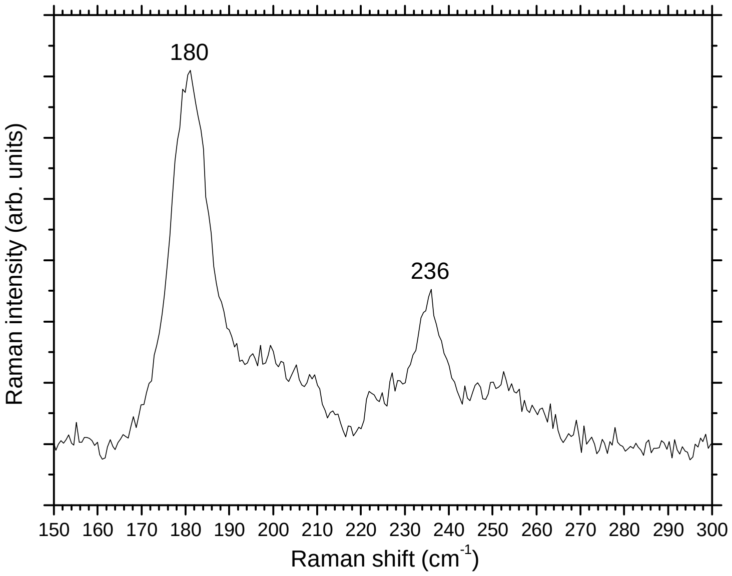

Figure 4-22: Raman scattering spectra of a CTSe sample. This analysis confirms the presence of CTSe with peaks at 180 cm^{-1} and 236 cm^{-1}.

4.2.2.2 CZTSe growth using the hybrid system

For the growth of CZTSe, the same 3-step approach as for the CTSe was followed. The temperature study presented in section 4.2.1.2 showed that the growth of single phase CZTSe films was only possible for substrate temperatures higher than 350 ºC. In this range of pressure and temperature, it is likely that some losses of Sn occur. In the last step, Sn was sputtered and Zn was evaporated.

The detailed steps are presented in Table 4-13 and an example of the power monitoring graph is shown in Figure 4-23. The basic idea was to make a Cu-rich to Cu-poor transition identical to the one observed in CIGS. The first step, *a*, was the deposition of a thin Sn layer. This was done in order to prevent a direct selenization of the Mo layer. The next step was the deposition of a layer of Cu and its selenization, step *b* to *e*. It is worth noticing that the Se evaporator is ramped up at the beginning of this step, which means that the Se evaporator only reaches the maximum temperature after 15 minutes while the whole step lasts 30 minutes. At point *d* there is a transition which is possibly the point where this layer is selenized. Point *c* there was a power correction made by the proportional–integral–derivative (PID) controller, also called a power overshoot. The last step is the formation of a Cu-poor film by sputtering Sn and evaporating Zn and Se, from *f* to *g*. Se is evaporated in excess as mentioned before, while the deposition rates of Sn and Zn were to be identical. No variation in the power signal was detected and therefore, no EPD signal was observed. Several samples with different times for step 3 were grown and the EPD signal was never seen. This probably means that in CZTSe, the Cu-rich to Cu-poor transition does not originate any significant change in the emissivity of the film and therefore an EPD signal is not visible. This brought significant difficulties to the growth of CZTSe films in a reproducible way since there was a variation in the deposition rates of the different materials and there was no means of detecting the stoichiometric point.

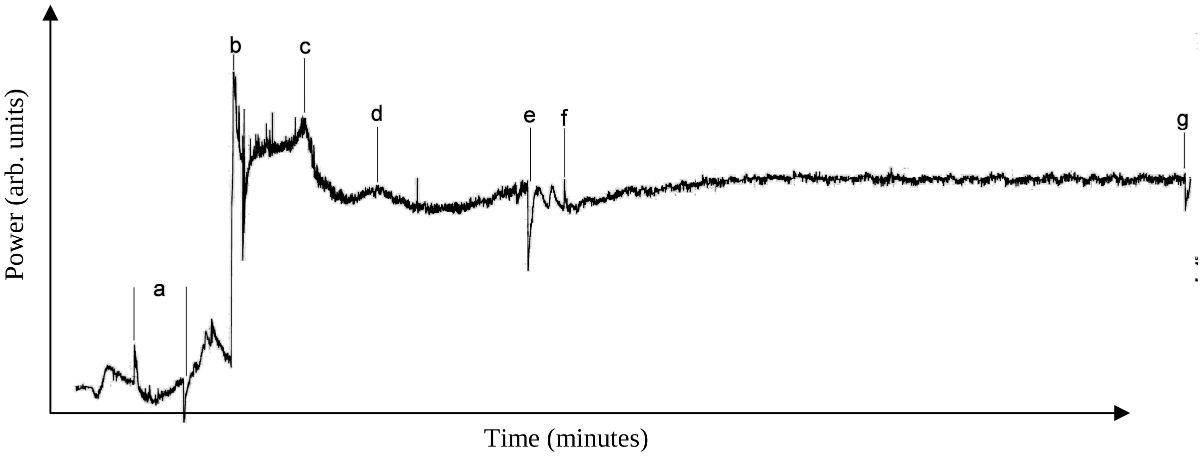

Figure 4-23: Time evolution of the power applied to the substrate's heater during the growth of the CZTSe thin films.

Table 4-13: Description of the 3-step growth of CZTSe. The step letters correspond to the points in Figure 4-23.

Step	**Duration (min)**	**Temperature of the Se evaporator (º C)**	**Substrate temperature (º C)**	**Material being sputtered (target)**	**Temperature of Zn evaporator (º C)**
a	5	100	200	Sn	100
b-e	30	ramp to 255 (15min)	350	Cu	100
f-g	45	255	350	Sn	Ramp up to 300

Given that there was no way to know when to stop step 3 several deposition times were tested, the composition of those films is presented in Table 4-14 . With the increase of the duration of this step, two trends in the variation of the composition were noticed. Those can be observed in Figure 4-24. One is the increase of the ratio [others]/[Se], it starts around 1.2 and increases up to 2.8. Values close to 1 mean that the samples are fully selenized. For all samples there is a deficiency of Se and this gets worse with the increase of duration of the last step. It is likely that at this temperature the Se atoms do not have enough energy to diffuse into the sample and selenize only a certain thickness near the surface. Since the overall thickness of the sample was increased and only a certain layer is selenized, the relative amount of Se diminishes explaining the evolution of this value. This question will be addressed later. Another trend that can be seen is the decrease of the value

[Cu]/([Zn]+[Sn]). This is expectable, considering that the quantity of Cu is kept constant with a fixed deposition time in step 2. At the same time, no losses of Cu are predicted, and as the last step consists of depositing Zn and Sn it consequently makes the relative quantity of Cu to diminish.

Regarding the quantity of Sn and Zn in the film some odd variations are noticeable. By looking at the value [Cu]/[Zn], which should be close to 2, it was noticed that with the increase of the duration of step 3 and with the exception of the second sample, this value tends to decrease from 2.2 to 1. The increase for the second sample from 2.2 to 2.4 is minimal. In addition with the increase of the duration of step 3, the deposition rates of Zn are somewhat stable and predictable. The first two films have a value of [Cu]/[Zn] close to 2 so if one was looking only at this value, this would be an acceptable duration. However one must have in mind Sn and Se as well. Concerning the quantity of Sn in the films, this gets fairly more complicated. The first film shows a very high value of [Cu]/[Sn] meaning that there is little Sn present, this is also confirmed by the value [Zn]/[Sn] which is 2.9 and should be close to 1. For the second sample [Cu]/[Sn] is close to 2 as wanted and since the quantity of Zn was also close to what was desired, this gave a value of [Zn]/[Sn] of 0.8. With regards to the third film, the trend of the [Cu]/[Sn] ratio deviates and instead of observing a decrease of this value, an increase is seen to 2.4. For the last film the value [Cu]/[Sn] goes down again to 1.4. This variation is large and it is probably due to evaporation of SnSe. This variation could also come from some eventual non-uniformity present in the samples. While no Zn losses were detected, it is possible that these elements, Zn and Sn, form compounds with Se as soon as Se arrives at the surface of the sample. If SnSe compounds are formed, evaporation of these compounds is expected since the working pressure was 4.8×10^{-3} mbar and the substrate temperature 375 ºC.

Table 4-14: Elemental composition variations for four samples grown using the hybrid system with different durations for step 3.

#	Sample name	[Cu]/ ([Zn]+[Sn])	[Zn]/[Sn]	[Cu]/[Zn]	[Cu]/[Sn]	[others]/[Se]	Duration of step 3 (minutes)
1	2008_07_04	1.7	2.8	2.2	6.7	1.2	24
2	2008_06_16	1.1	0.8	2.4	1.9	1.5	45
3	2008_08_19	0.9	1.7	1.4	2.4	2.2	55
4	2008_08_04	0.6	1.4	1	1.4	2.8	62

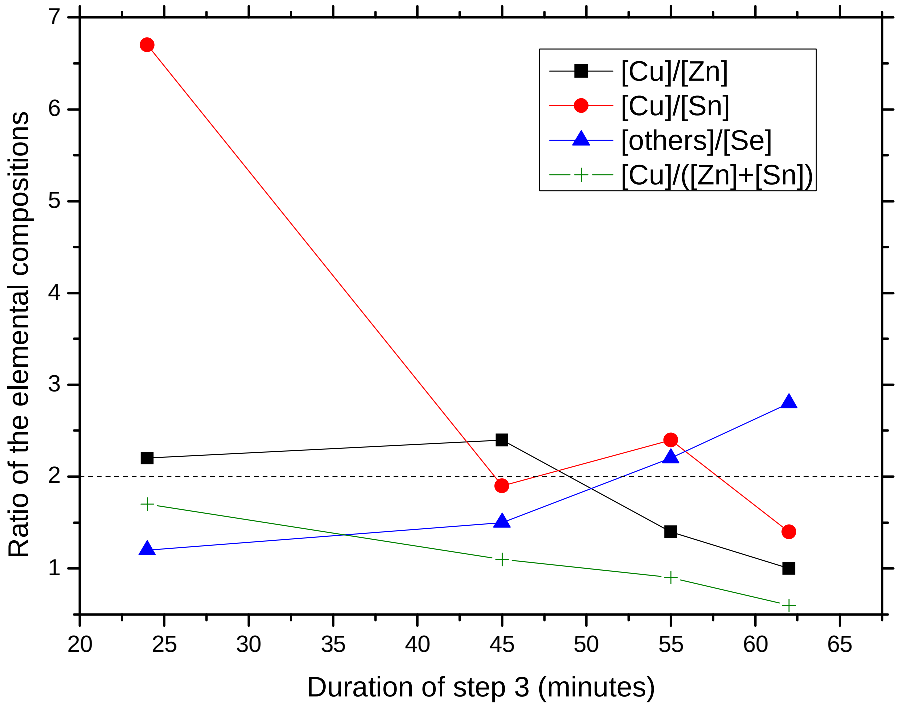

Figure 4-24: The evolution, with the duration of step 3, of the elemental ratios [Cu]/[Zn], [Cu]/[Sn] and [others]/[Se] for samples grown using the hybrid system.

Film number 2, with a duration of 45 minutes for step 3, was further studied because the composition appeared to be interesting: [Cu]/([Zn]+[Sn])=1.1; [Zn]/[Sn]=0.8 and [others]/[Se]=1.5. These values show that in terms of Cu, the film is near the stoichiometric point but it is Zn-poor and the ratio [others]/[Se] is greater than 1 show that the film is not fully selenized as discussed before. The SEM surface micrograph is shown in Figure 4-25 and illustrates an open structure with what appears to be round grains with a size of about 300 nm. Raman scattering analysis, Figure 4-26, shows the presence of CZTSe with peaks at 172 cm^{-1} and 194 cm^{-1} and CTSe with a peak at 180 cm^{-1}. The sample was not uniform since for different regions, different results were obtained. The XRD analysis, Figure 4-27, demonstrated that several phases were present, namely: Mo, Cu_3Sn, CZTSe/CTSe/ZnSe, Sn, and SnSe. This large number of phases present was not expected when looking at the Raman scattering analysis. The difference is probably due to the different area of analysis of the two techniques. Raman is a laterally micro sensitive with an effective depth analysis that should be no larger than 100 nm for the used wavelength, which was 488 nm. The fact that the film was not fully selenized is confirmed by the XRD analysis with the presence of Sn and Cu_3Sn. XRD cannot resolve between

CZTSe, CTSe and ZnSe but Raman indicates that CZTSe is present and saw no traces of ZnSe. The sample temperature is not high enough to allow the diffusion of Se into the film, as it can be observed by the metallic alloys present. Although there are a few phases present, the CZTSe diffraction peaks are stronger than any other peaks. This is seen in Figure 4-27.

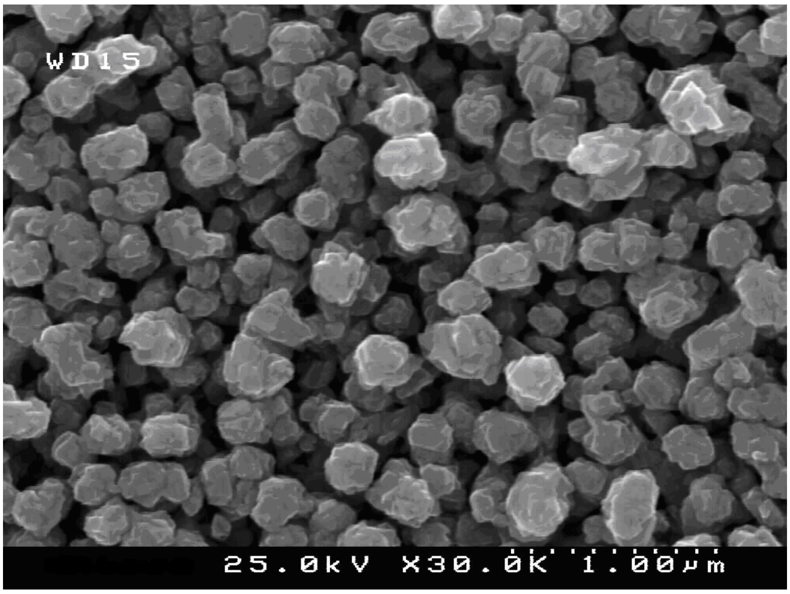

Figure 4-25: SEM surface micrograph of the best CZTSe film prepared using the hybrid system.

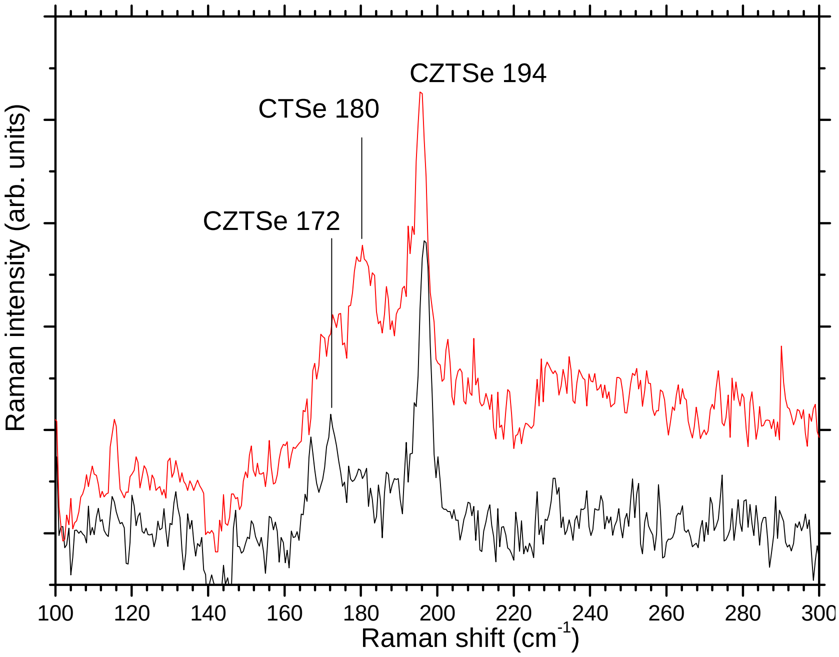

Figure 4-26: Raman scattering analyses for two different points of the same sample. Measurement done using a 488 nm Ar Ion laser as the excitation source.

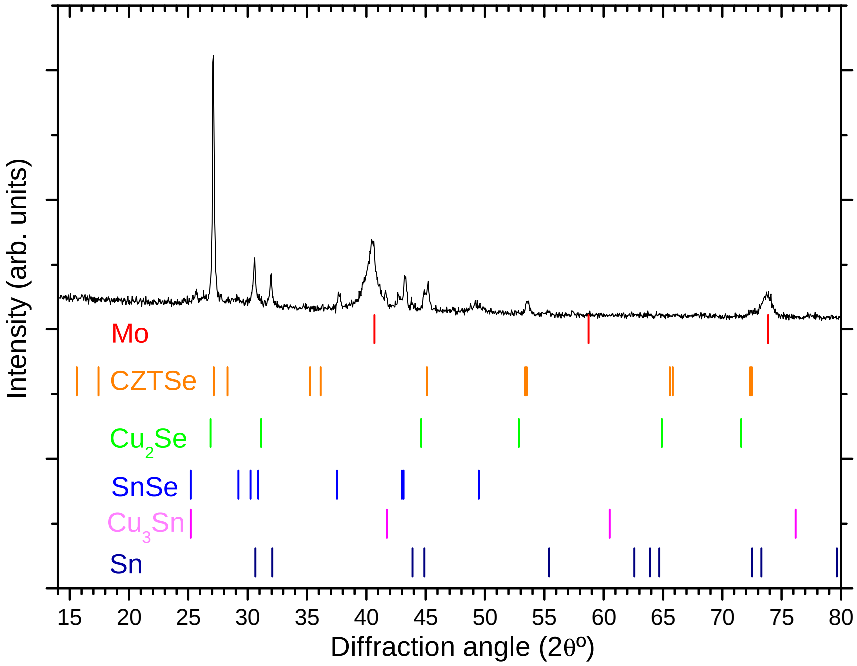

Figure 4-27: XRD diffractogram of a CZTSe film grown by the hybrid method.

The objective of this study was twofold, first to assess if there was an EPD signal during the growth of CZTSe and the second was to verify if this method was suitable to grow CZTSe. Raman scattering analysis confirmed that the film have parts where CZTSe is dominant and in some cases even the only phase present. Unfortunately, XRD and EDS measurements indicate that CZTSe must be concentrated in a layer near the surface. XRD reveals strong CZTSe peaks, hence one can assume that this layer is not residual. In the rest of the film, no Se reaches the metals and different alloys of Cu-Sn and Cu-Zn are formed. By knowing that CZTSe is formed one can conclude that this material does not suffer from the same emissivity change seen in CIGS when passing from a Cu-poor state to a Cu-rich state since no EPD signal was ever observed. In order to work with the hybrid system, a pressure of 1 x 10^{-3} mbar to 10 x 10^{-3} mbar is required to sustain the sputtering plasma. The biggest problem encountered was the diffusion of Se into the film. One way of solving this problem could be raising the temperature of the substrate. But at these pressures there was already evidence of losses of Sn and hence increasing the temperature would even worsen this problem. It is then evident that the hybrid method is not the most suitable method to grow CZTSe.

4.2.3 Properties of the best CZTSe thin films

The best CZTSe thin films were grown by selenization of metallic precursors at a substrate temperature of 520 ºC, Se evaporator temperature of 345 ºC and at a pressure of 1 mbar [VI]. Several samples with similar precursors were grown and were subjected to a KCN etching. The results of the composition and the adhesion of the films are presented in Table 4-15. It can be seen that most of the samples that are Zn-rich showed a poor adhesion. The samples grown on SLG even peeled off and some of these samples showed some dots with a yellowish colour after the KCN but not before. This indicates that there was some ZnSe at the back of the films.

Table 4-15: Elemental composition of various CZTSe samples grown at 1 mbar and 520 ºC.

sample name	substrate	[Cu]/([Zn]+[Sn])	[others]/[Se]	[Zn]/[Sn]	[Cu]/[Zn]	[Cu]/[Sn]	adhesion after KCN
CZTSe_2009_12_04	Mo	0.9	1.0	0.9	1.9	1.7	good
CZTSe_2010_02_13	Mo	1.0	1.0	1.3	1.8	2.3	peeled off
CZTSe_2010_02_15	Mo	1.4	0.9	0.9	3.0	2.7	poor
CZTSe_2010_02_17	Mo	1.0	1.1	0.8	2.3	1.8	poor
CZTSe_2010_02_10	SLG	0.9	1.0	1.1	1.6	1.8	peeled off
CZTSe_2010_02_12	SLG	0.9	1.0	1.1	1.7	1.8	peeled off

The best sample of this series was sample CZTSe_2009_12_04 and so it was decided to study it further. The corresponding surface SEM micrograph of the film is shown in Figure 4-28 a), and it shows an open morphology with some voids, however, at the bottom part of Figure 4-28 b) the cross section of the sample reveals a compact film with some small grains at the bottom. The film appears to have around 1 μm of thickness.

Figure 4-29 a) and Figure 4-29 c) shows an atomic force microscopy, AFM, surface topography image of the sample CZTSe_2009_12_04. This image indicates a rough, but compact, surface in agreement with the SEM cross section observations. The corresponding electric force frequency shift image, obtained with the AFM system, is presented in Figure 4-29 b). No significant contrast changes are observed in this image, revealing that different grains of the sample have very similar electrical properties. From these images, it is possible to conclude that the material is single phased and has no large composition variations. The AFM images show a rough and compact thin film with small grains of approximately 325 nm of diameter at the bottom, and bigger grains of approximately 1000 nm of diameter at the top. The root mean square roughness of the sample was 77 nm which seems a rather low value when looking at the apparent rough surface of the sample. This difference comes from the fact that in the SEM micrograph the small grains at the bottom were not visible whereas in the AFM image those can be seen.

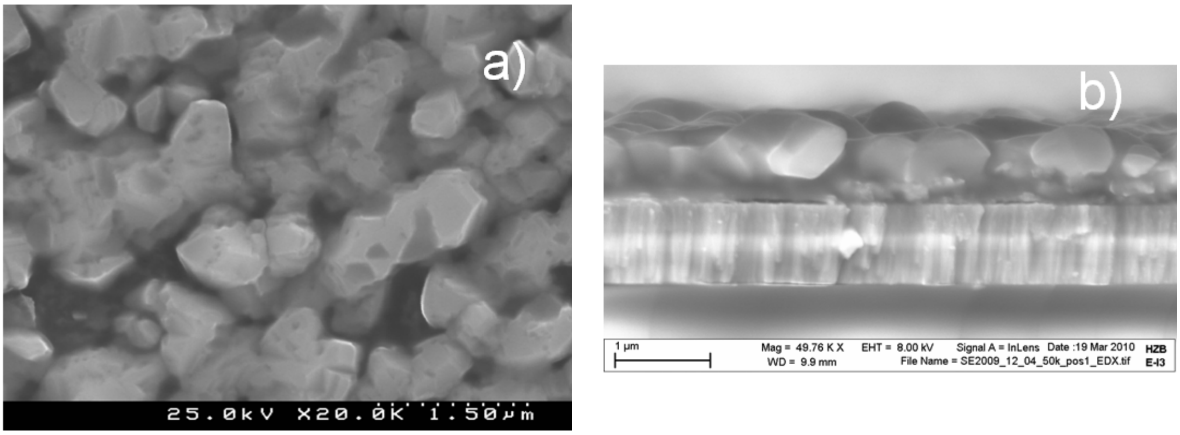

Figure 4-28: a) SEM micrograph of the surface of the sample CZTSe_2009_12_04; b) SEM micrograph of the cross section of the same film.

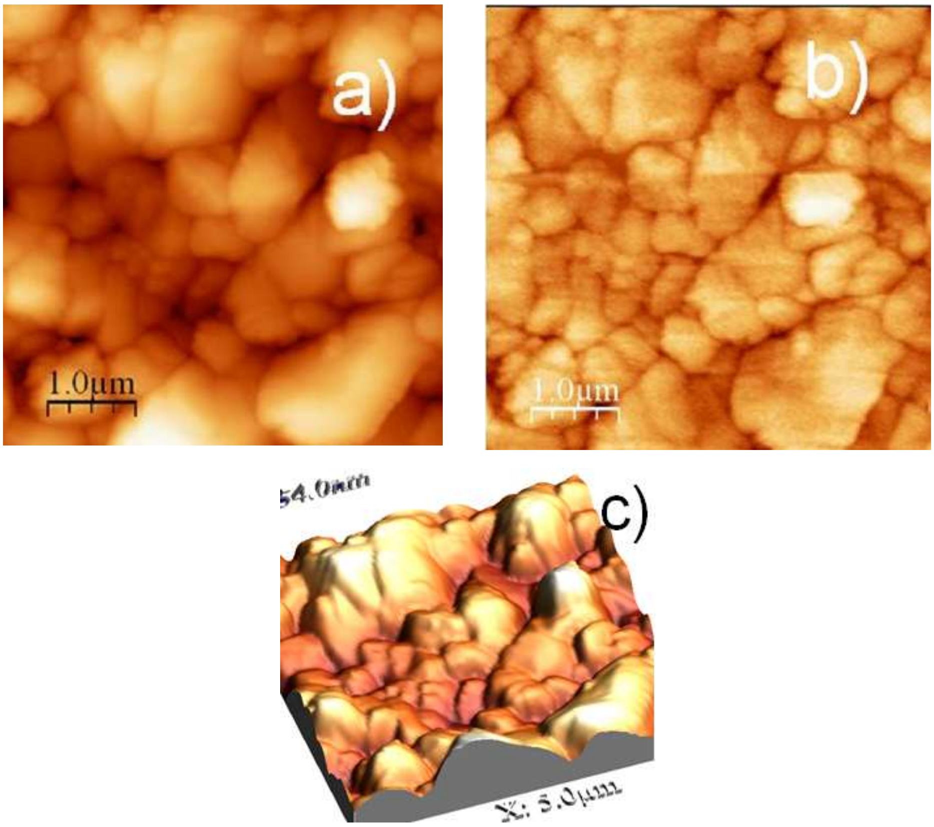

Figure 4-29: AFM images of the surface of the sample CZTSe_2009_12_04. a) topography image; b) electric force frequency shift image. The z-scale in images a), b) are 400 nm, 10 Hz. c) 3D view of the surface.

The EDS mapping of the cross section was done, and in Figure 4-30 the normalized EDS intensity counts for each element as function of depth is represented. The shape of the curves does not show an abrupt variation because of the interaction volume of the EDS probe, see Figure 4-31 where different interaction volumes are illustrated. That is also the reason why Mo appears to be mixed with the film but a simple inspection of the SEM cross section image, shown in Figure 4-28, shows that it is an artefact of the measurement as shown in point 3 of Figure 4-31. These results suggest a higher concentration of Zn at the top of the CZTSe film than at bottom. The concentration of Sn exhibits the opposite behaviour while the concentrations of Cu and Se have a similar variation. Other than this, the sample seems uniform in depth.

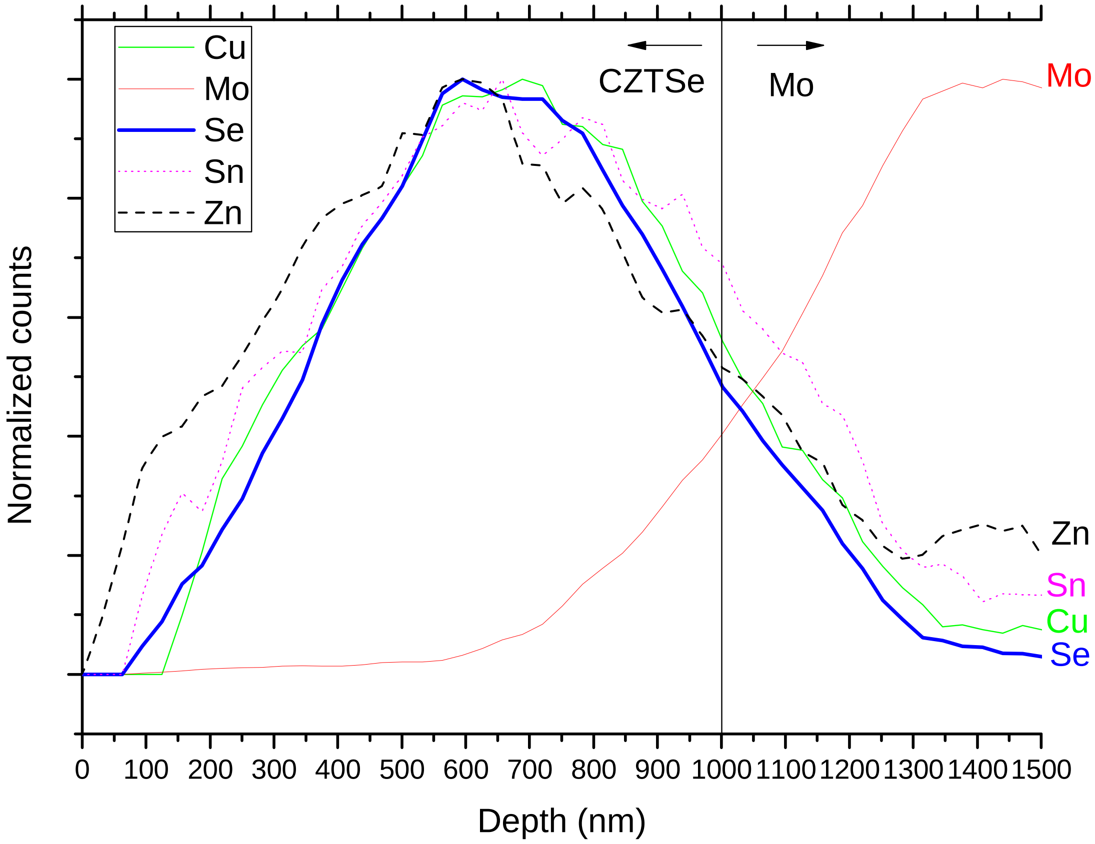

Figure 4-30: Representation of the normalized EDS intensity counts for each element as function of depth for a cross section of the CZTSe film.

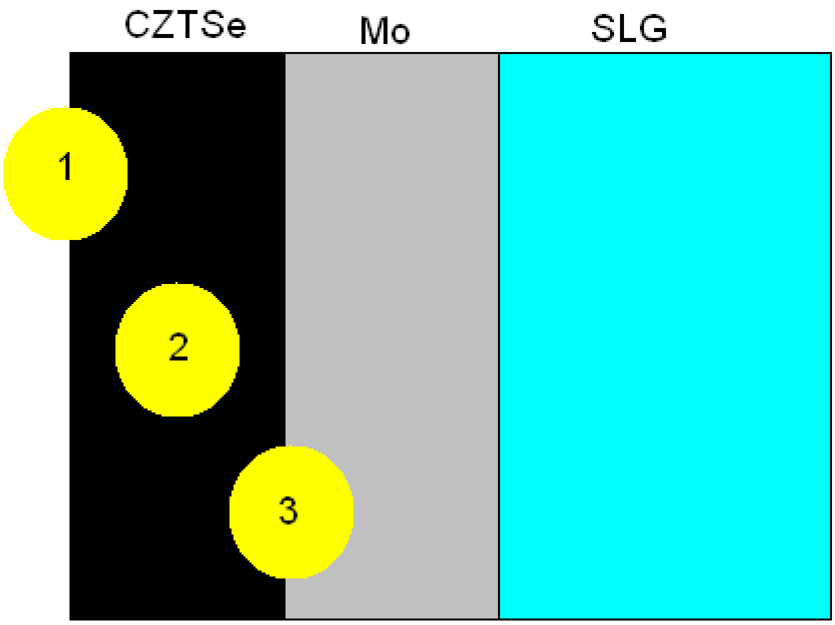

Figure 4-31: Illustration of different EDS interaction volumes for measurements 1, 2 and 3 for a CZTSe cross section.

The presence of CZTSe with the kesterite/stannite structure was confirmed using XRD, see Figure 4-32, where the main diffraction peaks for this structure are presented. No compounds other than CZTSe and Mo were found. These results show that the sample has a good cristallinity as confirmed by the low value of FWHM, less than 0.11 °, and the higher intensity of the (1 1 2) peak than that of the Mo main peak. To further confirm the presence of CZTSe and the absence of unwanted phases, the samples were also analysed using Raman scattering and the three main peaks of CZTSe were found at 174 cm^{-1}, 194-197 cm^{-1}, and 232-236 cm^{-1} as depicted in Figure 4-33. Although the EDS mapping showed an apparent higher concentration of Zn at the top of the film, no ZnSe phases were detected. Since these measurements are done in a micrometer spatial scale, several measurements were carried out and in a small number of them, traces of $Cu_{2-x}Se$ were found. Despite the fact that this compound was not found in XRD, one can assume that it is present in very small localized spots. After the KCN etching there was no change in the XRD spectra and the $Cu_{2-x}Se$ peaks were no longer found in Raman scattering.

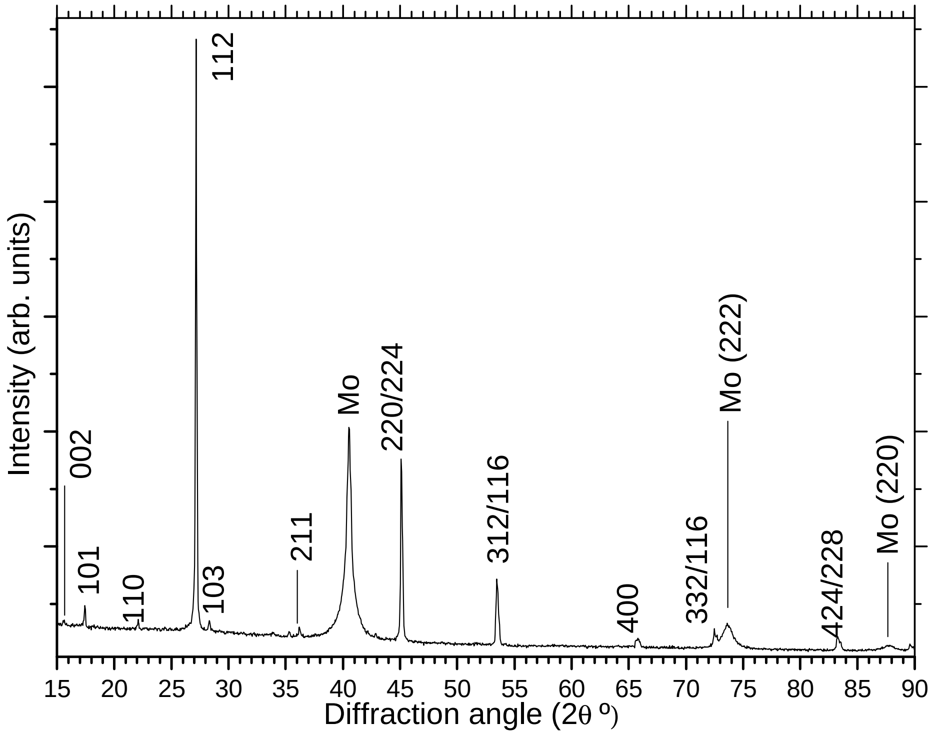

Figure 4-32: XRD diffractogram for the best CZTSe film.

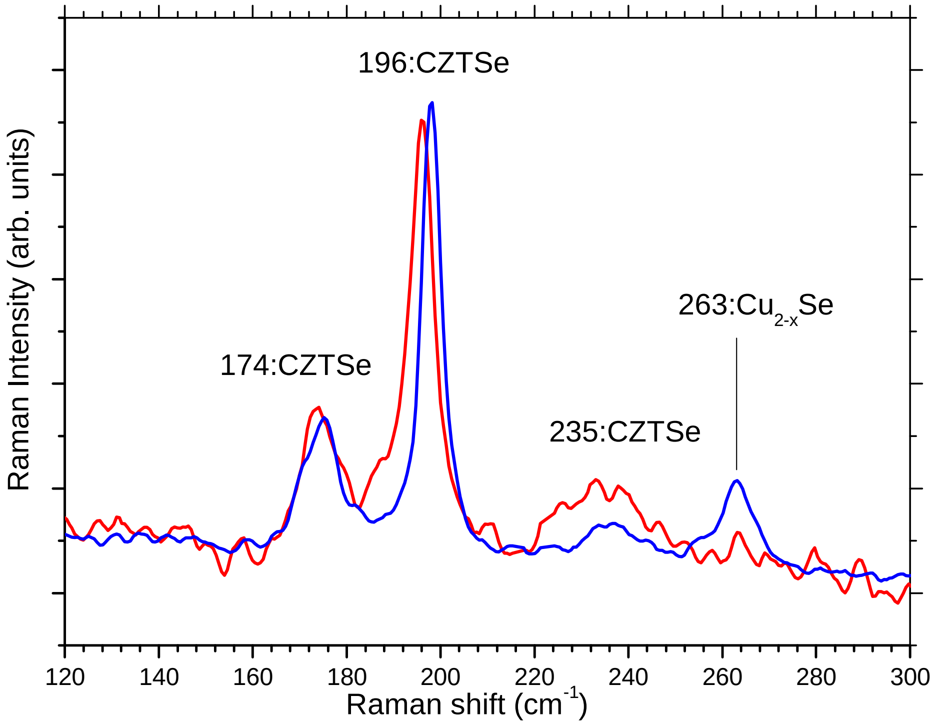

Figure 4-33: Raman scattering analyses for two different points of the same sample before the KCN treatment.

The film was analysed by XRD with the objective to make *Le Bail* refinements. To this end a long time measurement with a small step was needed. Therefore a measurement with a step of 0.01° and 2.55 seconds per point was made. The result is presented in Figure 4-34. The resolution is so high, that even the $K_{\alpha2}$ diffractions are detected. To analyse this kind of diffractograms, with several peaks presents, a simple manual check is not enough so a *Le Bail* refinement was done. Besides Mo and CZTSe, very small traces of SnO were detected as well. The peaks are so low that the identification was not done in the figure.

The general results of the refinement are shown in Table 4-16. The method compared the kesterite and the stannite structure. The lattice parameters are the same, since the method is based on the fitting of the position of the peaks. Changes were noticed in the value of the anisotropic stress, in which the kesterite sample showed a slightly smaller value, 9.42 % against the 9.48 % for the stannite and in the grain size, 637 nm in the kesterite versus 571 nm in the stannite. Since the numbers of reflections in both structures is not the same, a statistical analysis is needed to evaluate which is the most likely phase. For this the Hamilton method was performed [135]. Since the results are important but it was not the author himself who performed these analyses only the results are discussed and not the specifics of the method.

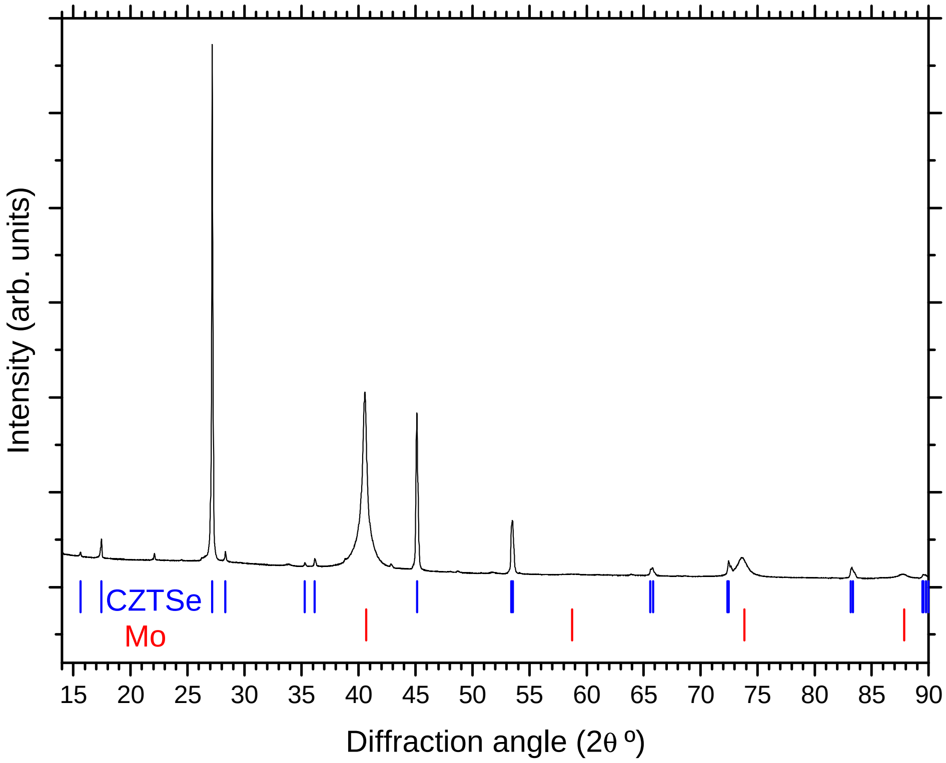

Figure 4-34: Long time XRD diffractogram for sample CZTSe_2009_12_04.

The Hamilton method proved with a 99% certainty that the structure present was kesterite rather than stannite. Also according to Person [98] the band gap energy for the kesterite CZTSe is 1.05 eV and for the stannite 0.89 eV. The kesterite's value is identical to the band gap energy value that was estimated and therefore there are two different methods pointing to the kesterite structure.

Table 4-16: Results from the *Le Bail* refinement.

	Stannite I42m	**Kesterite I4m**
a (Å)	5.6799	5.6799
c (Å)	11.37993	11.37993
Vol. (Å^3)	367.131	367.131
number of reflections	192	278
Average maximum strain and standard deviation (anisotropy) (%):	9.4847	9.4215
size (nm)	571.334	637.742

The absorption coefficient, α, was estimated from the transmittance and reflectance measurements made in samples CZTSe_2010_02_10 and CZTSe_2010_02_12 using the equations described in section 3.5.5. The reflectance and the transmittance of the film are shown in Figure 4-35.

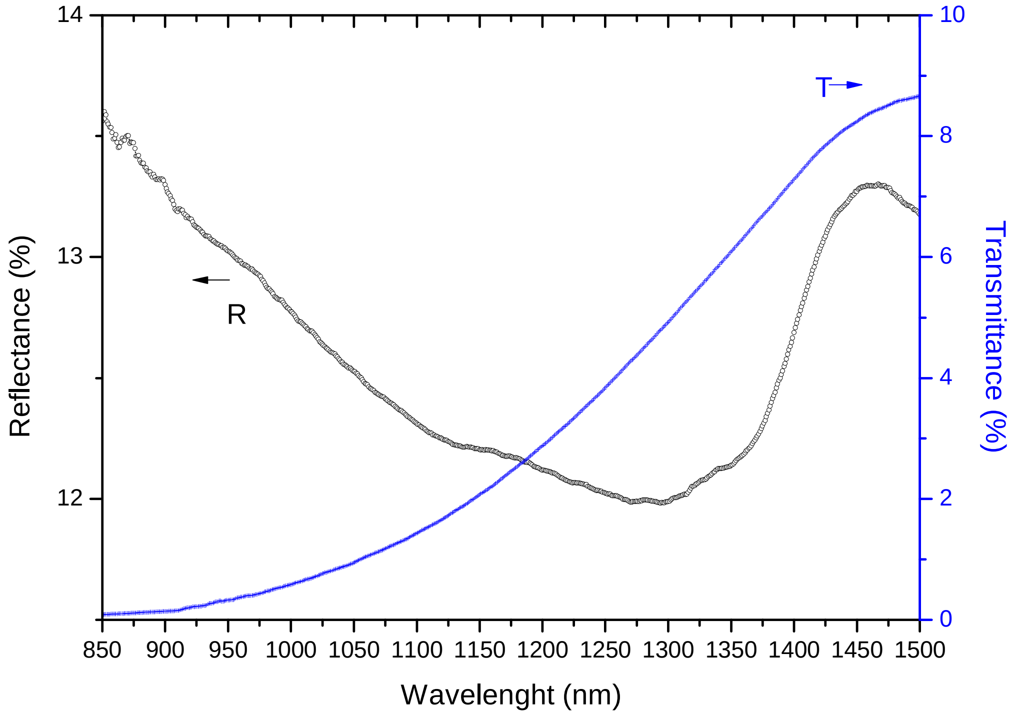

Figure 4-35: Transmittance and reflectance values for sample CZTSe_2010_02_10 grown on SLG at 1 mbar and 520 ºC.

The behaviour of the absorption coefficient with the photon energy is shown in the inset of Figure 4-36. The absorption coefficient is higher than 4 x 10^4 cm^{-1} for photon energies higher than 1.5 eV. This value is smaller than the usual referenced value of 10^5 cm^{-1} for CIGS but it is still high enough for the desired objective. From the linear fit of $(\alpha h\upsilon)^2$ vs. photon energy one obtains the value E_{gap} as shown in Figure 4-36. The band gap was then estimated to be 1.05 eV ± 0.05 eV. This value is consistent with the one reported experimentally by Grossberg [82].

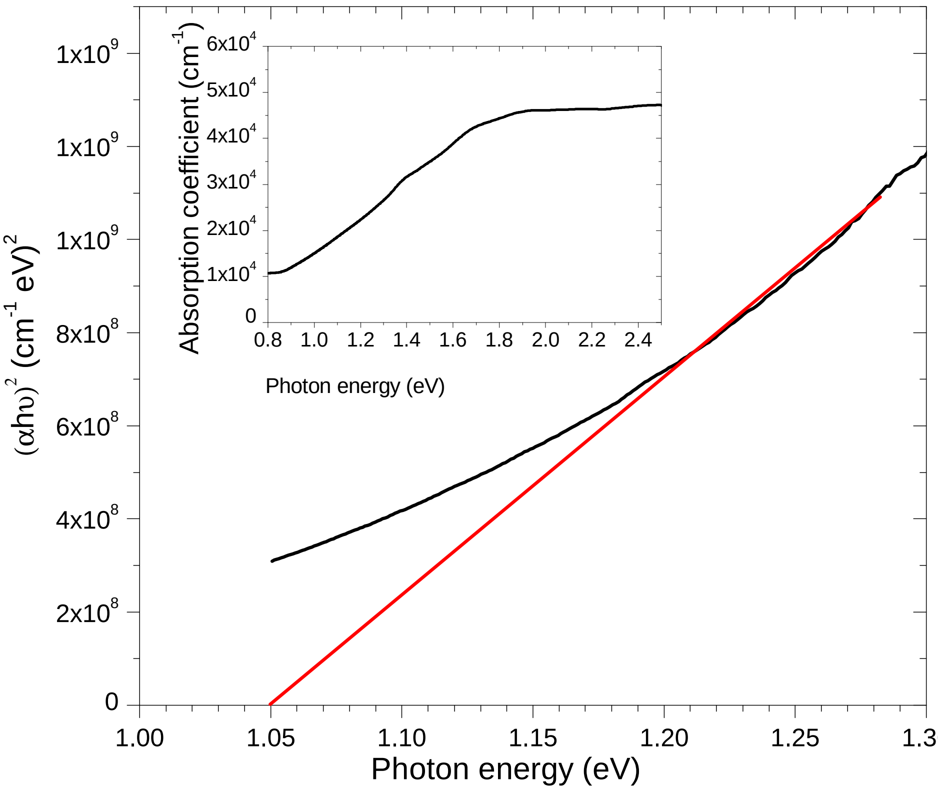

Figure 4-36: Band gap estimation for sample CZTSe_2010_02_10. The inset shows the absorption coefficient versus photon energy.

Figure 4-37, depicts the photoluminescence spectra for different temperatures of the sample CZTSe_2009_12_04. This sample was chosen for these measurements because it was the best characterized until then. The observed emission is a broad asymmetrical peak centred at 0.935 eV and is similar to the emission reported by Grossberg et al. [82] for CZTSe mono-grains. As temperature increases, it was identified a decrease in the intensity of the photoluminescence as expected owing this fact to the thermal activation of non-radiative de-excitation channels. This emission was only measured in samples grown on

SLG/Mo, for the samples grown directly on SLG no signal was detected. A detailed study of the PL emission was not done during the work leading to this thesis but some results were obtained and are the following: i) the emission peak shifts from 0.93 to 0.88 eV when the temperature changes from 20 K to 300 K; ii) the emission is broad with a width varying between 120 and 150 meV; iii) the variation of the intensity with temperature suggests a defect with an activation energy around 140 meV and, iv) there is a red shift in the peak position with the increase of temperature. The emission indicates a mechanism based on fluctuating potentials but extra electrical analyses would be needed to confirm it. All of these findings are in good agreement with the analysis made in CZTS which also pointed to an emission due to fluctuating potentials [i,ii]. These PL results are consistent with the band gap energy value estimated above.

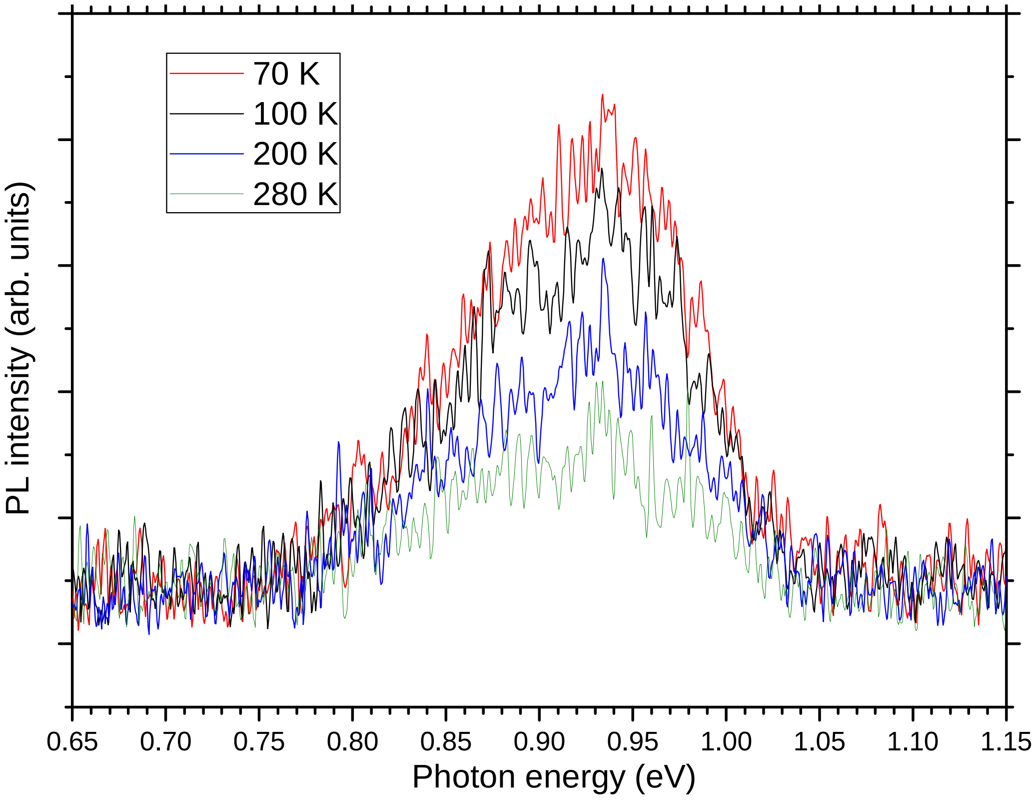

Figure 4-37: Photoluminescence at 70 K, 100 K, 200 K and 280 K, with an excitation power of 300 mW using a wavelength of 488 nm for the sample grown at grown at 1 mbar and 520 ºC.

4.3 CZTSSe

The first tests to grow CZTSSe were based in the selenization of CZTS. CZTS thin films were grown by sulphurization of metallic precursors at a substrate temperature of 525 ºC at a pressure of 5 mbar and next were selenized at two different pressures, 10^{-5} mbar and 10^{-3} mbar at a substrate temperature of 450 ºC. No differences were noticed in the analysis made of the films prepared at both pressures. In terms of composition, only small traces of Se were found with none of the samples having a ratio of [Se]/[S] higher than 0.02. The quantity of S is problematic to evaluate because of the coincidence of its X-ray emission with that of Mo. All samples showed small losses of Zn and Sn. But the quantity evaluation of Se in the sample is a problem. It has already been shown that EDS is not a suitable technique to evaluate the composition of layered structures, as it is the case. Without the proper techniques like SIMS, XPS with an ion gun to wear out the surface or even GI-XRD it is extremely difficult to evaluate the quantity of Se in the sample.

In Figure 4-38, the SEM micrograph of the CZTS film and the selenized film are presented. There is a noticeable change in the morphology of the sample and it appears that in certain areas the selenization promoted a smoother surface but with some cracks. Due to the small quantity of Se present, one may ask if these changes are due to the influence of the Se in the structure or if the selenization only acted as an annealing. This question is answered by looking at the reflectance of the samples in Figure 4-39, where substantial changes are observed. The reflectance for a CZTS film is shown, black line, in that line a well defined band gap transition curve is seen starting around 850 nm, 1.47 eV. However, for the selenized CZTS samples, such well defined transition is not observed, instead a more diffuse and less steep transition occurs. This proves that some surface modification of the samples was made and is probably due to incorporation of Se in the surface, thus diminishing the band gap energy.

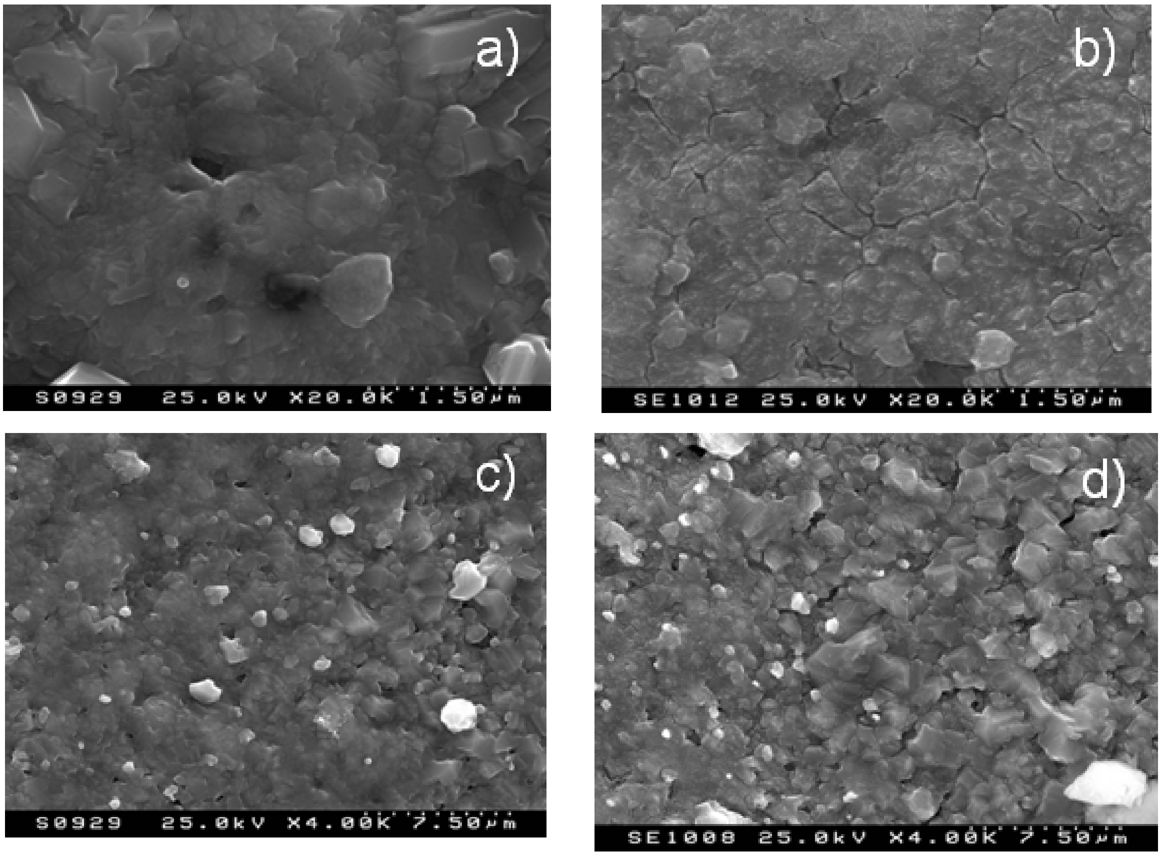

Figure 4-38 a) and c) SEM micrograph of the surface of the CZTS films before selenization, b) and d) SEM micrograph of the surface of the selenized films.

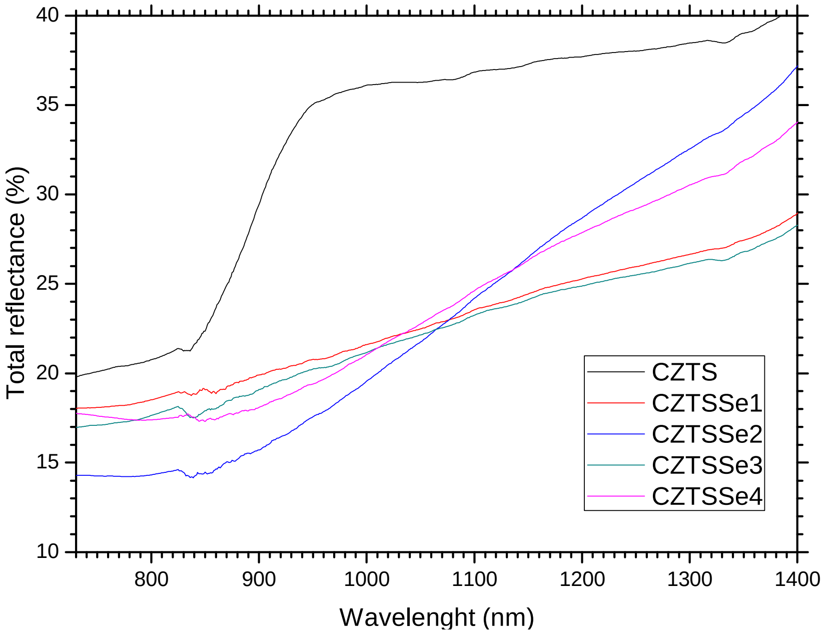

Figure 4-39: Reflectance of CZTS and CZTSSe samples.

Since a XRD analysis showed no difference in the diffractograms before and after the selenization, Raman scattering analysis was performed as shown in Figure 4-40. It was detected CZTS with peaks at 288 cm^{-1}, 338 cm^{-1} and 352 cm^{-1} [VII]. Despite being only a small peak, CZTSe was identified with a broad peak at 195 cm^{-1}. The existence of $Cu_{2-x}Se$ may not be discarded because a very small peak may be present around 262 cm^{-1}. More information on the Se-compounds and S-compounds Raman peaks is found in Annexes A and B, respectively.

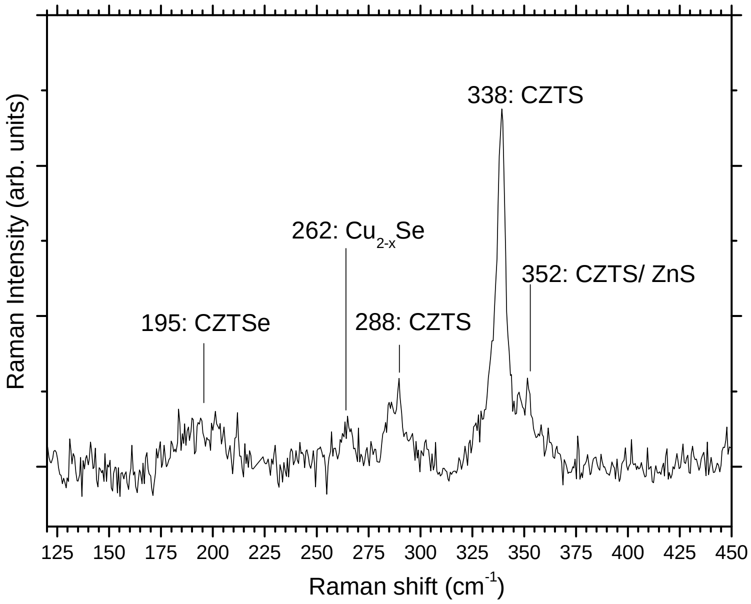

Figure 4-40: Raman scattering spectra for a selenized CZTS sample.

After these initial tests, it was decided to use a series of different precursors deposited by thermal evaporation at the HZB. The objective of this test was to understand better the Se diffusion into CZTS films. The details for each precursor are presented in Table 4-17. There were six different samples, all selenized in the same conditions, 1 mbar and a substrate temperature of 520 ºC. Sample ZTC S consisted of a multi-layer stacking of SLG/Mo/ZnS/SnS_2/$Cu_{2-x}S$ deposited by thermal evaporation. ZTC metal had metallic layers of Zn and Cu and only had sulphur in the form of SnS_2 making the following order: SLG/Mo/Zn/SnS_2/Cu. In all the other samples, the only layers deposited at HZB were SnS/CuS. In those samples and prior to the incorporation of Zn, the samples were submitted to a thermal treatment in an S atmosphere in order to form a phase of Cu-Sn-S, probably cubic Cu_2SnS_3 [iii,iv]. In sample 60Se, elemental Zn was deposited by RF sputtering in Aveiro and CZTS was formed before the selenization. In sample 64Se instead of Zn, ZnS was deposited and CZTS was formed as well. In samples 63Se and 59Se, CZTS was not formed and it was deposited ZnS and Zn, respectively. This way there are several questions regarding the formation of CZTSSe that can be raised and answered. Is the formation of ZnS prejudicial? Is CZTS stable enough not to allow the diffusion of Se into the film? What is the difference between having the sulphur already in the film and using metal layers?

Table 4-17: Growth details of the CZTSSe samples.

Sample name	Precursor details
ZTC S	ZnS/SnS/CuS
ZTC metal	Zn/SnS/Cu
60Se CZTS Zn	CZTS formed by sulphurization of SnS/CuS/Zn
64Se CZTS ZnS	CZTS formed by sulphurization of SnS/CuS/ZnS
63Se CTS ZnS	CTS/ZnS
59Se CTS Zn	CTS/Zn

The sulphurized precursors were analysed by SEM and by XRD. The cross section micrograph, shown in Figure 4-41, shows a compact film with a columnar structure where the surface micrograph shows a rough surface. The XRD diffractogram is shown in Figure 4-42 and several phases were identified other than Mo. The diffraction peaks associated with the structures of Cu_2SnS_3 tetragonal and Cu_2SnS_3 cubic, which have the same peak positions, are identified as well as Cu_2SnS_3 monoclinic and Cu_3SnS_4 orthorhombic [100]. Due to the higher intensity of the peaks, Cu_2SnS_3 cubic/tetragonal seems to be the dominant phase.

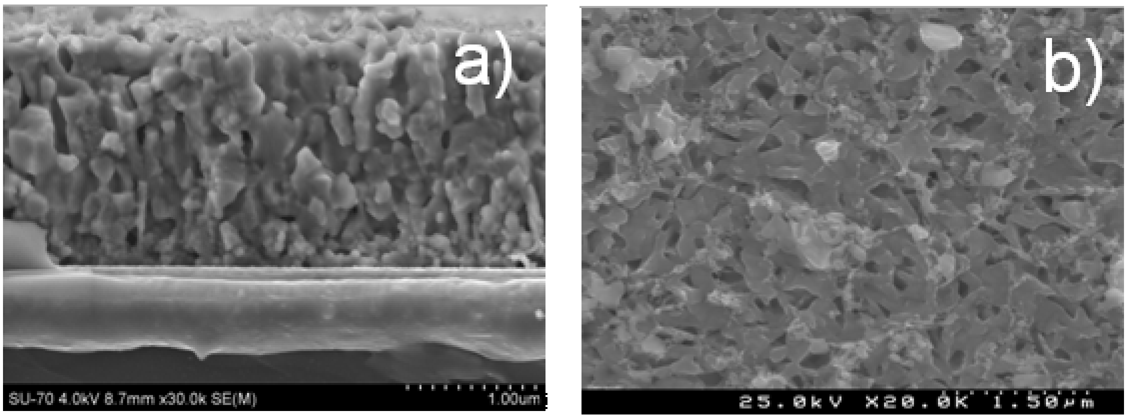

Figure 4-41: a) SEM micrograph of the cross section of the CTS film and b) SEM micrograph of the surface.

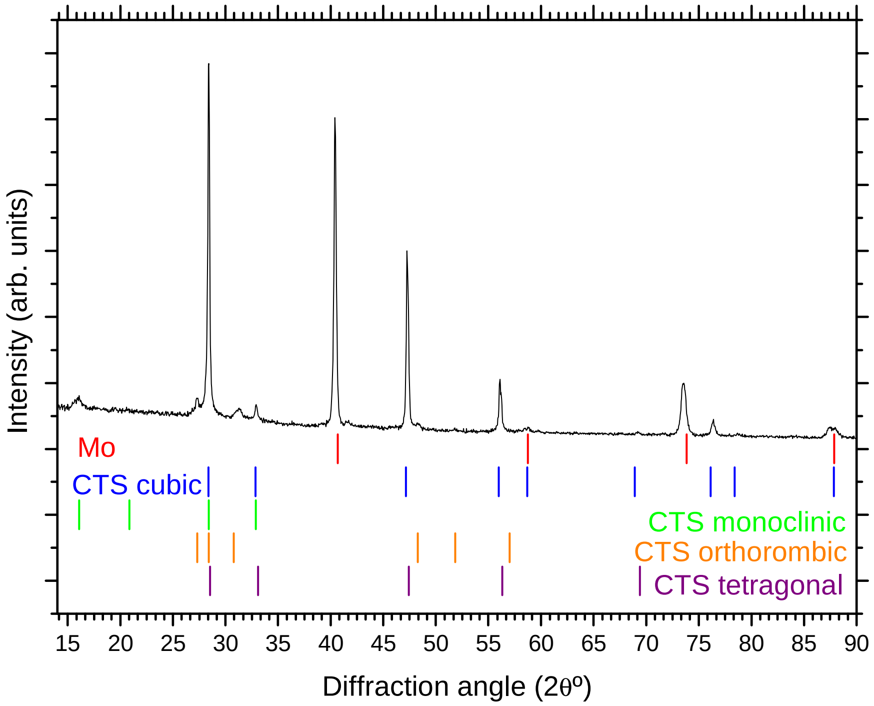

Figure 4-42: XRD diffractogram of the CTS film.

For the analysis of the CZTSSe films, XRD and SEM micrographs of the cross sections were used. The XRD allows the estimation of the quantity of Se by looking at the shift of the 112 peak. It is known that for CZTSe this peak is centred at 27.14 º and for CZTS is centred at 28.44 º. The SEM micrograph of the cross section and the EDS mapping with the counts for Se can both reveal important information about the morphology.

The EDS mapping analysis, shown in Figure 4-43, showed for all the samples that Se was mainly concentrated at the surface. This alone is useful information and indicates that the Se diffusion is low. The morphology of the resulting CZTSSe films is depicted in Figure 4-44. Sample ZTC Metal is the most compact one showing large grains at the top and smaller ones close to the back. The samples where all the precursors were deposited at the HZB show a similar open columnar structure. For sample ZTC S, the cross section micrograph shown has the complete cell structure, the image illustrates a rather compact film. Sample 60Se CZTS Zn has a voided columnar structure. Sample 64Se CZTS ZnS has likely a Zn(S,Se) layer at the top which is visible in the micrograph and was identified using the EDS mapping. Underneath that layer, this sample has the voided columnar structure similar to the other samples. Sample 59Se CTS Zn has larger grains than the other samples but at the same time the voids are bigger as well. Sample 63Se CTS ZnS has the generic structure that all the other samples show but at the top it appears to have a different layer, however, the EDS mapping showed no significant changes in the metal composition. The EDS mapping only revealed a higher concentration of Se at the top.

ZTC S ZTC Metal

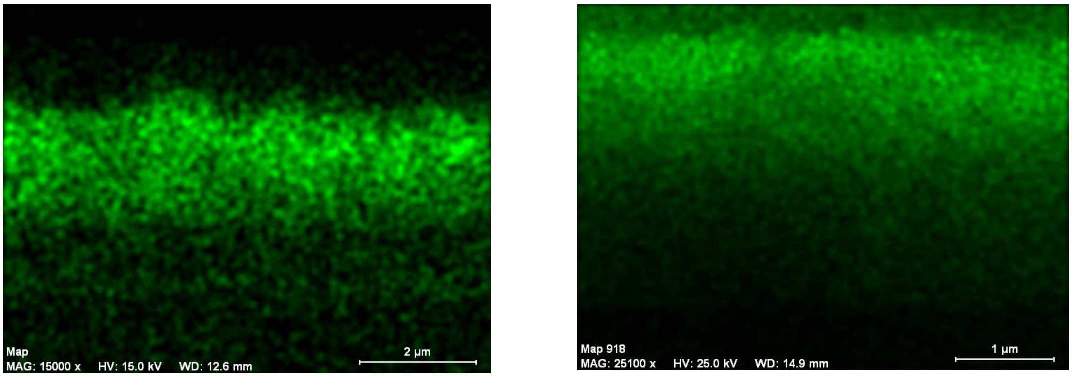

60Se CZTS Zn 64Se CZTS ZnS

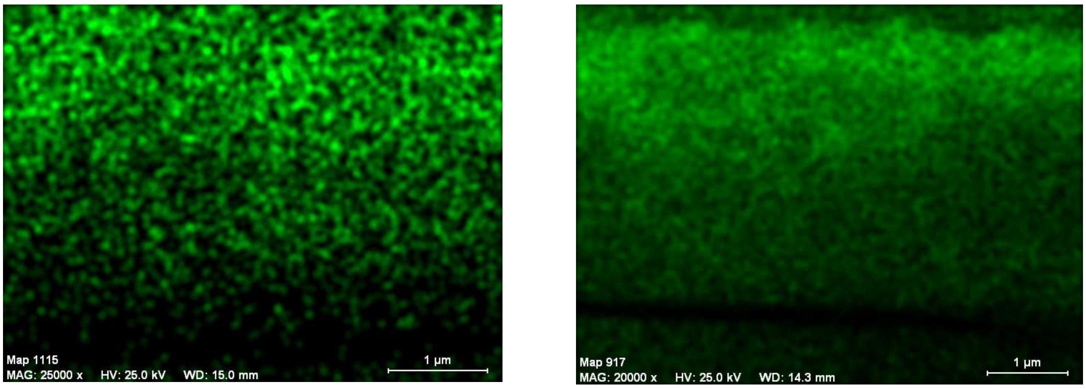

59Se CTS Zn 63Se CTS ZnS

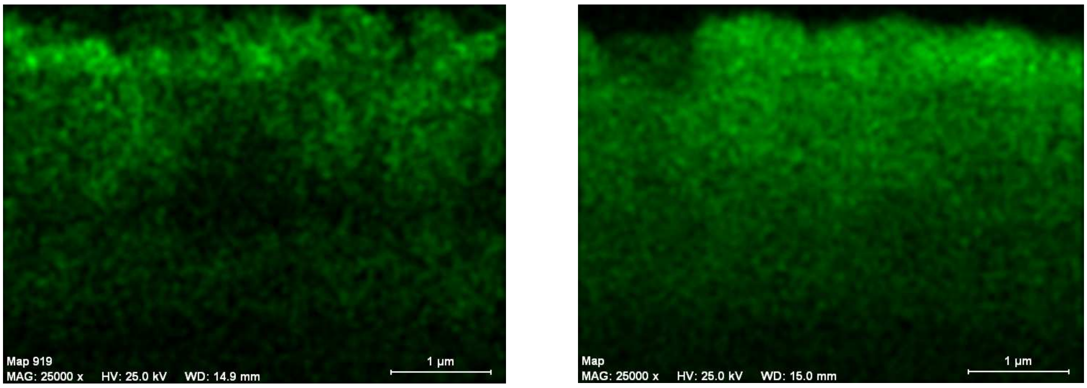

Figure 4-43: EDS mapping representing the presence of Se in the cross section of various CZTSSe samples.

ZTC S ZTC Metal

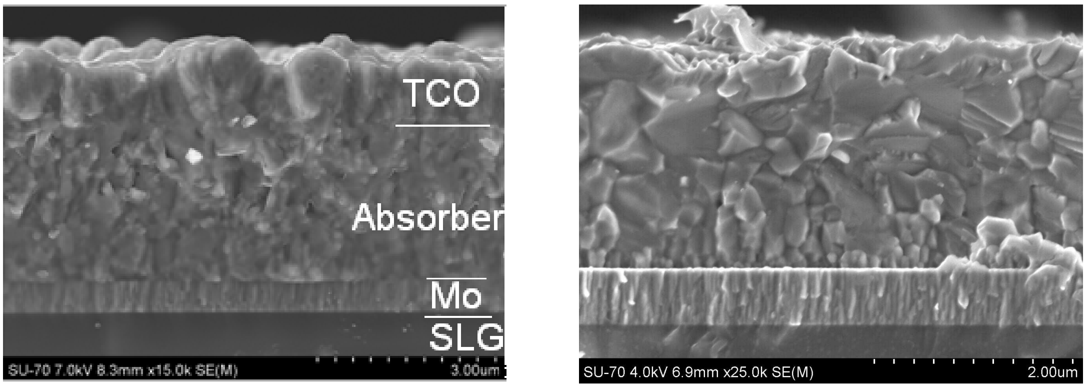

60Se CZTS Zn 64Se CZTS ZnS

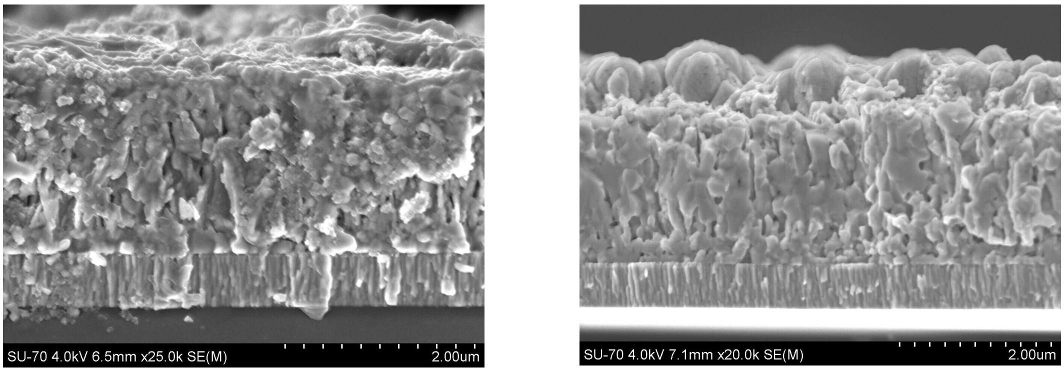

59Se CTS Zn 63Se CTS ZnS

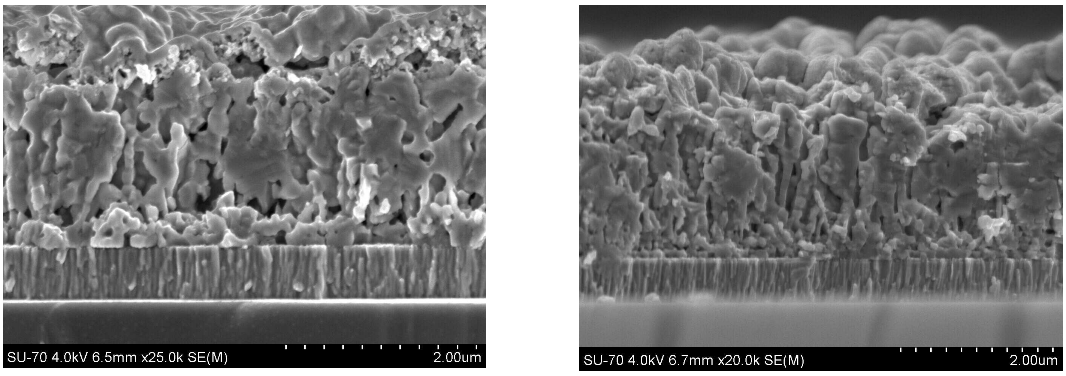

Figure 4-44: SEM micrograph of the cross section of various CZTSSe samples.

In the XRD analysis, the position of peak (1 1 2) of the studied CZTSSe samples is depicted in the diffractogram of Figure 4-45. The full diffractogram is represented in Figure 4-46. The position of peak (1 1 2) for CZTSe, at 27.14 ° and CZTS, at 28.44 °, is shown as a vertical line for reference. All the samples show a peak corresponding to CZTS which indicates that they all have a layer of pure CZTS. This layer is, then, located at the back of the samples, and Se does not reach there like the EDS mapping illustrates. Also, all the samples demonstrate a complex structure between CZTSe and CZTS which may be from several phases like $Cu_2ZnSn(S,Se)_4$, $Cu_2Sn(S,Se)_3$, Zn(S,Se) or even a broadening of the peaks originating from a Se grading from top to bottom. One possibility to precisely evaluate the origin of these emissions is to make Raman scattering on the cross section as well. Such measurements are very hard to do because of the focusing of the spot and mostly due to the size of the laser spot which varies between 1 µm and 10 µm. Besides it would require a high resolution and very stable sample stage which the group does not have. Instead the interpretation of these XRD diffractograms will be made assuming that the emissions observed between the two positions are from CZTSSe. Assuming that the shifting of the peak follows a linear trend, the peak position as function of [S]/([S]+[Se]) is presented in Table 4-18. From the relation of the peak intensities, one can assume that it is likely that high intensities mean that the phase originating that peak is more present than another phase.

Table 4-18: Linear interpolation of the position of the (1 1 2) Kesterite peak as function of the S content.

(1 1 2) peak position (º)	[S]/([Se]+[S]) x 100
27.14	0
27.24	8
27.34	15
27.44	23
27.54	31
27.64	38
27.74	46
27.84	54
27.94	62
28.04	69
28.14	77
28.24	85
28.34	92
28.44	100

Sample ZTC metal is the only one showing a well resolved peak at the CZTSe position, indicating the existence of a layer of CZTSe in its structure. This sample is also the one with the second peak closest to the CZTSe rather than to the CZTS. The latter is also stronger than the CZTS or the CZTSe peaks. From this observation one can say that this sample is the one with the higher content of Se and is comprised by at least three different layers. Although this sample had the largest grains and best morphology, one can not say that this is due to the influence of Se since this precursor was different from the others

Sample ZTC S shows a strong broad peak at 28.0º. Comparing the position of this peak with the estimated values in Table 4-18, this peak indicates that the sample must have a layer with a content of 70% of S on average besides a pure CZTS layer. Both ZTC samples have the strongest peaks which are not CZTS peaks, this may indicate that CZTS is not the dominant phase and the incorporation of Se was somehow successful.

Sample 60Se CZTS Zn shows a strong peak at 27.95 º and is the one, along with samples ZTC S and ZTC metal, which has a peak from the mixture stronger than the CZTS peak. This position points to a mixture of 60% S and 40% Se. Along with sample ZTC S, these are the only two samples that showed no evidences of CZTSe.

The broadening of the CZTS (1 1 2) peak for higher angles in sample 64Se CZTS ZnS may suggest that there is some ZnS present but no conclusion can be taken regarding the presence of ZnS. The intensity relation between the second peak present and the CTZS peak is also low which indicates that there was a smaller incorporation of Se into the sample.

Sample 63Se CTS ZnS showed, in the SEM micrograph, a structure at the top which might be ZnS but no significant shoulder at higher angles in the CZTS peak is found. The EDS mapping shows a layer of Se at the top so the difference in the morphology could come from the Se incorporation or from the formation of Zn(S,Se). In this sample, a peak can be found at 27.7 º which could be from a CZTSSe phase with 40% S and 60% Se.

As mentioned before, Sample 59Se CTS Zn has a peak at the CZTSe position which indicates that CZTSe is present. From all the studied samples, this is the one that appears to have a smoother grading of Se since the intensity of the peaks lowers continuously from the CZTS to the CZTSe peak.

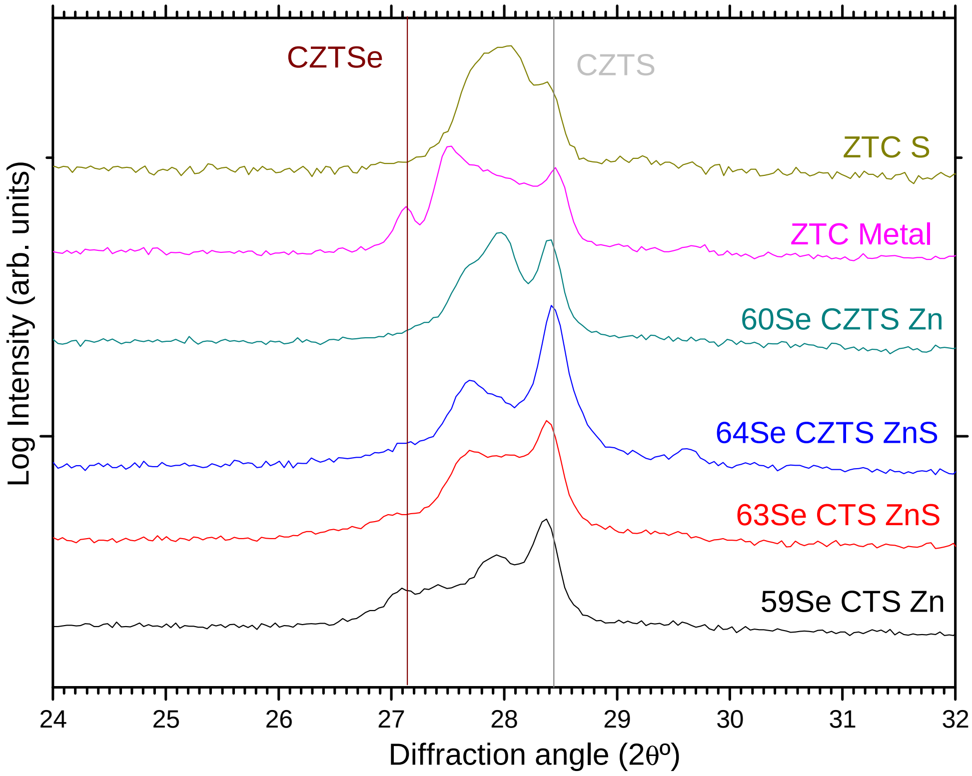

Figure 4-45: XRD diffractogram centred at the (1 1 2) kesterite peak for the CZTSSe samples.

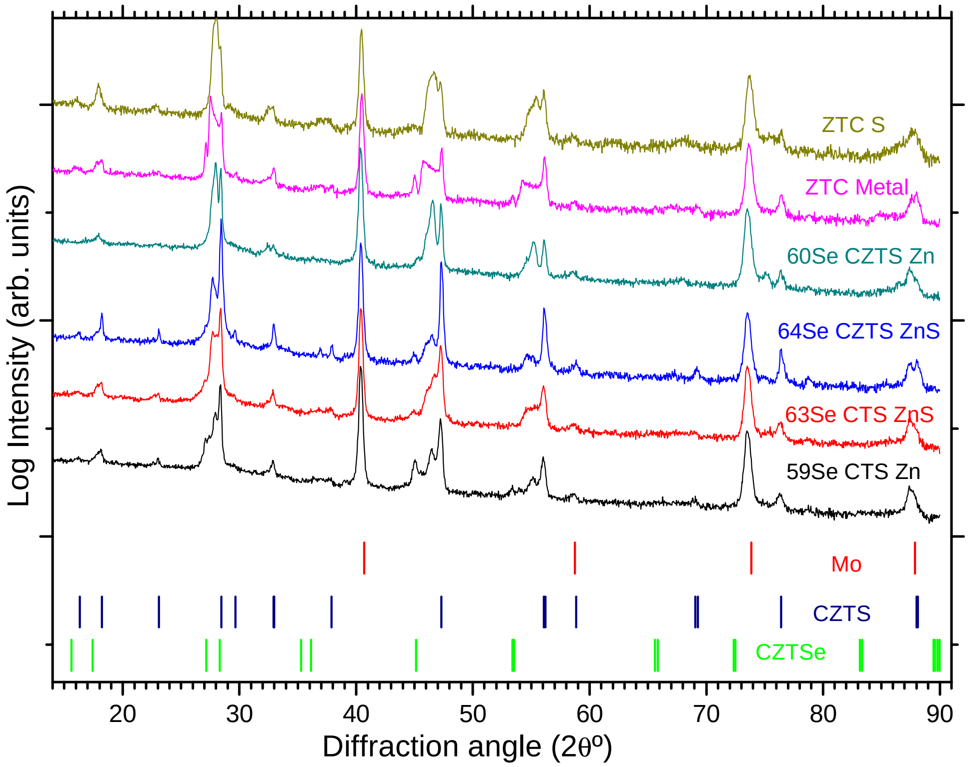

Figure 4-46: XRD diffractogram of the CZTSSe samples.

From these structural and morphological analyses, there were three samples that presented more distinctive results: ZTC S, ZTC metal and 59Se CTS Zn. Sample ZTC S confirmed a strong and broad intermediate diffraction peak and was chosen to be finished as a solar cell. The sample with the best morphology was ZTC metal and it also revealed a strong intermediate peak closer to CZTSe. Due to the presence of the CZTSe peak and the fact that it showed a quite strong peak near CZTSe, this was probably the sample with the highest Se content. Sample 59Se CTS Zn was the one from the sulphurization of precursors that indicated a continuous of peaks between CZTS and CZTSe and is the one with the smoothest Se grading. The samples where the CZTS was formed presented both strong CZTS peaks and the 64Se CZTS ZnS had a ZnS layer. The fact that the CZTS was not formed and Zn was in its metallic form was probably an important factor to allow the diffusion of Se into the film.

5 Solar cells using the new absorber materials

5.1 Solar cell structure

In the first chapter, the structure of a solar cell was presented. The usual structure for this type of thin film solar cells is SLG/Mo/absorber layer/CdS/TCO/ metallic grids/anti-reflection layer. In this thesis, all the presented Mo films are bilayer-type and no anti-reflection layer or grids were used. For the TCO different materials were used. In a first approach and for the CIGS films, it was used ITO deposited by DC-magnetron sputtering in Aveiro. The CZTSe solar cells have an i-ZnO/ ZnO:Al window layer deposited at the HZB and the CZTSSe solar cells have a GZO. In this chapter, only the deposition of the ITO layer is explained because it was the one prepared by the author.

Before presenting the results for solar cells the details of the properties of the used substrate are given and next an explanation of the development of a Mo-bilayer is described. Afterwards the CdS deposition process is explained and finally a brief elucidation of the ITO deposition process is presented.

5.1.1 Substrate

The substrate is not only a mean of mechanical support for the cell, its characteristics have influence in the properties of the absorber and there are a few requirements for the substrate that must be fulfilled:

- it must withstand the harsh growth conditions of the absorber, mainly high vacuum, high temperatures and not react with Se;

- the thermal expansion coefficients of the substrate and of the other layers must be similar so that during a panel’s lifetime the stress caused by temperature variation is low;

- have a smooth surface so that the cell layers are not influenced by the substrate’s morphology;

- be cheap, light, abundant and have low energy consumption.

Nowadays, the standard material for CIGS solar cells is soda lime glass (SLG). Amongst the points stated above, the most critical one is the thermal stability. SLG around 540 ºC starts to deform and loses its mechanical resistance.

A relevant fact in SLG is that it may be used as a source of Na for doping of the absorber layers. As shown in Table 5-1, there is a significant amount of sodium in the substrate. For CIGS solar cells, it is known that absorbers grown in the presence of Na have better efficiencies [58]. For the kesterites, only preliminary tests on CZTS have been done that give evidence that the presence of Na increases the grain size [136].

Table 5-1: Composition of the SLG substrates used in this thesis [137].

Compound	**SiO_2**	**Na_2O**	**CaO**	**MgO**	**K_2O**	**Al_2O_3**	**SO_3**	**Fe_2O_3**
Composition (%)	72.20	14.30	6.40	4.30	1.20	1.20	0.30	0.03

5.1.1.1 Cleaning of the substrates

When working with semiconductors, cleanness is a keyword. Since the work conducted was not made in a clean room, more caution was needed. The cleaning of the substrate started by a mechanical hand cleaning with acetone, ethanol and deionised water. After the manual cleaning, the samples were submitted, for 15 minutes, to a 70 ºC deionised water bath. Next, three ultrasonic baths consisting of 3 minutes each of acetone, ethanol and deionised water were done. After the last step, the substrates were passed again by deionised water and were dried with a N_2 flux. Until being used, the substrates were kept in a dry box.

5.1.2 Mo bilayer as back contact

The work described in this section refers to the back contact layer [VIII]. This layer has one main purpose which is basically to make the positive electrical contact of the cell. Although that is the main purpose, there are a few other requirements for this layer that need to be fulfilled: low resistivity; good adhesion to soda lime glass (SLG); low roughness; to be chemically inert with the materials deposited on top, mainly Cu, In, Ga, Se, Zn, Sn and S; be stable during the high growth temperatures of the CIGS; allow Na diffusion from SLG since the properties of CIGS films are influenced by the Na doping that occurs during growth; have a high reflectance in the visible spectrum; have a thermal expansion coefficient similar to SLG and CIGS and form an Ohmic contact with CIGS.

One material that meets almost all of those requirements is molybdenum. Mo is used by a large number of research groups and by the CIGS industry and it is already in the market as shown in Table 5-2. For comparison, it is also presented the CIGS growth method and the substrate. Despite the different methods and substrates used in all these companies, Mo, used as back contact, is common to all of them. Mo is a metal which can be deposited as thin films with a low resistivity, a good adhesion and with a fairly smooth surface. It does not react with Cu neither Ga nor In and although it reacts with Se, forming a $MoSe_2$ layer [138], there are small positive consequences reported for the solar cell performances [139]. Mo is also able to allow diffusion of Na [58] during CIGS growth, and withstands its growth conditions.

Table 5-2: Substrates, CIGS growth methods and back contact material for several CIGS companies [140].

Company	Substrate	Back Contact	CIGS Growth Process
Shell Solar (now Showa-Shell)	Glass	Mo	Sputter/Selenization
Global Solar	Steel	Mo	Co-evaporation
Miasole	Glass	Mo	Sputter/Selenization
Würth Solar	Glass	Mo	Co-evaporation
Avancis	Glass	Mo	Sputter/RTP
Daystar Tech	Glass	Mo	Sputter
EPV	Glass	Mo	Sputter/evaporation
Ascent Solar	Polymer	Mo	Co-evaporation
ISET	Glass/Flex	Mo	Ink/Selenization
Nanosolar	Flexible	Mo	Nanoink print/ RTP
Heliovolt	Glass	Mo	FASST
SoloPower	Steel	Mo	ED/RTP

One weak point that is usually acknowledged when using Mo is its low reflectance in the visible part of the spectrum. Some research groups [141] are trying to decrease the thickness of the CIGS, and their motivation is to make PV modules cheaper by using lower quantities of material. With lower thickness of the absorber layer, the amount of light absorbed in a single passage will decrease and therefore a good reflectance of light in the back contact is required. The basic idea is to increase the number of absorbed photons by reflecting those that are not absorbed in the first passage. Other metals with low resistivity and high reflectivity values, for example Pt, or Au, usually diffuse into the CIGS layer during the deposition [142]. Other reports have confirmed that cells made with Mo perform better than cells with a back contact layer with better reflectivity than the Mo one [142].

Mo is usually deposited by sputtering, mainly because this method is used in the industry and it is easy to work with. Although Mo appears to be a good material to be used as back contact, its deposition is not without problems. When depositing Mo by sputtering, the low resistivity and the high adhesion of the films are contradictory effects making it difficult to have a film with both properties maximized. The reason why this happens is usually attributed to the film stress state [143, 144]. Films that are deposited under compressive stress have low resistivity but also low adhesion. On the other hand, films that are deposited under tensile stress have good adhesion but high resistivity. To overcome this problem Scofield et al. [144] suggested the deposition of a bilayer. If one can have a first layer with good adhesion followed by a layer with good resistivity, it might be possible to have a layer in which both properties would be adequate.

Despite the fact that the properties of Mo are well known and several research groups have already been using a Mo bilayer for a long time, the clear deposition conditions of such a layer have not been reported, so far. Therefore the objective of the work presented in this chapter is not to study all the referred properties but to present suitable deposition conditions of a Mo bilayer. So, from the listed requirements laid down at the beginning of this chapter, only the study of the properties that can be changed by the deposition method will be done. The properties that are required to make suitable Mo films are: thicknesses no bigger than 1000 nm; sheet resistances lower than 1 $\Omega_{\square}$; good adhesion; being able to withstand temperatures up to 580 ºC and at the same time maintain its original properties.

5.1.2.1 Influence of the sputtering pressure

Sputtering working pressure influences the properties of sputtered atoms mainly by changing the mean free path [145, 146]. With increased pressure in the chamber, the probability of a sputtered atom colliding with an Ar atom exchanging the energy and momentum increases. The energy with which the sputtered atoms arrive at the substrate is an important factor to determine the stress state of the films. When sputtering at low pressures, Mo films have the tendency to become tightly packed, which tends to form films with a compressive stress and this leads to a decrease in its resistivity. On the other hand, when sputtering at high pressures Mo films have a more porous columnar grain growth causing intergranular voids and tend to have a tensile stress. This happens due to the reduced energy of sputtered atoms that arrive at the substrate. In terms of film properties, these voids make the resistivity higher but since there is not a reorganization of the arriving atoms, the adhesion is good. The tensile forces between these grains are attractive and inversely proportional in strength to the intergranular spacing [143]. Although these two explanations seem to be adopted by different research groups, there is an effect that is not yet fully explained. It has been reported that Mo films have a maximum value in tensile stress with increasing deposition pressure which then even turns to compressive stress. This effect is not explained by anyone, so far.

The stress state of the films is dependent on the microstructure of the Mo films which is also related with the deposition conditions. In ideal situations one would require to have the electrical behaviour of the compact films deposited at low pressures with compressive stress and the good adhesion that films with columnar grains show when they are in a tensile stress deposited at high pressures. The stress state of the films studied in this work will be estimated using the rocking curve method.

5.1.2.2 The Rocking curve characterization method

The rocking curve method is a non destructive X-ray diffraction based method that allows one to estimate the stress state of a thin film. It is a complex technique that explores the strain in a film. Let us consider that $\varepsilon_{\Phi,\psi}$ is the elastic lattice strain in a direction defined by the Euler angles Φ and ψ with respect to the specimen frame of reference, see Figure 5-1.

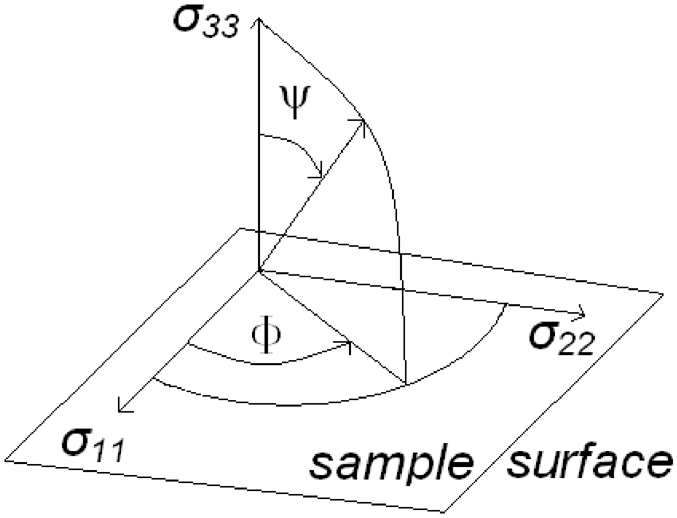

Figure 5-1: Definition of Euler angles ψ and Φ with respect to the overall stress state.

The strain depends on the components of the stress tensor σ_{ij} [$\sigma_{ij} = \sigma_{ji}$ ($i \neq j$); $\sigma_{i3}=\sigma_{3i}=0$] [143, 147] as:

$$\varepsilon_{\phi,\psi}^{hkl} = \frac{d_{\phi,\Psi}^{hkl} - d_0^{hkl}}{d_0^{hkl}} = S_1^{hkl}(\sigma_{11} + \sigma_{22}) + \frac{1}{2} S_2^{hkl} \sigma_\phi \sin^2 \psi \qquad \text{(eq 5-1)}$$

$$\sigma_\phi = \sigma_{11} \cos^2 \phi + \sigma_{12} \sin 2\phi + \sigma_{22} \sin^2 \phi \qquad \text{(eq 5-2)}$$

where ψ is the angle between the normal to the diffracting set of lattice planes (h k l) and the normal to the specimen surface, ϕ is the rotation angle within the plane of the layer (see Figure 5-1). $d_{\phi,\psi}^{hkl}$ is the lattice spacing of (h k l) planes in the direction defined by ϕ and ψ, and d_0^{hkl} is the corresponding strain-free lattice spacing of (h k l) planes. S_1^{hkl} and S_2^{hkl} are elastic constants for lattice plane (h k l). For a polycrystalline specimen with random crystallite orientation and a negligible variation of σ_{ij} over the probed depth, $\varepsilon_{\phi,\psi}^{hkl}$ depends linearly on $\sin^2\psi$.

For the case of Mo, the lattice planes used were (3 2 1). The diffraction peak is found around the 2θ range 129-137 º. For the measurement of the Mo (3 2 1) peak, a scan between 0º and 63º in the ψ direction was done. Bragg's law was used to calculate $d_{\phi,\Psi}^{321}$. The curves were fitted using a pseudo-Voigt function.

By using the slope of $d_{\phi,\Psi}^{321}$ versus $\sin^2\psi$ and eq 5-1 it is possible to estimate the value of $\frac{1}{2}S_2^{321}\sigma_\phi$. The linearization was done in the interval of 0.25 to 0.7 $\sin^2\psi$. S_2^{321} takes the value of 4.76 x 10^{-6} MPa^{-1} according to [143, 144] and therefore it is possible to calculate σ_ϕ. Although it is also possible to determine bi-axial components of the stress tensor, since these follow the general behaviour of σ_ϕ, this component is enough to evaluate the stress state of the films.

5.1.2.3 Mo film deposition and characterization

Deposition of Mo was done by DC magnetron sputtering. The Mo target purity was N4 and Ar N5 was used as the sputtering gas. Mo films were deposited on 3 × 3 cm^2 soda lime glass (SLG) substrates. The base pressure of the chamber was 5 × 10^{-6} mbar. Thicknesses were monitored with a quartz crystal monitor Intellemetrics IL 150. The working pressure in the chamber could vary in the interval between 1 x 10^{-3} mbar and 1 x 10^{-2} mbar. This was done by changing the Ar flow or by opening or closing a butterfly valve. In this study it was always used the same flow of Ar to calibrate the butterfly position at a predefined pressure. Pressure then could be changed using different Ar flow values. It was used a sputtering power density of 0.5 $\mathrm{W/cm}^2$ and the substrate-to-target distance was 10 cm.

The adhesion of the films was tested by the Scotch tape test [144]. It was considered that the Scotch tape test or adhesion test had only two results, good or bad. If after the application of the tape the film was not damaged, then the adhesion was good, otherwise it was considered bad.

The four point probe method was used to measure the sheet resistance, ρ_S, of the films. Knowing the sheet resistance and the thickness, h, of the films it is possible to estimate the resistivity, ρ, using the following equation valid for square uniform samples:

$$\rho = h \cdot \rho_s \qquad \text{(eq 5-3)}$$

5.1.2.4 Results

5.1.2.4.1 Mo single layer films

Single layer Mo films were initially deposited to test the different regimes described by Scofield et al. [144] and the reproducibility of such conditions in the chamber was analysed. In Table 5-3 the results of the first experiments are given. For this set of experiments the main purpose was to identify the changes in adhesion and resistivity as function of the working pressure. Table 5-3 shows the same tendency that has been reported by Scofield et al. [144] for all properties. Films sputtered at high pressure have good adhesion and poor resistivity and films at lower pressure have the opposite properties. In Figure 5-2 it is possible to see the resistivity as function of the pressure. The results follow the same tendency as shown in previous studies [143, 144].

Table 5-3: Properties of single layer Mo films.

Pressure (mbar)	**Adhesion**	**Resistivity (µΩ.cm)**
10×10^{-3}	Good	411.0
6×10^{-3}	Good	330.4
4×10^{-3}	Bad	82.7
1×10^{-3}	Bad	36.3

From these results it is evident that there are two regimes when depositing Mo. The first regime, at pressures between 6×10^{-3} and 10×10^{-3} mbar, produces samples with good adhesion but with high resistivity. In the second regime, at pressures between 4×10^{-3} and 1×10^{-3} mbar, the samples have bad adhesion but lower resistivity.

This analysis demonstrates which regime one can use to deposit a Mo bilayer. The first layer should be deposited at a pressure higher than 6 x 10^{-3} mbar to ensure good adhesion and the second at a pressure lower than 4 x 10^{-3} mbar to obtain a low resistivity.

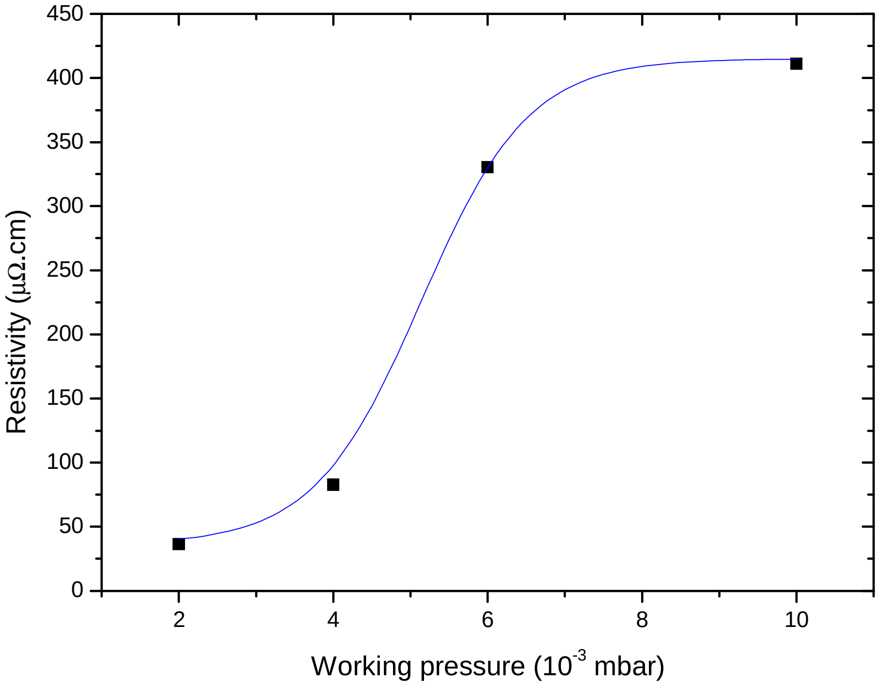

Figure 5-2: Mo single layer resistivity versus working pressure.

5.1.2.4.2 *Mo bilayer films*

For this test it was decided to deposit a layer at high pressure at the bottom followed by a layer at low pressure at the top. It was decided to make the bottom layer 500 nm thick and to study the effect of varying the thickness of the top layer on the properties. The pressures chosen were 10 x 10^{-3} mbar for the bottom layer and 4 x 10^{-3} mbar for the top layer. Between the two different pressures there is a period of 2 minutes. During this time the pressure was lowered in 1 minute and the tooling factor of the thickness quartz crystal monitor was changed in the other minute. Since this is not automatic, these transitions may vary slightly from film to film and can result in different final thicknesses of the films.

By looking at the properties presented in Table 5-4 it can be seen that when the top layer is thin, then the film properties are close to those of the single layer samples deposited at high pressure. In the other extreme case, where the top layer is as thick as the bottom layer, the film has bad adhesion and the lowest resistivity. The best sample of this batch had a 500 nm thick bottom layer and the top layer was 300 nm thick. For the top layer of 400 nm there was poor adhesion and so continuing to increase the thickness of the top layer was useless. The value of 1.8 $\Omega_{\square}$ for the sheet resistance is not low enough and therefore the deposition pressure of the top layer was further decreased.

Table 5-4: Description of the Mo bilayer process with 10 x 10^{-3}/4 x 10^{-3} mbar.

Sample	Step	Pressure (mbar)	Quartz Monitor Thickness (nm)	Total measured thickness (nm)	Adhesion	ρ_s ($\Omega_{\square}$)	ρ ($\mu\Omega$.cm)
1	1	10 x 10^{-3}	500	685	Good	4.5	307.68
	2	4 x 10^{-3}	200				
2	1	10 x 10^{-3}	500	808	Good	2.4	194.07
	2	4 x 10^{-3}	300				
3	1	10 x 10^{-3}	500	911	Bad	1.8	163.98
	2	4 x 10^{-3}	400				

In Table 5-5 the properties of the Mo bilayer films with the top layer deposited at 1 x 10^{-3} mbar are presented. Four top layers with thicknesses, 50 nm, 200 nm, 300 nm and 450 nm were deposited. This time with increasing thickness of the top layer no noticeable degradation in the adhesion was observed. In the case in which the top layer was 450 nm thick it was noticed a degradation in the value of the resistivity as shown in Figure 5-3. This was attributed to a poorer adhesion but since the tape test only dictates a fail or pass evaluation, the degree of adhesion is not quantified. If the adhesion of a film is degraded, then the morphology of the film is also degraded and consequently the resistivity increases.

Sample number 3 presented the lowest resistivity and had good adhesion. This sample showed a sheet resistance of 0.6 $\Omega_{\square}$ with a total thickness of 817 nm which corresponds to a resistivity of 49.1 $\mu\Omega$.cm. This value of resistivity is very close to that of a Mo single layer deposited at 1 x 10^{-3} mbar. There are some differences between the monitored thicknesses and the ones measured with the profiler but these differences are small and acceptable. This value is in accordance with values reported in other works [138, 148].

Table 5-5: Parameters and results of the bilayer deposition with 10 x 10^{-3}/1 x 10^{-3} mbar pressures.

Sample	Step	Pressure (mbar)	Controller Thickness (nm)	Adhesion	Total measured thickness (nm)	ρ_s ($\Omega_\square$)	ρ ($\mu\Omega$.cm)
1	1	10 x 10^{-3}	500	Good	567	1.6	90.7
	2	1 x 10^{-3}	50				
2	1	10 x 10^{-3}	500	Good	717	0.8	57.4
	2	1 x 10^{-3}	200				
F3	1	10 x 10^{-3}	500	Good	817	0.6	49.1
	2	1 x 10^{-3}	300				
4	1	10 x 10^{-3}	500	Good	972	0.8	77.8
	2	1 x 10^{-3}	450				

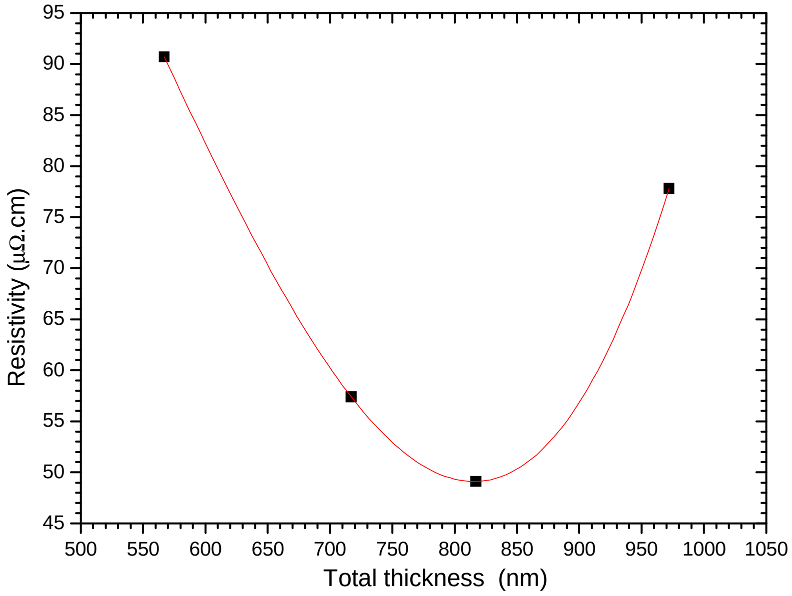

Figure 5-3: Resistivity versus total thickness for Mo bilayer samples deposited with a bottom layer of 500 nm deposited at 10 x 10^{-3} mbar and different top layers deposited at 1 x 10^{-3} mbar.

Since it was shown that for these pressure ranges the lowest achievable resistivity was 49.1 µΩcm for the sample with thickness 500+300 nm at 10 x 10^{-3} /1 x 10^{-3} mbar, it was decided to study further samples deposited in these conditions.

5.1.2.4.3 Characterization of the Mo bilayer films

An important question that had arisen from the last test was the reproducibility. Given that there was a difference between the quartz crystal monitor values and the measured thickness values it was important to check whether this error was systematic or random. To investigate this problem several samples were deposited. This was done for more than 4 runs, each with 4 films. It was then noticed that all the films had good adhesion. Their thicknesses were between 800 and 900 nm and the sheet resistance values ranged between 0.5 and 0.8 $\Omega_{\square}$. These differences were most likely due to the pressure transition time between the bottom and top layers. This transition was done manually and therefore variations may exist from sample to sample.

To ensure that the film could resist the growth temperature of CIGS, one of the samples was placed in the deposition chamber and heated up to 580 ºC for one hour. The Mo film was able to sustain these high temperatures without degradation of its properties.

The XRD diffractogram presented in Figure 5-4 shows the typical cubic Mo structure with the following visible peaks: (1 1 0) planes with a peak at 40.46 º, with d_{110} = 2.22 Å and a peak at 73.75 º which corresponds to the (2 2 1) planes with d_{221} = 1.28 Å. The peaks of the (2 2 0) planes at 87 º and (3 1 0) at 101 º are very weak. The lattice parameter, *a*, was estimated to be 3.13 Å against the 3.14 Å predicted by the XRD database [100]. This variation is smaller than 0.32% and it is within the measurement errors.

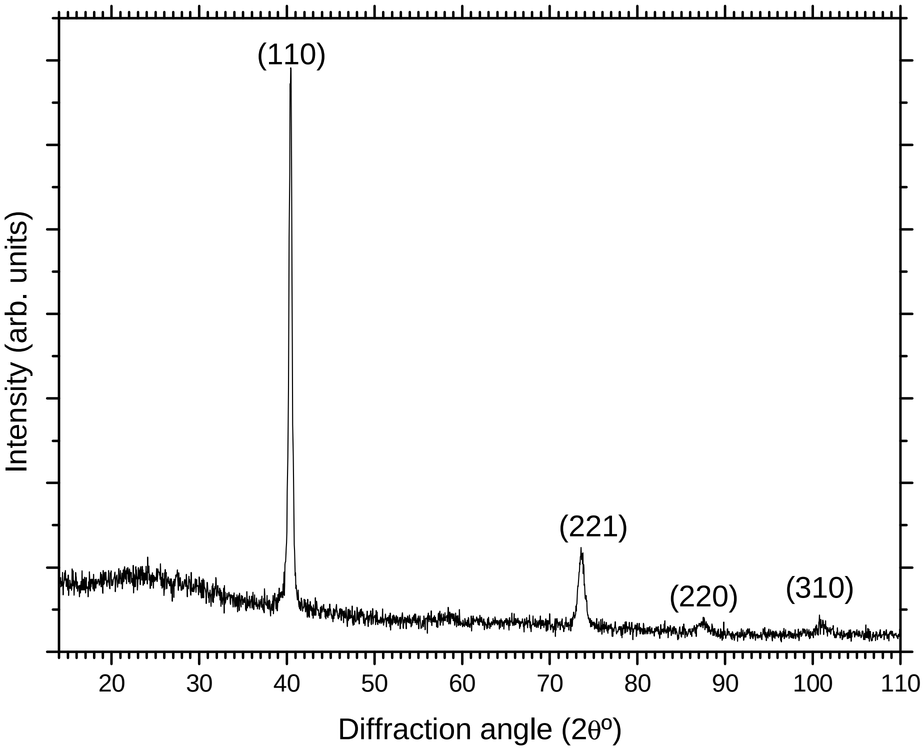

Figure 5-4: XRD diffractogram of a Mo bilayer film.

The stress calculations were made for a Mo bilayer film. In Figure 5-5 a) it is presented the pseudo-Voigt fit for a XRD measurement with ψ = 35.84°. In Figure 5-5 b) it is plotted $d_{\phi,\Psi}^{321}$ versus the $sin^2\psi$. Calculations of the stress tensor, σ_ϕ, were made as previously explained.

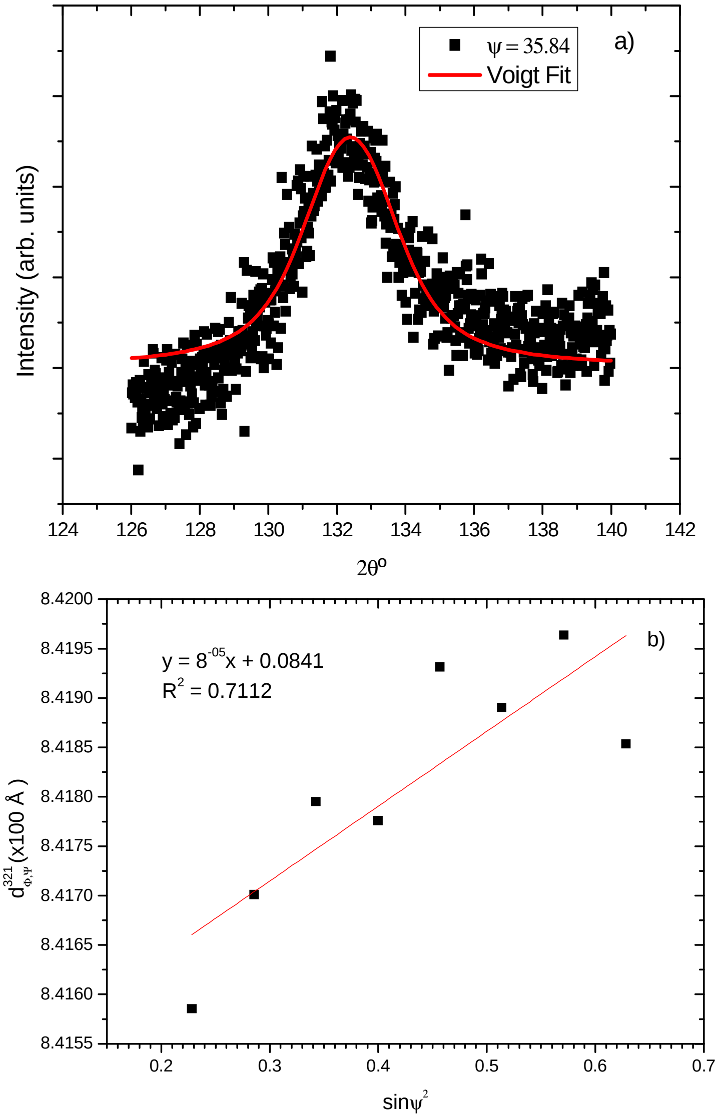

Figure 5-5: a) Example of Voigt fitting for ψ = 35.84 °; b) the lattice spacing for the planes (3 2 1) versus sin^{2}ψ for a Mo bilayer film.

As shown in Figure 5-5 not only the correlation between the points is low, but the slope of the curve is also low. Although R^2, the variation coefficient is 0.7, R, the correlation coefficient is 0.83 which indicates that there is a general tendency for higher values of $d_{\phi,\Psi}^{321}$ with the increase of $\sin^2\psi$. This means that the film is in a tensile state. The result of the stress tensor component, σ_ϕ, is 17 MPa, which is a low value. For comparison purposes, the values found by Vink et al. [143] were in the order of magnitude of GPa. This difference is possibly due to the fact that the film has relaxed due to its thickness, but it is also possible that this is a mean value for a film with the top half in a compressive state and the bottom half in a tensile state. Nevertheless the important film properties had the desirable values.

In Figure 5-6, a SEM image of the cross section of a Mo bilayer is presented. The film shows a columnar growth and it is possible to see the bottom layer with 500nm and the top layer with 300 nm.

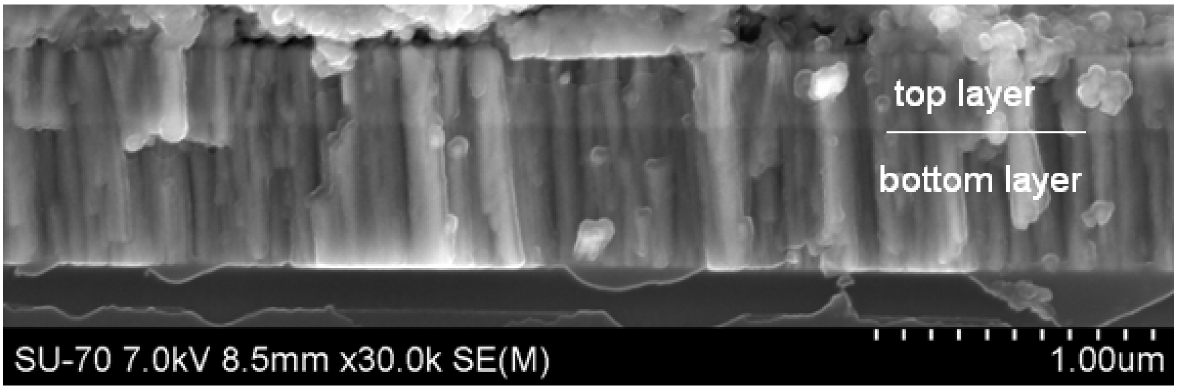

Figure 5-6: SEM image of the cross section of a Mo bilayer.

The main goal of the study reported in this section was to clearly identify the deposition conditions, missing in the literature, which ensured the deposition of Mo bilayers with good adhesion to the SLG, a sheet resistivity lower than 1 $\Omega_\square$ and good reproducibility of the former two properties.

In summary the results of the study where the effects of varying pressure and thickness of the top layer on the properties of a Mo bilayer were presented. A detailed study of the resulting Mo bilayers was made, and the optimal result was achieved when the bottom layer was deposited at 10 x 10^{-3} mbar with a thickness of 500 nm and the top layer deposited at 1 x 10^{-3} mbar with a thickness of 300 nm. The Mo bilayers produced by this method meet the desired properties by having a good adhesion and a sheet resistivity between 0.5 and 0.8 $\Omega\square$.

The resulting Mo bilayers were analysed and XRD studies showed a film with the typical Mo cubic structure and a crystallite size of 40 nm. Stress calculations gave evidence that these films were in a low tensile state. These calculations were difficult to make due to the large dispersion of the data when analysing the rocking curves themselves. The method proved to be reproducible and the films could withstand the harsh growth conditions of CIGS.

5.1.3 CdS buffer layer

Cadmium sulphide, CdS, is one of the most used semiconductors in thin film PV applications since it is used in CIGS and CdTe solar cells, both in laboratory and in industry applications. In those two types of solar cells, CdS has the same function which is being the n-type semiconductor in the p-n heterojunction.

This compound is part of the II-VI family and has a direct band gap energy of 2.42 eV at room temperature [149]. CdS forms in two possible crystal structures, wurzite and zinc blend. CdS is an n-type semiconductor where the conductivity comes from the excess of Cd in the lattice. The vacancies of S and the interstitial defects of Cd are both donor defects [149].

Another property of CdS that is useful for a better functioning of the solar cell is its refractive index [150]. This value is intermediate between the value of ZnO and CIGS, as it can be seen in Figure 5-7 and therefore reflection is minimized.

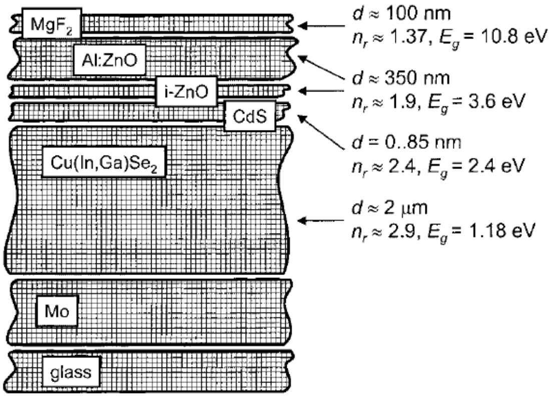

Figure 5-7: Solar cell structure showing the thickness, the refractive index and the band gap energy for each layer according to Orgassa et al. [150].

Although CdS has interesting properties for solar cells, efforts are being made to replace this material since there is a big concern about the toxicity and environmental hazards of cadmium [151]. Placing the environmental concerns apart, there is also hope that the replacement of this compound for another with higher band gap energy can bring superior values of short circuit currents. Examples of studied materials to replace CdS are ZnS and $Zn_xM_{1-x}gO$, a good review of some materials that could replace CdS is done by Naghavi et al. [152]. A vast number of compounds could, theoretically, replace CdS as the buffer layer, but the best CIGS and CZT(S,Se) solar cells are made with CdS. The exact reason why this occurs is not understood but some studies suggest that during the CBD there is a passivation of the CIGS surface [153], enhancing this way the electronic properties of the absorber.

This layer is usually deposited using chemical processes and brings additional concerns since all the other growth techniques are vacuum based. The breaching of vacuum brings extra costs and may lead to the contamination of the important interface between the absorber and the CdS.

5.1.3.1 Chemical bath deposition

There are several techniques for depositing CdS, among them, the most used and with the best results is the chemical bath deposition (CBD). This method is easy, cheap and quite reproducible. As mentioned before, it is not done in vacuum and this is in fact a problem since all the other depositions are vacuum based. The main concern of this process is the residues of Cd and ammonia which are hazardous for the environment.

The interface between CIGS and CdS is still today the object of controversy. Some authors argue that there is a diffusion of Cd into the surface of the CIGS layer and that dopes the layer n-type leading to the formation of a homojunction instead of a heterojunction [48, 54, 150]. Another factor that influences the behaviour of the CIGS/CdS junction is the existence of Na coming from the substrate [50, 58]. This is something difficult to evaluate since during the bath Na can be cleaned from the surface [58].

There are many reports where the thickness of CdS is studied but the optimum thickness is usually considered to be between 40 and 60 nm [149-151]. In this range of

CdS thicknesses the combined effect of the electronic losses and the optical gain, result in the most efficient CIGS solar cells. The structure of the films deposited by this method is usually a mixture of phases with the wurzite and the zinc blend structure [150].

The usual composition of the bath is:

- $Cd(CH_3COO)_2$ (cadmium acetate) in a concentration of 0.03M;
- $CS(NH_2)_2$ (thiourea) in a concentration of 0.6M;
- NH_4OH (25%) (ammonium hydroxide) in a concentration of 7.14M.

In this recipe, cadmium acetate is used as the Cd source, the ammonium hydroxide is the complexing agent and thiourea is the source of S. The deposition of the CdS films occurs by condensation of Cd and S ions on the surface of the film, or by adsorption of colloidal CdS particles in suspension [149].

The chemical reaction that occurs in this deposition is the following [149]:

$$Cd(NH_3)_4^{2+} + CS(NH_2)_2 + 2OH^- \rightarrow CdS + CH_2N_2 + 4NH_3 + 2H_2O \qquad \text{(eq 5-4)}$$

For this reaction, a buffer solution can be added in order to control its pH by assuring that the quantity of OH^- is constant. Usually ammonium acetate, $CH_3CO_2NH_4$ is used. That procedure was not performed during this thesis. For more information on this reaction, see reference [149].

For one deposition, the following quantities are used:

- 200ml of deionised H_2O (18MΩcm);
- 15ml cadmium acetate solution, $Cd(CH_3COO)_2$;
- 10ml of thiourea solution, $CS(NH_2)_2$;
- 25ml of ammonium hydroxide, NH_4OH.

The solutions are added in the following order: H_2O; cadmium acetate; thiourea; and finally ammonium hydroxide.

The deposition starts when the samples are dipped into the hot bath and the timing starts when thiourea is added to the solution. The bath is kept at a temperature between 65 ºC and 70 ºC. This variation is due to the immersion of the sample holder. The deposition takes between 15 to 18 minutes and is controlled by the colour of the solution. Although the control relies on visual perception, the results are quite reproducible. As soon as the deposition ends, the samples are removed and cleaned with H_2O and dried with a flow of N_2. The utensils are cleaned with a solution of 10% HCl.

The control of the bath's temperature is of crucial importance since it is responsible for the speed and quality of the deposition. In this thesis, CdS films grown at different temperatures were deposited. In Table 5-6 the properties of films deposited at different temperatures are presented and were in good agreement with other works [154].

Table 5-6: Effects of temperature in the CBD of CdS adapted from [154]. The lowest temperature,*, was not tested in this thesis and was taken from [154].

Temperature of the bath (°C)	Rate	Quality
Up to 55*	slow	surface not uniform
From 55 to 70	moderate	good
above 70	fast	rough and with poor adhesion

5.1.3.2 Properties of the CdS film

In Figure 5-8, the transmittance of a CdS film deposited by CBD is shown. The figure depicts a transmission higher than 80% for wavelengths values higher than 580 nm. The band gap value of CdS is around 2.4 eV or about 530 nm. In order to estimate precisely this value, reflection measurements would be required as well. However this was not the objective and with just these measurements it is possible to say that there is a transition near 550 nm which should be due to the band gap absorption.

The diffraction pattern of a CdS film deposited on SLG by CBD is illustrated in Figure 5-9. The green lines show where the peaks for the CdS with the zinc blend structure should be. This pattern points out that the film has the zinc blend structure, but to verify this statement because the layer is thin, a grazing incident measurement would be needed.

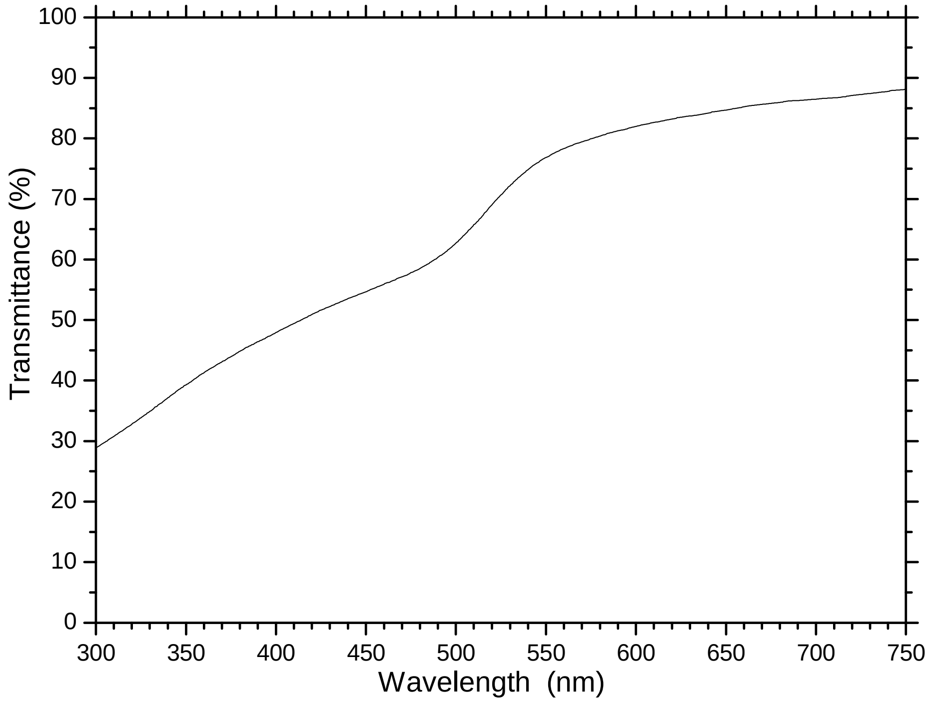

Figure 5-8: Transmittance of a CdS film deposited on SLG by CBD.

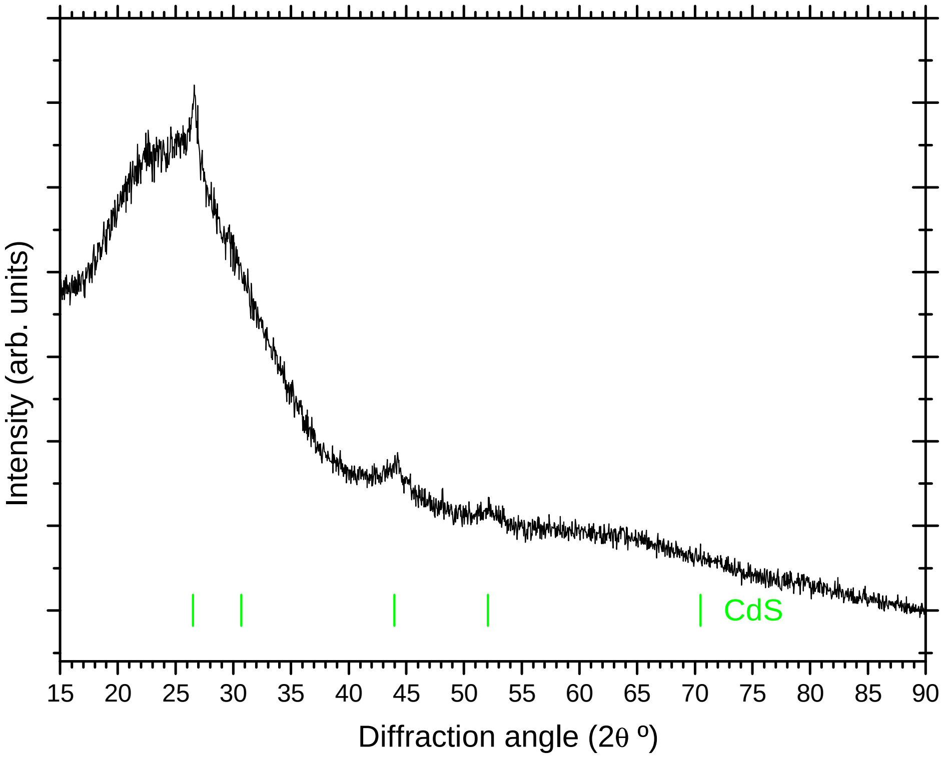

Figure 5-9: XRD diffractogram of a CdS film deposited by CdS.

5.1.4 The cell window layer

The role of this layer is as the name indicates to allow light to be transmitted and at the same time allow the collection of photogenerated charge carriers. Typically, in the best CIGS solar cells and in industrial systems, a bilayer of i-ZnO and ZnO:Al is used [40, 41]. Supposedly, the intrinsic layer of ZnO is able to stop some short circuits between the two electrodes because of its high resistivity and low roughness [155]. The Al doped ZnO is conductive and therefore capable of collecting the free electrons [156]. The research group in Aveiro instead of using the ZnO bilayer uses a single layer of $In_2O_{3:}SnO_2$, indium tin oxide, ITO. Previous results demonstrate that solar cells with only this layer do not perform as well as the ones with the ZnO-bilayer but perform well enough to evaluate the solar cells performances [157].

The ITO window layers were deposited by DC-sputtering in a system without load-lock. A 3-inch ITO target (10 wt% SnO_2) was used for the deposition. The base pressure of the vacuum system was 4.2 x 10^{-6} mbar. ITO sputtering was done in pure Ar or Ar/O_2 (1.5 vol.% O_2) gas atmosphere at a working pressure of 10^{-2} mbar with DC power density varied from 0.8 W/cm^2 up to 1.8 W/cm^2. The deposition time for the optimized process conditions lasted about 5 min and produced 300 nm thick films. Since the chamber did not have a load lock system, when the chamber was opened the target was exposed to air and its oxidation state changed, varying as well the conditions of the next depositions. So the ITO deposition usually took several runs to optimize. It is well known that the amount of oxygen in the film changes significantly both the optical and electrical properties of the films [158, 159].

Films with a thickness of 300 nm and with values of sheet resistance of 100 $\Omega_\square$ or lower were used in the solar cells. In the latest cells the production base line of solar cells of the HZB was used instead.

All the CIGS solar cells were made with the ITO window layer. CZTSe solar cells were made at the HZB in Berlin and their baseline was used, hence they have a ZnO window layer. In the case of the CZTSSe solar cells, a ZnO:Ga window layer, deposited at CINEMAT in Lisbon, was used. A good overview of the properties of some TCOs can be seen in the review paper written by Granqvist [160].

5.2 Solar cell results

Several solar cells were prepared during this thesis most of them were from CIGS since at that time it was possible to prepare the whole solar cell in Aveiro. With the degradation of the ITO target, a fast preparation of CZTSe solar cells could not be done. The results for the best cells of each material are presented in Table 5-7.

Table 5-7: Solar cell results.

Sample	V_{oc} [mV]	j_{sc} [mA/cm²]	FF [%]	η [%]
CIGS sample 1	535	21.0	66.8	7.4
CZTSe_2009_12_04	85	2.5	25.0	0.1
CZTSe_2010_02_17	65	4.6	25.0	0.1
CZTSSe ZTC S	207	13.9	31.4	0.9

For the best CIGS solar cell the absorber was grown using the hybrid system where Ga was evaporated. The film properties were discussed previously in section 4.1.1. The best solar cell had an efficiency of 7.4% with a V_{OC} of 535 mV, a J_{SC} of 21 mA/cm² and a fill factor of 66.8 %. The j-V curve is shown in Figure 5-10. This efficiency value is very close to that of the best cell obtained by the research group at Aveiro, around 8% using pellets of Ga-Se on top of the In and Cu sputtering targets. However, a solar cell with a conversion efficiency of only 7.4% represents a weak value when compared with the best cells that reach values as high as 20%. The reason why the cells do not have such high values can be explained by several factors, from which the strongest is the lack of a base line procedure for solar cell production. Not only the other layers are not fully optimized but the processes themselves are not mature enough to obtain good results, for instance the minimization of the exposure of the absorbers to air, the use of materials as pure as possible or even simple things such as the handling.

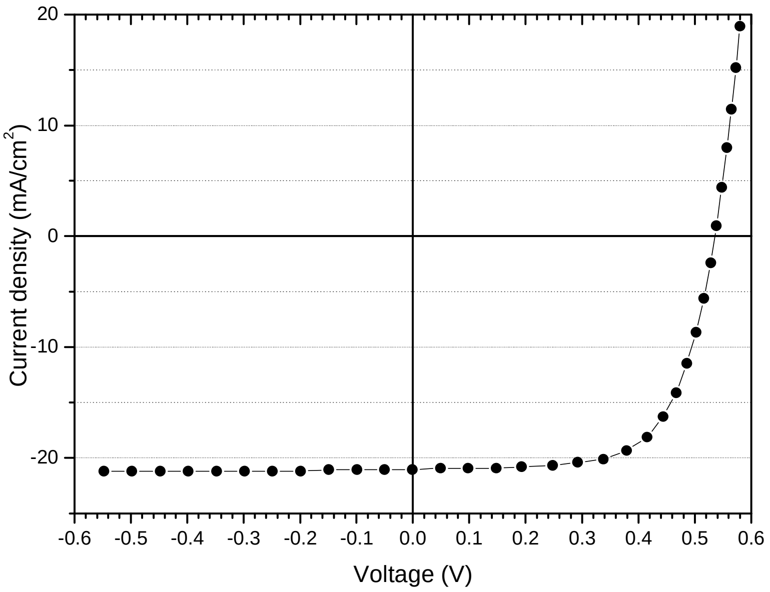

Figure 5-10: j-V curve of the best CIGS solar cell.

For CZTSe solar cells, the results were weaker with most of the cells not showing any photovoltaic effect and the ones that indicated that effect had extremely poor values with efficiencies of 0.1 %, see Figure 5-11. The reason why this happened can be mostly attributed to the poor adhesion of the CZTSe films to the Mo. When they were submitted to the KCN etching, most demonstrated poor adhesion because some peeled off and visible pin-holes were detected in the films which affected the efficiency of the cells. Also, the absorbers were sent to the HZB, in Berlin, without the CdS layer which is known to protect the absorbers from exposure to air. During the transportation the films may have suffered some degradation both of the electrical properties by exposure to air and by damage to the surface. By comparison, one can look at the CZTS solar cells whose absorber was also prepared in Aveiro and were sent to Berlin to be finished into cells. Those films showed a much better adhesion and the solar cell properties are better, although not great. The maximum solar cell efficiency obtained was around 1.2 % [v].

The CZTSSe based solar cell showed somewhat better values with the best having an efficiency of 0.9 %, 207 mV and 13.9 mA.cm^{-2}, the j-V curve is depicted in Figure 5-11. The mix of S and Se improved the solar cell performance since the efficiency value is better than for the best CZTSe solar cell but still lower than the best CZTS solar cell.

Despite this fact, only one solar cell of this material was prepared and more would be needed to draw definitive conclusions.

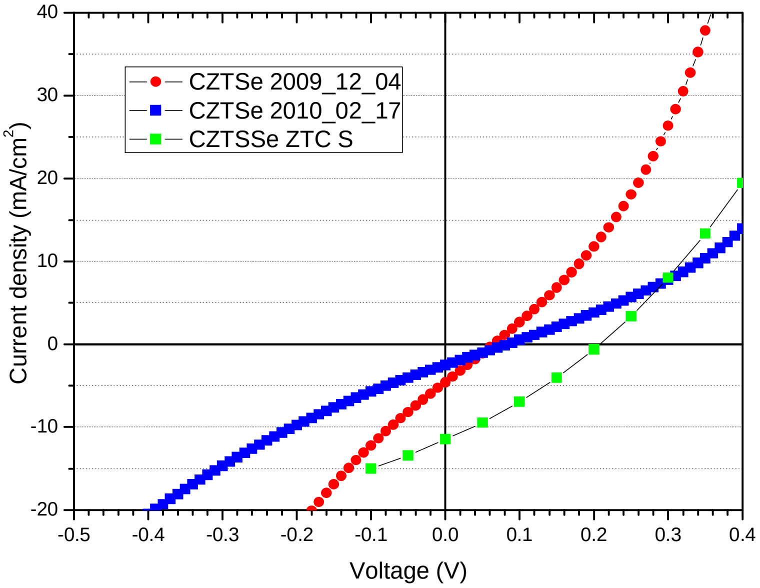

Figure 5-11: j-V curve of CZTSe and CZTSSe solar cells

6 Conclusions

In this thesis, three different studies were carried out. The first was the study of different processes for incorporation of Ga in CIGS thin films grown by the hybrid system. The second was the establishment of suitable growth conditions of CZTSe and its characterization. The final stage of the work consisted of preliminary studies on the growth of CZTSSe by incorporating Se in CZTS and CTS films.

In the Ga incorporation studies, one of the tests conducted using a target of Ga was not successful due to the low melting point of Ga and the high surface tension of liquid Ga that created drops at the target holder. In the test with evaporation of Ga, the growth of CIGS was made with a 2-step Cu-rich to Cu-poor transition. A reproducible process for the growth CIGS films with the desired composition was successfully implemented. Although the film presented an open structure, this unwanted morphology did not cause shunts in the cells and the maximum efficiency obtained was around 7 %. This efficiency is in the same range as previous cells made in Aveiro. The results show that evaporating Ga can be a possible process to be installed in hybrid sputtering and evaporation growth systems. The use of a CuGa sputtering target gave results of low quality since in this case most of Ga concentrated at the back of the films. The morphology of the films was poor and the reproducibility was low hence no solar cells were prepared. The CuGa targets are usually used for growing GIGS by selenization of precursors which is a different method from the one used here, so the extrapolation of the results was not successful.

The thermodynamic conditions for the growth of CZTSe were fully studied. It was noticed that for substrate temperatures lower than 500 ºC the diffusion of Se is not good enough. Another problem that arose was that at pressures lower than 1 mbar, there are losses of Zn and Sn by evaporation due to the vapour pressure at that temperature for elemental Zn and SnSe. Two different methods were implemented to grow single phased CZTSe, the first was to perform the selenization of precursors at 10^{-5} mbar with excess of Zn and Sn to compensate for the losses; and the second one was the selenization of precursors done at 1 mbar. In both cases a KCN etching was needed to remove $Cu_{2-x}Se$ phases even for final Cu-poor films. The second option was better since it avoided the unnecessary loss of material and the control of the composition only depended on the composition of the precursors. The properties of single phase CZTSe films were thoroughly studied. The characteristics found are the following: the band gap energy was estimated to be around 1.05 eV, it was observed a PL emission around 0.935 eV at room temperature, the Raman scattering peaks were fully assigned and there is evidence that the crystalline structure of the films is kesterite. Despite the encountered problems, a recipe to prepare single phase CZTSe was achieved and this paved the way to understand and refine the properties of this material.

Regarding the CZTSSe films, the study reveals that films with CTS or CZTS formed before the selenization are less homogenous than the ones where the precursors are stacked metal sulphides. Due to the XRD impossibility to distinguish Zn(S,Se) from CZT(S,Se) and the wavelength limited depth analysis of Raman scattering, conducting the analysis of the crystalline structure of such films revealed to be quite difficult.

6.1 Suggestions for further work

The performance of CIGS based solar cells was poor when compared with the actual world records. It would be important to have better conditions for the preparation of the cells in order to verify if the actual limitation is coming from the material or rather from the process of preparing the cells. For this, a clean room, less air exposure time to mainly the Mo films and the absorbers and the local capability to prepare TCOs would all be major improvements for the preparation of solar cells. With regards to the material properties, in the evaporation of Ga an improvement of the morphology of the films would be needed. The resulting open structure with relatively small grains is not desired and a study of the influence of the grain boundaries would be important to understand how this is limiting the cells' performance.

The solar cell performance of both CZTSe and CZTSSe was quite poor. In the case of CZTSe, adhesion of the films is still a problem and possible solutions for this problem would be: make slower heating and cooling profiles given that the thermal expansion coefficient of the absorber is unknown; deposit the mixed precursors instead of stacked for a better mixture in order to avoid secondary phases due to non uniformity; increase the control of the precursors composition and test other gases to increase the pressure during the selenization for replacement of Ar like, for instance, N. The most important studies that now can be done are electrical ones. It is rather important to understand CZTSe electrical properties to assess if this material is really suitable for solar cells and its major limitations, since being a p-type semiconductor with a high absorption coefficient is not enough. Carriers' concentrations, carriers' mobility, position of Fermi levels, electronic affinity, influence of Na, influence of defects, and some other parameters are important and should be measured. Other studies that should be done as well are structural ones. In the case of CIGS, having more or less replacement of Ga per In is not a problem since the structure will be the same, but in the case of making Zn-rich CZTSe films, where is the excess of Zn going? The direct replacement of Zn per Sn is not straightforward and for this a better knowledge of the structure and of the physics of the defects of the material is needed.

References[6]

[1] M.K. Hubbert, *Nuclear Energy and the Fossil Fuels*, Presented before the Spring Meeting of the Southern District, American Petroleum Institute, Plaza Hotel, San Antonio, Texas, March 7–8-9, 1956.

[2] Nathan S. Lewis, George Crabtree, Michael R. Wasielewski, Paul Alivisatos, Harriet Kung, *Basic research needs for solar energy utilization*, U.S. Department of Energy, September 2005.

[3] Jenny Nelson, *The physics of solar cells*, Imperial College Press, 2002.

[4] M.A. Green, *Photovoltaics: technology overview*, Energy Policy 28 (2000) 989-998.

[5] L. L. Kazmerski, *Solar photovoltaics R&D at the tipping point: A 2005 technology overview*, Journal of Electron Spectroscopy and Related Phenomena 150 (2006) 105–135.

[6] Science, Technology & Applications Working Group, *A Strategic Research Agenda for Photovoltaic Solar Energy Technology*, European Communities, 2007.

[7] A. Zahedi, *Solar photovoltaic (PV) energy; latest development in the building integrated and hybrid PV systems*; Renewable Energy 31 (2006) 711–718.

[8] QCells Factbook August 2009, *Hand on QCells Handbook for investors and analysts*, Q-Cells, August 2009.

[9] Arnulf Jäger-Waldau, *PV Status Report 2008*, European Commission Joint Research Center Institute for Energy, EUR 23604 EN – 2008.

[10] D.A. Cusano, *CdTe solar cells and photovoltaic heterojunctions in II–VI compounds*, Sol. State Electron. 6 (1963) pp. 217.

[11] Dietrich A. Jenny and Richard H. Bube, *Semiconducting Cadmium Telluride*, Phys. Rev. 96, 1190–1191 (1954).

[12] R. H. Bube, *Photoconductivity of the Sulfide, Selenide, and Telluride of Zinc or Cadmium*, Proceedings of the IRE, pp. 1836-1850, 1955.

---

[6] The style of the references is the same as in the original papers, therefore different citing styles are present but finding the papers is much easier. When not published but yet on-line versions were accessible at the time of the writing, the corresponding DOI is indicated instead of volume and page number.

[13] K. L. Chopra, P. D. Paulson and V. Dutta, *Thin-Film Solar Cells: An Overview*, Prog. Photovolt: Res. Appl. 2004; 12:69–92.

[14] Martin A. Green, Keith Emery, Yoshihiro Hishikaw and Wilhelm Warta, *Solar cell efficiency tables (version 36)*, Prog. Photovolt: Res. Appl. 2010;DOI:10.1002/pip.1021.

[15] ZSW press release 11/2010, *New world record with efficient CIGS solar cell, Zentrum für Sonnenenergieund* Wasserstoff-Forschung Baden-Württemberg (ZSW) Stuttgart, Germany, 23 August 2010.

[16] Joyce Laird, *PV innovations: Thin-film technology update*, Renewable Energy Focus, Elsevier, 16 August 2010.

[17] Jörg Palm, Volker Probst, Franz H. Karg, *Second generation CIS solar modules*, Solar Energy 77 (2004) 757–765.

[18] Sigurd Wagner, J. L. Shay, P. Migliorato, and H. M. Kasper, *$CuInSe_2$/CdS heterojunction photovoltaic detectors*, Appl. Phys. Lett. 25, 434 (1974).

[19] ZSW Press release 5/2010, *ZSW produces a thin-film solar cell with 20.1 percent efficiency*, Zentrum für Sonnenenergie und Wasserstoff-Forschung Baden-Württemberg (ZSW), Stuttgart, Germany, 28. April 2010.

[20] R. R. Potter, C. Eberspacher, and L. B .Fabick, *Device analysis of $CuInSe_2$/(Cd,Zn)S/ZnO solar cells*, in Proceedings of the Conference Record of the 18th IEEE Photovoltaic Specialists Conference, pp. 1659–1664, 1985.

[21] Martin A. Green, *Estimates of Te and In Prices from Direct Mining of Known Ores*, Prog. Photovolt: Res. Appl. 2009; 17:347–359.

[22] H. Katagiri, N. Ishigaki, T. Ishida and K. Saioto, *Characterization of Cu_2ZnSnS_4 thin films prepared by vapor phase sulfurization*, Jpn. J. Appl. Phys. Vol 40(2001) pp. 500-504.

[23] Jonathan J. Scragg, Philip J. Dale, Laurence M. Peter, Guillaume Zoppi, and Ian Forbes, *New routes to sustainable photovoltaics: evaluation of Cu_2ZnSnS_4 as an alternative absorber material*, phys. stat. sol. (b) 245, No. 9, 1772–1778 (2008) / DOI 10.1002/pssb.200879539.

[24] Björn-Arvid Schubert, Immo Michael Kötschau, Sonja Cinque, Hans-Werner Schock, Georg Meran, *An economic approach to evaluate the range of coverage of indium and its impact on indium based thin-film solar cells – recent results of Cu_2ZnSnS_4 (CZTS), based solar cells*, 23rd European photovoltaic solar energy conference, 1-5 September 2008, Valencia Spain.

[25] Kentaro Ito and Tatsuo Nakazawa, *Electrical and optical properties of stannite-type quaternary semiconductor thin films*, Japanese Journal of Applied physics, Vol 21, N°, 11, November 1988, pp. 2094-2097.

[26] Hironori Katagiri, Nobuyuki Sasaguchi, Shima Hando, Suguru Hoshino, Jiro Ohashi, Takaharu Yokota, *Preparation and evaluation of Cu_2ZnSnS_4 thin films by sulfurization of E-B evaporated precursors,* Solar Energy Materials and Solar Cells 49 (1997) 407-414.

[27] Hironori Katagiri, Masato Nishimura, Takeshi Onozawa, Shinichi Maruyama, Masato Fujita, Toshiyuki Sega and Taku Watanabe, *Rare-Metal Free Thin Film Solar Cell*, IEEE PCC-Nagaoka 1997, Page(s): 1003 - 1006 vol.2.

[28] T. A. M. Friedlmeier, *Multinary Compounds and Alloys for Thin-Film Solar Cells: Cu_2ZnSnS_4 and Cu(InGa,)$(S,Se)_2$*, PhD dissertation Thesis, University of Stuttgart (2001).

[29] William Shockley and Hans J. Queisser, *Detailed Balance Limit of Efficiency of p-n Junction Solar Cells*, Journal of Applied Physics, Vol 32, n3, 1961, pp 510-519.

[30] S. M. Sze, K. N. G. Kwok, *Physics of Semiconductor Devices,* Third Edition, Wiley-InterScience, 2007, New Jersey.

[31] J. E. Jaffe and Alex Zunger, *Electronic structure of the ternary chacopyrite semuconductors, $CuAlS_2$, $CuGaS_2$, $CuInS_2$, $CuAlSe_2$, $CuGaSe_2$, and $CuInSe_2$*, Physical review B, volume 28, number 10, 15 November 1983.

[32] O. Lundberg, M. Edoff, L. Stolt, *The effect of Ga-grading in CIGS thin film solar cells*, Thin Solid Films 480–481 (2005) 520–525.

[33] Cynthia Jensen, Dale Tarrant, James Ermer, Gary Pollock, *The role of Gallium in $CuInSe_2$ solar cells fabricated by a two-stage method*, Photovoltaic specialists conference, IEEE Photovoltaic Specialists Conference, 1993, Page(s): 577 – 580.

[34] R.J. Matson, M.A. Contreras, J.R. Tuttle, A.B. Swartzlander*; Effects of the concentration of Ga on junction formation in thin film ZnO/CdS/$CuIn_xGa_{1-x}Se_2$/Mo photovoltaic devices*; Mat. Res. Soc. Symp. Proc. Vol. 426, 1996.

[35] T. Dullweber, G. Hanna, U. Rau, H.W. Schock, *A new approach to high-efciency solar cells by band gap grading in Cu(In,Ga)Se_2 chalcopyrite semiconductors,* Solar Energy Materials & Solar Cells 67 (2001) 145 150.

[36] R. Klenk, J. Klaer, R. Scheer, M.Ch. Lux-Steiner, I. Luck, N. Meyer, U. R Klenk, *Solar cells based on $CuInS_2$—an overview*, Thin Solid Films 480–481 (2005) 509– 514.

[37] Marko Topič, Franc Smole, and Jože Furlan, *Band gap engineering in CdS/Cu(In,Ga)Se_2 solar cells,* J. Appl. Phys. 79, 8537 (1996).

[38] J. Kessler, C. Chityuttakan, J. Lu, J. Schöldström, L. Stolt, *Cu(In,Ga)Se_2 thin films grown with a Cu-poor/rich/poor sequence: growth model and structural considerations,* Prog. Photovolt: Res. Appl. 2003; 11:319–331.

[39] R. A. Mickelsen and W. S. Chen, “*High photocurrent polycrystalline thin-film CdS/CuInSe$_2$ solar cells*,” Applied Physics Letters, vol. 36, no. 5, pp. 371–373, 1980.

[40] Philip Jackson, Roland Würz, Uwe Rau, Julian Mattheis, Matthias Kurth, Thomas Schlötzer,Gerhard Bilger and Jürgen H. Werner, *High Quality Baseline for High Efficiency, Cu(In$_{1-x}$,Ga$_x$)Se$_2$ Solar Cells*, Prog. Photovolt. Res. Appl. 2007; 15:507–519.

[41] Ingrid Repins, Miguel A. Contreras, Brian Egaas, Clay De Hart, John Scharf, Craig L. Perkins, Bobby To and Rommel Noufi, *19.9%-efficient ZnO/CdS/ CuInGaSe$_2$ Solar Cell with 81.2% Fill Factor*, Prog. Photovolt: Res. Appl. 2008; 16:235–239.

[42] Miguel A. Contreras, Brian Egaas, K. Ramanathan, J. Hiltner, A. Swartzlander, F. Hasoon and Rommel Noufi, *Progress toward 20% efficiency in Cu(In,Ga)Se$_2$ polycrystalline thin-film solar cells*, Prog. Photovolt: Res. Appl. 7, 311–316 (1999).

[43] M. Nishitani, T. Negami, T. Wada, *Composition monitoring method in CuInSe$_2$ thin film preparation*, Thin solid films, 258 (1995) 313-316.

[44] N. Romeo, A Bosio, V. Canevari and R. Tedeschi, *Oscillating temperature selenization of Cu, Ga, In Elemental layers in a Se Vapour*, Photovoltaic Energy Conversion, IEEE, 1994, Page(s): 176 - 178 vol.1.

[45] Naoki Kohara, Takayuki Negami, Mikihiko Nishitani, Takahiro Wada, *Preparation of Device-Quality Cu(In,Ga)Se$_2$ Thin Films Deposited by Coevaporation with Composition Monitor*, Jpn. J. Appl. Phys. 34 (1995) pp. L1141-L1144.

[46] K. Sakurai, R. Hunger, R. Scheer, C. A. Kaufmann, A. Yamada, T. Baba, Y. Kimura, K. Matsubara, P. Fons, H. Nakanishi, S. Niki, *In situ diagnostic methods for thin-film fabrication: utilization of heat radiation and light scattering*, Prog. Photovolt: Res. Appl. 2004; 12:219–234.

[47] Kessler J, Schöldström J, Stolt L. *Rapid Cu(In,Ga)Se$_2$ growth using ‘end point detection´*, Photovoltaic Specialists Conference, IEEE, 2000, Page(s): 509 – 512.

[48] S. B. Zhang, Su-Huai Wei, Alex Zunger and H. Katayama-Yoshida, *Defect physics of the CuInSe$_2$ chalcopyrite semiconducto*r, Physical Review B 15 April 1998-Ii Volume 57, Number 16.

[49] Marianna Kemell, Mikko Ritala, and Markku Leskelä, *Thin Film Deposition Methods for CuInSe$_2$ Solar Cells*, Critical Reviews in Solid State and Materials Sciences, 30:1–31, 2005.

[50] Shigeru Niki, Miguel Contreras, Ingrid Repins, Michael Powalla, Katsumi Kushiya,Shogo Ishizuka and Koji Matsubara, *CIGS absorbers and processes*, Prog. Photovolt:Res. Appl. (2010) DOI: 10.1002/pip.969.

[51] C. J. Hibberd, E. Chassaing,W.Liu, D. B. Mitzi, D. Lincot, and A. N. Tiwari, *Non-Vacuum Methods for Formation of Cu(In,Ga)(Se,S)$_2$ Thin Film Photovoltaic Absorbers*, Prog. Photovolt:Res. Appl. (2010) DOI: 10.1002/pip.914.

[52] I. Dirnstorfer, Mt. Wagner, D.M. Hofmann, M.D. Lampert, F. Karg, and B.K. Meyer, *Characterization of Cu(In,Ga)(Se,S)$_2$ Thin Films III. In-Rich Layers*, phys. stat. sol. (a) 168, 163 (1998).

[53] Mt. Wagner, I. Dirnstorfer, D.M. Hofmann, M.D. Lampert, F. Karg, and B.K. Meyer, *Characterization of Cu(In,Ga)(Se,S)$_2$ Thin Films I. Cu-Rich Layers*, phys. stat. sol. (a) 167, 131 (1998).

[54] Billy J. Stanbery, *Copper Indium Selenides and Related Materials for Photovoltaic Devices*, Critical Reviews in Solid State and Materials Sciences, 27(2):73–117 (2002).

[55] A. Rockett and R. W. Birkmire, *CuInSe$_2$ for photovoltaic applications*, J. Appl. Phys. 70 (7), 1 October 1991.

[56] Susanne Siebentritt, Malgorzata Igalson, Clas Persson and Stephan Lany, *The electronic structure of chalcopyrites—bands, point defects and grain boundaries*, Prog. Photovolt:Res. Appl. (2010) DOI: 10.1002/pip.936.

[57] Michael Hafemeister, Susanne Siebentritt, Jürgen Albert, Martha Ch. Lux-Steiner, and Sascha Sadewasser, *Large Neutral Barrier at Grain Boundaries in Chalcopyrite Thin Films*, PRL 104, 196602 (2010).

[58] Rudmann, Dominik, *Effects of sodium on growth and properties of Cu(In,Ga)Se$_2$ thin films and solar cells*; PhD Dissertation ETH No 15576, Eidgenössische Technische Hochschule, Zürich, 2004.

[59] J. Schöldstrom, U. Zimmermann and M. Edoff, *Dynamic radiative properties of the Cu(In,Ga)Se$_2$ layer during the co-evaporation process*, Prog. Photovolt:Res. Appl. (2010) DOI: 10.1002/pip.931.

[60] S. Schorr, *Structural aspects of adamantine like multinary chalcogenides*, Thin Solid Films 515 (2007) 5985–5991.

[61] Z. V. Orlova, Trudy Vses. Magadanks Naucho-Issled. Int. Magadan, 2, 76 (1956).

[62] B. R. Pamplin and R. S. Feigelson, *Spray Pyrolysis of Complex Sphalerite Materials* , Mat. Res. Bull. Vol. 14, pp. 1-4, 1979.

[63] Min-Ling Liu, Fu-Qiang Huang, Li-Dong Chen, and I-Wei Chen, *A wide band gap p-type thermoelectric material based on quternary chacogenides of Cu$_2$ZnSnQ$_4$ (Q=S,Se)*, Applied physics letters 94, 202103 (2009).

[64] H. Hahn and H. Schulze, *Kurze Originalmitteilungen Ober ternire Selenide des Barium*, Die Naturwissensehaften 426 7. Mai 1965].

[65] W. Schfifer and R. *Nitsche, Tetrahedral quaternary chalcogenides of the type* Cu_2*-II-IV-*$S_4(Se_4)$, Mat. Res. Bull. Vol. 9, pp. 645-654, 1974. Pergamon Press, Inc.

[66] L. Guen, *Physical Properties of the Quarternary Chalcogenides* $Cu_2^IA^{II}B^{IV}X_4$, Mat. Res. Bull. Vol. 14, pp. 463-467, 1979.

[67] Hiroaki Matsushita, Takashi Maeda, Akinori Katsui, Takeo Takizawa, *Thermal analysis and synthesis from the melts of Cu-based quaternary compounds Cu-III-IV-*VI_4*,and* Cu_2*-II-IV-*VI_4, Journal of Crystal Growth 208 (2000) 416-422.

[68] I.D. Olekseyuk, L.D. Gulay , I.V. Dydchak , L.V. Piskach , O.V. Parasyuk , O.V. Marchuk, *Single crystal preparation and crystal structure of the* $Cu_2Zn/Cd,Hg/SnSe_4$ *compounds*, Journal of Alloys and Compounds 340 (2002) 141–145.

[69] J.M. Raulot, C. Domain, J.F. Guillemoles, *Ab initio investigation of potential indium and gallium free chalcopyrite compounds for photovoltaic application*, Journal of Physics and Chemistry of Solids, 66 (2005) 2019–2023.

[70] Hiroaki Matsushita, Akinori Katsui, *Materials design for Cu-based quaternary compounds derived from chalcopyrite-rule*, Journal of Physics and Chemistry of Solids, 66 (2005) 1933–1936.

[71] M. Altosaar, J. Raudoja, K. Timmo, M. Danilson, M. Grossberg, M. Krunks, T. Varema and E. Mellikov, $Cu_2ZnSnSe_4$ *Monograin Powders For Solar Cell Application*, Photovoltaic Energy Conversion, Conference Record of the 2006 IEEE 4th World Conference, 2006, pp. 468 – 470.

[72] Rachmat Adhi Wibowo, Woo Seok Kim, Eun Soo Lee, Badrul Munir, Kyoo Ho Kim, *Single step preparation of quaternary* $Cu_2ZnSnSe_4$ *thin films by RF magnetron sputtering from binary chalcogenide targets*, Journal of Physics and Chemistry of Solids 68 (2007) 1908–1913.

[73] G Suresh Babu, Y B Kishore Kumar, P Uday Bhaskar and V Sundara Raja,*Effect of post-deposition annealing on the growth of* $Cu_2ZnSnSe_4$ *thin films for a solar cell absorber layer*, Semicond. Sci. Technol. 23 (2008) 085023 (12pp).

[74] G Suresh Babu, Y B Kishore Kumar, P Uday Bhaskar and V Sundara Raja, *Growth and characterization of co-evaporated* $Cu_2ZnSnSe_4$ *thin films for photovoltaic applications*, J. Phys. D: Appl. Phys. 41 (2008) 205305 (7pp).

[75] G. Zoppi, I. Forbes, R. W. Miles, P. J. Dale, J. J. Scragg, and L. M. Peter, $Cu_2ZnSnSe_4$ *Thin Film Solar Cells Produced by Selenisation of Magnetron Sputtered Precursors*, Prog. Photovolt: Res. Appl. 2009; 17:315–319.

[76] I.V. Dudchak, L.V. Piskach, *Phase equilibria in the* Cu_2SnSe_3 *–*$SnSe_2$ *–ZnSe system*, Journal of Alloys and Compounds 351 (2003) 145–150.

[77] R. A. Wibowo, W. S. Kim, B. Munir and K. H. Kimd , *Growth and Properties of Stannite-Quaternary* $Cu_2ZnSnSe_4$ *Thin Films Prepared by Selenization of Sputtered Binary Compound Precursors*, Advanced Materials Research Vols. 29-30 (2007) pp. 79-82.

[78] Rachmat Adhi Wibowo, Eun Soo Lee, Badrul Munir, and Kyoo Ho Kim, *Pulsed laser deposition of quaternary* $Cu_2ZnSnSe_4$ *thin films*, phys. stat. sol. (a) 204, No. 10, 3373–3379 (2007).

[79] F. Hergert, R. Hock, *Predicted formation reactions for the solid-state syntheses of the semiconductor materials* Cu_2SnX_3 *and* Cu_2ZnSnX_4 *(X = S, Se),* starting from binary chalcogenides, Thin Solid Films 515 (2007) 5953–5956.

[80] M. Altosaar , J. Raudoja, K. Timmo, M. Danilson, M. Grossberg, J. Krustok, and E. Mellikov, $Cu_2Zn_{1-x}Cd_xSn(Se_{1-y}Sy)_4$ *solid solutions as absorber materials for solar cells,* phys. stat. sol. (a) 205, No. 1, 167–170 (2008).

[81] Hironori Katagiri, Kazuo Jimbo, Satoru Yamada, Tsuyoshi Kamimura, Win Shwe Maw, Tatsuo Fukano, Tadashi Ito and Tomoyoshi Motohiro, *Enhanced Conversion Efficiencies of* Cu_2ZnSnS_4*-Based Thin Film Solar Cells by Using Preferential Etching Technique*, Applied Physics Express 1 (2008) 041201.

[82] M. Grossberg, J. Krustok, K. Timmo, M. Altosaar, *Radiative recombination in* $Cu_2ZnSnSe_4$ *monograins studied by photoluminescence spectroscopy*, Thin Solid Films 517 (2009) 2489–2492.

[83] O. Volobujeva, J. Raudoja, E. Mellikov, M. Grossberg, S. Bereznev, R. Traksmaa, $Cu_2ZnSnSe_4$ *films by selenization of Sn–Zn–Cu sequential films*, Journal of Physics and Chemistry of Solids 70 (2009) 567–570 .

[84] O. Volobujeva, E. Mellikov, J. Raudoja, S.Bereznev, M. Pilvet, *Cu-In and Cu-Zn-Sn Films as Precursors for Production of* $CuInSe_2$ *and* $Cu_2ZnSnSe_4$, Thin Films, Mater. Res. Soc. Symp. Proc. Vol. 1165, 2009.

[85] L.A. Wahab , M.B. El-Den, A.A. Farrag, S.A. Fayek, K.H. Marzouk, *Electrical and optical properties of chalcopyrite compounds*, J. Phys. Chem. Solids (2009), doi:10.1016/j.jpcs.2008.12.018.

[86] Satoshi Nakamura, Tsuyoshi Maeda, and Takahiro Wada, *Electronic structure of stannite-type* $Cu_2ZnSnSe_4$ *by first principles calculations*, Phys. Status Solidi C, 1–5 (2009).

[87] X. Y. Shi, F. Q. Huang, M. L. Liu, and L. D. Chen, *Thermoelectric properties of tetrahedrally bonded wide-gap stannite compounds* $Cu_2ZnSn_{1-x}In_xSe_4$, Appl. Phys. Lett. 94, 122103 (2009).

[88] Shiyou Chen, X. G. Gong, Aron Walsh and Su-Huai Wei, *Crystal and electronic band structure of* Cu_2ZnSnX_4 *(X=S and Se) photovoltaic absorbers: First-principles insights*, Applied Physics Letters 94, 041903 (2009).

[89] C. Sevik and T. Çağın, *Assessment of thermoelectric performance of* Cu_2ZnSnX_4*, X=S, Se, and Te,* Applied Physics Letters 95, 112105 (2009).

[90] Shiyou Chen, X. G. Gong, Aron Walsh and Su-Huai Wei, *Electronic structure and stability of quaternary chalcogenide semiconductors derived from cation cross-substitution of II-VI and I-III-*VI_2 *compounds*, Physical Review B 79, 165211 (2009).

[91] Aron Walsh, Su-Huai Wei, Shiyou Chen and X. G. Gong, *Design Of Quaternary Chalcogenide Photovoltaic Absorbers Through Cation Mutation*, Photovoltaic Specialists Conference, IEEE, 2009, Page(s): 001875 – 001878.

[92] Alexey Shavel, Jordi Arbiol and Andreu Cabot, *Synthesis of Quaternary Chalcogenide Nanocrystals: Stannite* $Cu_2Zn_xSn_ySe_{1+x+2y}$, 4514 9 J. AM. CHEM. SOC. 2010, 132, 4514–4515.

[93] J. Krustok, R. Josepson, T. Raadik, M. Danilson, *Potential fluctuations in* $Cu_2ZnSnSe_4$ *solar cells studied by temperature dependence of quantum efficiency curves*, Physica B 405 (2010) 3186–3189.

[94] Teodor K. Todorov, Kathleen B. Reuter, and David B. Mitzi, *High-Efficiency Solar Cell with Earth-Abundant Liquid-Processed Absorber*, Adv. Mater. 2010, 22, E156–E159.

[95] J. Krustok, R. Josepson, M. Danilson, D. Meissner, *Temperature dependence of* $Cu_2ZnSn(Se,S)_4$ *monograin solar cells*, Solar Energy 84 (2010) 379–383.

[96] Suresh Babu G., Kishore Kumar Y.B., Uday Bhaskar P., Sundara Raja Vanjari, *Effect of Cu/(Zn+Sn) ratio on the properties of co-evaporated* $Cu_2ZnSnSe_4$ *thin films*, Solar Energy Materials & Solar Cells 94 (2010) 221–226.

[97] Hao Wei, Wei Guo, Yijing Sun, Zhi Yang, Yafei Zhang, *Hot-injection synthesis and characterization of quaternary* $Cu_2ZnSnSe_4$ *nanocrystals*, Materials Letters 64 (2010) 1424–1426.

[98] Clas Persson, *Electronic and optical properties of* Cu_2ZnSnS_4 *and* $Cu_2ZnSnSe_4$, Journal of Applied Physics 107, 053710 (2010).

[99] SeJin Ahn, Sunghun Jung, Jihye Gwak, Ara Cho, Keeshik Shin, Kyunghoon Yoon, Doyoung Park, Hyonsik Cheong, and Jae Ho Yun; *Determination of band gap energy (Eg) of* $Cu_2ZnSnSe_4$ *thin films: On the discrepancies of reported band gap values*, Applied Physics Letters 97, 021905 (2010).

[100] International Centre of Diffraction Data (ICDD). Datasheets: CZTSe: 04-010-6295; ZnSe: 04-007-4741; Cu_2SnSe_3: 03-065-4145; Cu_2Se01-071-4843; CuSe: 00-027-0185; SnSe: 04-004-4281; $SnSe_2$: 01-089-3197; Mo: 04-001-2734; Sn: 04-004-7743; Cu_3S: 03-065-4374; Zn: 04-008-6027; $Cu_{5.26}Sn_5$: 00-047-1575; Cu_5Zn_8: 00-025-1228; Cu: 00-103-1005; Cu_4Zn - 03-065-6066.

[101] Gwenae Gouadec, Philippe Colomban; *Raman Spectroscopy of nanomaterials: How spectra relate to disorder, particle size and mechanical properties*; Progress in Crystal Growth and Characterization of Materials 53 (2007).

[102] S. Larach, R. E. Shrader, and C. F. Stocker, *Anomalous Variation of band gap with composition in Zinc Sulfo and Seleno - Tellurides*, Physical Review, Volume 108, number 3, November 1, 1957.

[103] G. Marcano, C. Rincón, L. M. de Chalbaud, D. B. Bracho and G. Saánchez Pérez, *Crystal growth and structure, electrical, and optical characterization of the semiconductor* Cu_2SnSe_3, Journal of Applied Physics Volume 90, Number 4 15 August 2001.

[104] G. Suresh Babu, Y.B. Kishore Kumar, Y. Bharath Kumar Reddy, V. Sundara Raja, *Growth and characterization of* Cu_2SnSe_3 *thin films*, Materials Chemistry and Physics 96 (2006) 442–446.

[105] C. Xue, D. Papadimitriou, Y. S. Raptis, W. Richter, N. Esser, S. Siebentritt and M. Ch. Lux-Steiner, *Micro-Raman Study of Orientation Effects of CuSe-Crystallites on Cu-rich* $CuGaSe_2$ *Thin Films*, Journal of Applied Physics Volume 96, Number 4 15 August 2004.

[106] H.M. Pathan , C.D. Lokhande , D.P. Amalnerkar , T. Seth, *Modified chemical deposition and physico-chemical properties of copper(I) selenide thin films*, Applied Surface Science 211 (2003) 48–56.

[107] D. Pathinettam Padiyan, A. Marikani, K. R. Murali, *Electrical and Photoelectrical Properties of Vacuum Deposited SnSe Thin Film*s, Cryst. Res. Technol. 35 2000 8 949–957.

[108] Nicolas D. Boscher, Claire J. Carmalt, Robert G. Palgrave, Ivan P. Parkin, *Atmospheric pressure chemical vapour deposition of SnSe and* $SnSe_2$ *thin films on glass*, Thin Solid Films 516 (2008) 4750–4757.

[109] Shiyou Chen, X. G. Gong,bAron Walsh, and Su-Huai Wei, *Defect physics of the kesterite thin-film solar cell absorber* Cu_2ZnSnS_4, Applied Physics Letters 96, 021902 (2010).

[110] David Avellaneda, M. T. S. Nair, and P. K. Nair, Cu_2SnS_3 *and* Cu_4SnS_4 *Thin Films via Chemical Deposition for Photovoltaic Application*, Journal of The Electrochemical Society, 157 (6) D346-D352 (2010).

[111] H. Nukala, J. L. Johnson, A. Bhatia, E. A. Lund, W. M. Hlaing, M. M. Nowell, L. W. Rieth M. A. Scarpulla, *Synthesis of Optimized CZTS Thin Films for Photovoltaic Absorber Layers by Sputtering from Sulfide Targets and Sulfurization*, Mater. Res. Soc. Symp. Proc. Vol. 1268, 2010 Materials Research Society.

[112] J. Malaquias, Cu_2ZnSnS_4 *thin films for PV: Comparison of two growth methods,* Master Thesis, University of Aveiro, Aveiro 2010.

[113] Qijie Guo, Hugh W. Hillhouse, and Rakesh Agrawal, *Synthesis of Cu_2ZnSnS_4 Nanocrystal Ink and Its Use for Solar Cells*, J. AM. CHEM. SOC. 2009, 131, 11672–11673.

[114] A. Rockett, T. C. Lommason, L. C. Yang, H. Talieh, P. Campos and Joen A. Thorton, *Deposition of $CuInSe_2$ by the hybrid sputtering-and-evaporation method*, Photovoltaic Specialists Conference, 1988, Page(s): 1505 - 1509 vol.2.

[115] A. Rockett, A. Agarwal, L. C. Yang, E. Banda, G. Kensole, C. J. Kiely and H. Talieh, *Deposition of $CuInSe_2$ by the hybrid sputtering and evaporation method*, Photovoltaic Specialists Conference, 1990, IEEE, Page(s): 764 - 767 vol.1.

[116] M.F. Dumke, a, T.A. Tombrello, R.A. Wellerb, R.M. Housley and E.H. Cirlin, *Sputtering of the gallium-indium eutectic alloy in the liquid phase*, Surface Science Volume 124, Issues 2-3, 2 January 1983, Pages 407-422.

[117] VG Beshenkov, AB Grigoriev, VA Marchenko, *Momenta of particles emitted by target at intensive irradiation by low-energy ions*, Technical Physics, Vol 47, No 5 2002 pp 621-627.

[118] J Ränsch, S Hong, J Berndt and J Winter, *Investigation on interactions of fluid gallium with capacitively coupled rf-plasmas*, Plasma Phys. Control. Fusion 46 (2004) 1843-1853.

[119] R. Klenk, R. Menner, D. Cahen, H.W. Schock, *Improvement of $Cu(Ga,In)Se_2$ based solar cells by etching the absorber*, Photovoltaic Specialists Conference, 1990, IEEE, Page(s): 481 - 486 vol.1.

[120] R Caballero, C Guillen, *Optical and electrical properties of $CuIn_{1-x}GaxSe_2$ thin films obtained by selenization of sequentially evaporated metallic layers*, Thin Solid Films 431–432 (2003) 200–204.

[121] J. Tauc, R. Griforovici and A. Vancu; *Optical properties and electronic structure of Amorphous Germanium*; phys. Stat. sol. 15, 627 (1966).

[122] A.B. Murphy, *Band-gap determination from diffuse reflectance measurements of semiconductor films, and application to photoelectrochemical water-splitting*, Solar Energy Materials & Solar Cells 91 (2007) 1326–1337.

[123] A B Murphy, *Modified Kubelka–Munk model for calculation of the reflectance of coatings with optically-rough surfaces*, J. Phys. D: Appl. Phys. 39 (2006) 3571–3581.

[124] D. Abou-Ras, G. Kostorz, D. Bremaudb ,M. Kälin, F.V. Kurdesau, A.N. Tiwari, M.Döbeli, *Formation and characterisation of $MoSe_2$ for $Cu(In,Ga)Se_2$ based solar cells*, Thin Solid Films 480–481 (2005) 433– 438.

[125] Dieter Schmid, Martin Ruckh, Hans Werner Schock, *A comprehensive characterization of the interfaces in Mo/CIS/CdS/ZnO solar cell structures*, Solar Energy Materials and Solar Cells 41/42 (1996) 281-294.

[126] D. Abou-Ras , R. Caballero, C. A. Kaufmann, M. Nichterwitz, K. Sakurai , S. Schorr, T. Unold and H. W. Schock, *Impact of the Ga concentration on the microstructure of* $CuIn_{1-x}Ga_xSe_2$, phys. stat. sol. (RRL) 2, No. 3, 135–137 (2008).

[127] T.M. Friedlmeier, H. Dittrich, H.W. Schock, *Growth and characterization of* Cu_2ZnSnS_4 *and* $Cu_2ZnSnSe_4$ *thin films for photovoltaic applications,,* The 11th Conference on Ternary and Multinary Compounds, ICTMC-11, Salford, 8–12 September, 1997, p. 345.

[128] H. Katagiri, Cu_2ZnSnS_4 *thin film solar cells*, Thin Solid Films 480–481 (2005) 426–432.

[129] Dominique Drouin, Alexandre Réal Couture, Dany Joly, Xavier Tastet, Vincent Aimez,Raynald Gauvin, *CASINO V2.42—A Fast and Easy-to-use Modeling Tool for Scanning Electron Microscopy and Microanalysis Users*, SCANNING VOL. 29, 92–101 (2007).

[130] J. Bardeen, *Diffusion in binary alloys*, Physical Review, volume 76 number 9 1949, pp 1403-1405.

[131] *Thin Film Evaporation Guide Vacuum*, Vacuum Engineering & Materials, Inc. Los Gatos, California USA.

[132] G. Lermann, T. Bischof, A. Materny, and W. Kiefer, T. Kïmmell, G. Bacher, A. Forchel, and G. Landwehr, *Resonant micro-Raman investigations of the ZnSe–LO splitting in II–VI semiconductor quantum wires*, J. Appl. Phys. 81 (3), 1 February 1997.

[133] A.F. da Cunha, D. Rudmann, P.M.P. Salomé, F. Kurdesau, *Growth and Characterization of CIGS Solar Cells by RF Magnetron Sputtering with Continuous Se Evaporation and End Point Detection*, Proceedings of the 20th European Photovoltaic Solar Energy Conference and Exhibition, Barcelona, 6–10 June, 2005.

[134] Neelkanth G. Dhere, M. Cristina Lourenço, Ramesh G. Dhere and Lawrence L. Kazmerski, *Preparation and characterization of vacuum deposited* $CuInSe_2$ *thin films*, Solar Cells Volume 16, January-February 1986, Pages 369-380.

[135] Walter C. Hamilton, *Significance Tests on the Crystallographic R Factor*, Acta Cryst. (1965) 18, 502-510.

[136] J.L. Johnson, H. Nukala, E.A. Lund, W.M. Hlaing, A. Bhatia, L.W. Rieth, M.A. Scarpulla, *Effects of 2 phases, stress, and Na at the Mo/*Cu_2ZnSnS_4 *interface*, Mater. Res. Soc. Symp. Proc. Vol. 1268 2010 Materials Research Society 1268-EE03-03.

[137] http://www.menzel.de retrieved in the 20^{th} of June of 2008.

[138] L. Assmann, J.C. Bernède, A. Drici, C. Amory, E. Halgand, M. Morsli, *Study of the Mo thin films and Mo/CIGS interface properties*, Applied Surface Science, 246, 2005, 159–166.

[139] T. Wada, N. Koharab, S. Nishiwaki, T. Negami, *Characterization of the Cu(In,Ga)Se2/Mo interface in CIGS solar cells*, Thin Solid Films, 387, 2001, 118-122.

[140] H.S. Ullal and B. von Roeder, *Critical issues for commercialization of thin film PV technologies,*Solid State Technology,2008, 52-54.

[141] A. Čampa, J.Krč, J. Malmström b, M. Edoff, F. Smole, M. Topič, *The potential of textured front ZnO and flat TCO/metal back contact to improve optical absorption in thin Cu(In,Ga)Se$_2$ solar cells*, Thin Solid Films, 515, 2007, 5968–5972.

[142] K. Orgassa, H.W. Schock, J.H. Werner, *Alternative back contact materials for thin film Cu(In,Ga)Se$_2$ solar cells* , Thin Solid Films, 431, 2003, 387–391.

[143] T. J. Vink, M. A. J. Somers, J. L. C. Daams and A. G. Dirks, *Stress, strain, and microstructure of sputter-deposited MO thin films*, J. Appl. Phys., 70 (a), 1991, 4301-4308.

[144] John H. Scofield,, A. Duda, D. Albin, B.L. Ballard, P.K. Predecki, *Sputtered molybdenum bilayer back contact for copper indium diselenide-based polycrystalline thin-film solar cells*, Thin solid Films, 260, 1995, 26-31.

[145] Jonh A. Thorton, Joseh E. Greene; *Sputter deposition Processes in Handbook of Deposition Technologies for films and coatings*; Roitan F Bunshah; Noyes Publications, Second Edition, New Jersey, 1994.

[146] Mattox, D.M*; Handbook of Physical Vapor Deposition (PVD) Processing*; William Andrew Publishing/Noyes, 1998.

[147] U. Welzel, J. Ligot, P. Lamparter, A. C. Vermeulen and E. J. Mittemeijer, *Stress analysis of polycrystalline thin films and surface regions by X-ray diffraction*, J. Appl. Cryst. (2005). 38, 1–29.

[148] C. Guillén, J. Herrero, *Low-resistivity Mo thin films prepared by evaporation onto 30 cm × 30 cm glass substrates*, Journal of Materials Processing Technology, 143–144 (2003), 144–147.

[149] Joel Pantoja Enrıquez and Xavier Mathew; *Influence of the thickness on structural, optical and electrical properties of chemical bath deposited CdS thin films*; Solar Energy Materials & Solar Cells 76 (2003) 313–322.

[150] Kay Orgassa, Uwe Rau, Quang Nguyen, *Role of the buffer layer as an active optical element in Cu(In,Ga)Se$_2$ thin film solar cells*; Prog. Photovolt: Res. Appl., vol. 10, pp. 457-463, 2002.

[151] B. Malinowska, M. Rakib and G. Durand; *Ammonia recycling and cadmium confinement in chemical bath deposition of CdS thin layers*; Prog. Photovolt: Res. Appl., vol. 9, pp. 389-404, 2.

[152] N. Naghavi, D. Abou-Ras, N. Allsop, N. Barreau, S.Bücheler, A. Ennaoui, C.-H. Fischer, C. Guillen, D. Hariskos, J. Herrero, R. Klenk, K. Kushiya, D. Lincot, R. Menner, T. Nakada, C. Platzer-Björkman, S. Spiering, A.N. Tiwari and T. Törndahl, *Buffer layers and transparent conducting oxides for chalcopyrite* $Cu(In,Ga)(S,Se)_2$ *based thin film photovoltaics: present status and current developments*, Prog. Photovolt: Res Allp (2010), doi: 10.1002/pip.955.

[153] Chun-Sheng Jiang, F. S. Hasoon, H. R. Moutinho, H. A. Al-Thani, M. J. Romero and M. M. Al-Jassim; *Direct evidence of a buried homojunction in* $Cu(In,Ga)Se_2$ *solar cells*; Appl. Phys. Lett., Vol. 82, No. 1, 6 January 2003.

[154] S.N. Qiu, W.W. Lam, C.X. Qiu, I. Shih; $ZnO/CdS/CuInSe_2$*, photovoltaic cells fabricated using chemical bath deposited CdS buffe layer*, Applied Surface Science 113/l 14 (1997) 764-767.

[155] Anant H. Jahagirdar, Ankur A. Kadam and Neelkanth G. Dhere ,*Role of i-ZnO in Optimizing Open Circuit Voltage Of CIGS And Cigs Thin Film Solar Cells*, Photovoltaic Energy Conversion, 2006, IEEE, Page(s): 557 – 559.

[156] Z.C. Jin, L Hamberg and C. G. Granqvist, *Optical properties of sputter-deposited ZnO:AI thin films*, J. Appl. Phys. 64 (to). 15 November 1988.

[157] A.F. da Cunha, F. Kurdesau, D. Rudmann, P.M.P. Salome, *Performance comparison of hybrid sputtering/evaporation* $Cu(In_{1-x},Ga_x)Se_2$ *solar cells with different transparent conducting oxide window layers*, Journal of Non-Crystalline Solids 352 (2006) 1976–1980.

[158] Radhouane Bel Hadj Tahar, Takayuki Ban, Yutaka Ohya, and Yasutaka Takahashi, *Tin doped indium oxide thin films: Electrical properties*, J. Appl. Phys., Vol. 83, No. 5, 1 March 1998.

[159] F. Kurdesau, G. Khripunov, A.F. da Cunha, M. Kaelin, A.N. Tiwari, *Comparative study of ITO layers deposited by DC and RF magnetron sputtering at room temperature*, Journal of Non-Crystalline Solids 352 (2006) 1466–1470.

[160] Claes G. Granqvis, *Transparent conductors as solar energy materials: A panoramic review*, Solar Energy Materials & Solar Cells 91 (2007) 1529–1598.

[161] S. Sugai, T. Ueda, *High-pressure Raman spectroscopy in the layered materials* $2H\text{-}MoS_2$, $2H\text{-}MoSe_2$ *and* $2H\text{-}MoTe_2$, Physical Review B, Volume 26, Number 12, 15 December 1982.

[162] Nicolas D. Boscher, Claire J. Carmalt, Robert G. Palgrave, Ivan P. Parkin, *Atmospheric pressure chemical vapour deposition of SnSe and* $SnSe_2$ *thin films on glass*, Thin Solid Films 516 (2008) 4750–4757.

[163] H. R. Chandrasejhar, R. G. Humphreys, U. Zwick and M. Cardona, *Infrared and Raman spectra of the IV-VI compounds SnS and SnSe,* Physical Review B, volume 15, number 4, 15 february 1977.

[164] D Walsh, S Jandl and J Y Harbec, *Raman active modes of the layer crystal* $SnS_{1-x}Se_x$, 1980 J. Phys. C: Solid State Phys. 13 L125.

[165] S. Jiménez Sandoval, D. Yang, R. F. Frindt and J. C. Irwin, *Raman Study and lattice dynamics of sinle molecular layers of* MoS_2, Physical Review B, Vol. 44, Number 8, (1991), pp 3955-3962.

[166] J. Serrano, A. Cantarero, M. Cardona, N. Garro, R. Lauck, R.E. Tallman, T.M. Ritter, B.A. Weinstein, *Raman scattering in β-ZnS,* Phys Rev B 69 (2004) 014301.

[167] Louise S. Price, Ivan P. Parkin, Amanda M. E. Hardy and Robin J. H. Clark, *Atmospheric pressure chemical vapor deposition of tin sulfides (SnS,* Sn_2S_3*, and* SnS_2*) on glass,* Chem. Mater. 1999, 11, 1792 1799.

List of publications

During the time of work that lead to this thesis, the author has published the following papers which are referred in the text by their roman numerals:

[I] P.M.P. Salomé, P.A. Fernandes and A.F. da Cunha; *Morphological and Structural Characterization of* $Cu_2ZnSnSe_4$ *Thin Films Grown by Selenization of Elemental Precursor Layers*; Thin Solid Films, Volume 517, Issue 7, 2 February 2009, Pages 2531-2534.

[II] P.M.P. Salomé and A.F. da Cunha, *Incorporation of Ga in CIGS Absorber Layers Formed by RF-Magnetron Sputtering in Se Vapours*, Materials Science Forum, Vols. 587-588 (2008), pp 323-327.

[III] António F. da Cunha and Pedro M. P. Salomé; *CIGS absorber layers prepared by sputtering based methods; Thin Film Solar Cells*: Current Status and Future Trends; 2010 Nova Science Publishers, Inc; ISBN 978-1-61668-326-9.

[VI] P.A. Fernandes, P.M.P. Salomé, A.F. da Cunha, *Precursors' Order Effect on the Properties of Sulfurized* Cu_2ZnSnS_4, Semicond. Sci. Technol. 24 (2009) 105013 (7pp).

[V] P.M.P. Salomé, P. A. Fernandes, and A. F. da Cunha; *Influence of selenization pressure on the growth of* $Cu_2ZnSnSe_4$ *films from stacked metallic layers*; Phys. Status Solidi C 7, No. 3–4, 913– 916 (2010).

[VI] P.M.P. Salomé, P.A. Fernandes , A.F. da Cunha, J.P. Leitão, J. Malaquias, A. Weber, J.C González and M.I.N. da Silva, *Growth pressure dependence of* $Cu_2ZnSnSe_4$ *properties*; Solar Energy Materials & Solar Cells 94 (2010) 2176–218.

[VII] P.A. Fernandes, P.M.P. Salomé, A.F. da Cunha*; Growth and Raman scattering characterization of* Cu_2ZnSnS_4; Thin Solid Films, Volume 517, Issue 7, 2 February 2009, Pages 2519-2523.

[VIII] P.M.P. Salomé, J. Malaquias, P.A. Fernandes, and A.F. da Cunha, *Mo bilayer for thin film photovoltaics revisited*; 2010 J. Phys. D: Appl. Phys. 43 345501.

List of additional publications

During the time of work that lead to this thesis, the author has been involved in the following publications which were not the main topic of this thesis:

[i] J.P. Leitão, N.M. Santos, P.A. Fernandes, P.M.P. Salomé, A.F. da Cunha, J.C. González, F.M. Matinaga, *Study of optical and structural properties of* Cu_2ZnSnS_4 *thin films*, accepted in Thin Solid Films.

[ii] J. P. Leitão, N. M. Santos, P. A. Fernandes, P. M. P. Salomé, A. F. da Cunha, J. C. González, G. M. Ribeiro, and F. M. Matinaga, *Photoluminescence and electrical study of fluctuating potentials in* Cu_2ZnSnS_4 *based thin films*, submitted to Physics Review B.

[iii] P A Fernandes, P M P Salomé, and A F da Cunha, *A study of ternary* Cu_2SnS_3 *and* Cu_3SnS_4 *thin films prepared by sulfurizing stacked metal precursors*, J. Phys. D: Appl. Phys. 43 (2010) 215403 (11pp).

[iv] P. A. Fernandes , P. M. P. Salomé , and A. F. da Cunha; Cu_xSnS_{x+1} *(x = 2, 3) thin films grown by sulfurization of metallic precursors deposited by dc magnetron sputtering*; Phys. Status Solidi C 7, No. 3–4, 901– 904 (2010).

[v] P. A. Fernandes; P.M.P. Salomé; A.F. da Cunha; Björn-Arvid Schubert, Cu_2ZnSnS_4 *solar cells prepared with sulfurized dc-sputtered stacked metallic precursors*, accepted in Thin Solid Films.

[vi] P. A. Fernandes, P.M.P. Salomé and A. F. da Cunha, *Importance of Raman scattering in the study of polycrystalline* Cu_2ZnSnS_4 *films*; submitted to J. Phys. D: Appl. Phys.

List of figures

List of tables

Annex A: Selenium compounds Raman scattering peaks and relevant information

The following table shows the peaks of several Se-compounds that may be present as spurious phases in CZTSe thin films.

Table A-1: Position of Raman scattering peaks for several Se-compounds.

Compound	Structure	Peaks (cm^{-1})	Reference
CZTSe	kesterite/stannite	174, 195, 235	this thesis, [80]
ZnSe	zinc blende	206, 250	this thesis, [132]
Cu_2SnSe_3	cubic	180, 236	this thesis, [80]
$MoSe_2$	hexagonal	245, 282	this thesis, [161, 162]
$Cu_{2-x}Se$	cubic	91, 260-270	this thesis, [105]
SnSe	orthorhombic	33,71, 105,130,151	this thesis, [163]
$SnSe_2$	hexagonal	185	[162, 164]

The following chart shows the absorption coefficient for a CZTSe film grown over SLG. The values were used to fill the following table which shows the effective penetration depth mentioned in chapter 3.

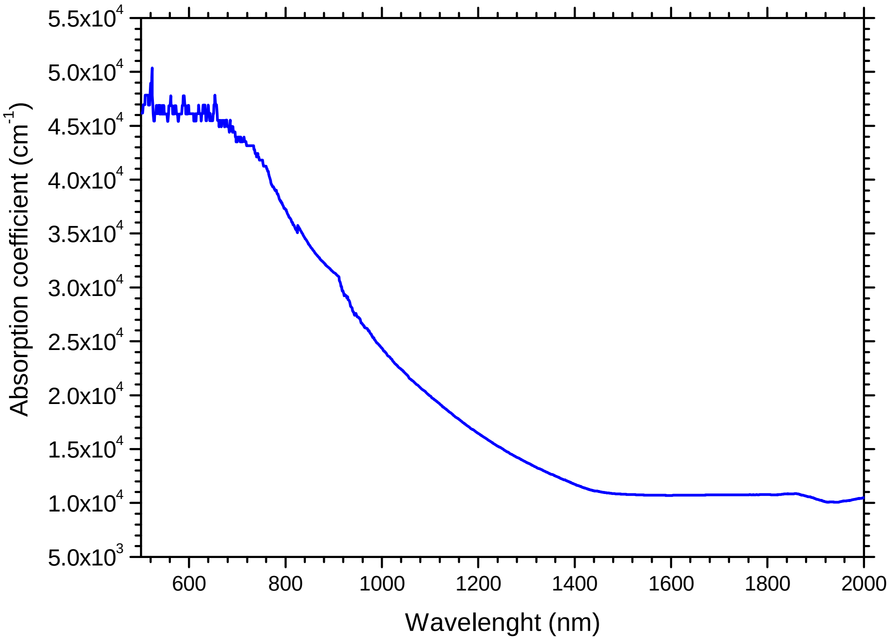

Figure A-1: Absorption coefficient versus wavelength for CZTSe.

Table A-2: Estimated values of the effective penetration depth for different wavelengths of CZTSe.

Wavelength (nm)	Absorption (cm^{-1})	Effective penetration depth (nm)
488	47287	106
514	46331	108
633	45727	109
785	38253	131
1035	22828	219

Annex B: Sulphur compounds Raman scattering peaks and relevant information

The following table shows the peaks of several S-compounds that may be present as spurious phases in CZTSe thin films.

Table B-1: Position of Raman scattering peaks for several S-compounds.

Compound	Structure	Peaks (cm^{-1})	Reference
CZTS	kesterite/stannite	287, 338, 370, 351	this thesis [I]
MoS_2	hexagonal	228, 384, 410	[165]
ZnS	cubic	276, 350	[166]
Cu_2SnS_3	tetragonal	297, 337, 352	[iii, iv]
Cu_2SnS_3	cubic	267, 303, 356	[iii, iv]
Cu_3SnS_4	orthorhombic	318	[iii, iv]
SnS	orthorhombic	160, 190, 219	[i , iii, iv]
SnS_2	hexagonal	314	[i,167]
Sn_2S_3	orthorhombic	52, 60, 307	[167]
$Cu_{2-x}S$	hexagonal	475	[i]

The following plot shows the absorption coefficient for a CZTS film grown over SLG [vi]. The values were used to fill the following table which shows the effective penetration depth mentioned in chapter 3.

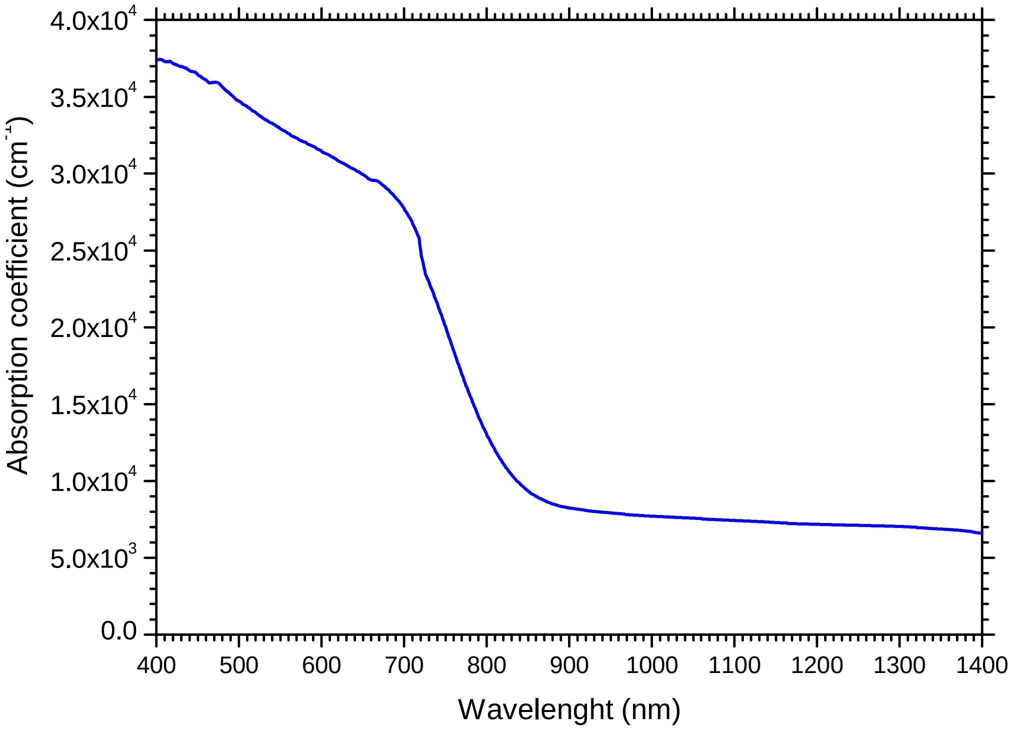

Figure B-1: Absorption coefficient versus wavelength for CZTS.

Table B-2: Estimated values of the effective penetration depth for different wavelengths of CZTS.

Wavelength (nm)	**Absorption (cm^{-1})**	**Effective penetration depth (nm)**
488	35254	142
514	34194	146
633	30465	164
785	14851	337
1035	7610	657

Short Curriculum Vitae

Name: Pedro Manuel Parracho Salomé

Place and date of birth: Ílhavo, 07-12-1983

Nationality: Portuguese

Contact information: Mobile phone: +351 966430059 email: psalome@ua.pt

Institutional Address: Campus Universitário de Santiago, Departamento de Física, Universidade de Aveiro, 3810-193 Aveiro, Portugal

Home Adress: Rua de Camões N.13 3830-152 Ílhavo, Portugal

Academic degrees: Diploma in Physics Engineering (5 years degree – “Licenciatura before the Bologne Process”), University of Aveiro Portugal, 2001- 2006, 1st of the class, mark 15/20.

Advanced Training Course in Energy Efficiency and Renewable Energies, 56 ECTS, (CFA EEER: Curso de formação avançada em eficiência energética e energias renováveis) 2008/2009.

Prizes: Best student award of physics engineering class 2006 University of Aveiro

Publications in international Journals:

A. F. da Cunha, F. Kurdzesau and P.M.P. Salomé, *Cu(In,Ga)Se*$_2$ *prepared by a 2 and 3-stage hybrid RF-magnetron sputtering and Se evaporation method: Properties and solar cell performance*, Materials Science Forum, Vols. 514-516, pp. 93-97, 2006.

A.F. da Cunha, F. Kurdesau, D. Rudmann and P.M.P. Salomé, *Performance comparison of hybrid sputtering/evaporation CIGS solar cells with different TCO window layers*, Journal of Non-Crystalline Solids 352 (2006) 1976-1980.

P.M.P. Salomé and A.F. da Cunha, *Incorporation of Ga in CIGS Absorber Layers Formed by RF-Magnetron Sputtering in Se Vapours,* Materials Science Forum Vols. 587-588 (2008) pp 323-327.

P.A. Fernandes, P.M.P. Salomé, A.F. da Cunha; *Growth And Raman Scattering Characterization Of* Cu_2ZnSnS_4, Thin Solid Films 517 (2009) 2519–2523.

P.M.P. Salomé, P.A. Fernandes and A.F. da Cunha; *Morphological and Structural Characterization of* $Cu_2ZnSnSe_4$ *Thin Films Grown by Selenization of Elemental Precursor Layers*; Thin Solid Films, 517(2009)2531–2534.

P.A. Fernandes, P.M.P. Salomé, A.F. da Cunha, *Precursors' Order Effect on the Properties of Sulfurized* Cu_2ZnSnS_4 *Thin Films*, Semicond. Sci. Technol. 24 (2009) 105013 (7pp).

P.A. Fernandes, P.M.P. Salomé, A.F. da Cunha; *A study of ternary* Cu_2SnS_3 *and* Cu_3SnS_4 *thin films prepared by sulfurizing stacked metal precursors*; J. Phys. D: Appl. Phys. 43 (2010) 215403.

P.M.P. Salomé, P.A. Fernandes , A.F. da Cunha, J.P. Leitão, J. Malaquias, A. Weber, J.C González and M.I.N. da Silva, *Growth pressure dependence of* $Cu_2ZnSnSe_4$ *properties*; Solar Energy Materials & Solar Cells 94 (2010) 2176–218.

P.M.P. Salomé, J. Malaquias, P.A. Fernandes, and A.F. da Cunha, *Mo bi-layer for thin film photovoltaics revisited,* J. Phys. D: Appl. Phys. 43 (2010) 345501 (7pp).

Publications in Conference Proceedings with refereeing:

A. F. da Cunha, D. Rudmann, P.M.P. Salomé and F. Kurdesau; *Growth and Characterization of CIGS Solar Cells by RF magnetron sputtering with continuous Se evaporation and End Point Detection*; Proceedings of the 20th EPVSEC, Barcelona, 2005.

P. A. Fernandes , P. M. P. Salomé , and A. F. da Cunha; Cu_xSnS_{x+1} *(x = 2, 3) thin films grown by sulfurization of metallic precursors deposited by dc magnetron sputtering*; Phys. Status Solidi C, 1–4 (2010) / DOI 10.1002/pssc.200982746.

P. M. P. Salomé, P. A. Fernandes, and A. F. da Cunha; *Influence of selenization pressure on the growth of* $Cu_2ZnSnSe_4$ *films from stacked metallic layers*; Phys. Status Solidi C, 1–4 (2010) / DOI 10.1002/pssc.200982748.

Under submission/ refereeing / accepted:

P.A. Fernandes, P.M.P. Salomé, A.F. da Cunha and Björn-Arvid, Schubert, Cu_2ZnSnS_4 *solar cells prepared with sulfurized dc-sputtered stacked metallic precursors,* accepted in Thin Solid Films.

J.P. Leitão, N.M. Santos, P.A. Fernandes, P.M.P. Salomé, A.F. da Cunha, J.C. González, F.M. Matinaga, *Study of optical and structural properties of* Cu_2ZnSnS_4 *thin films,* accepted in Thin Solid Films.

J. Malaquias, P.A. Fernandes, P.M.P. Salomé, A.F. da Cunha, *Assessment of the potential of tin sulphide thin films prepared by sulphurization of metallic precursors as cell absorbers*, under refereeing in Thin Solid Films.

Chapter in books:

António F. da Cunha and Pedro M. P. Salomé; CIGS absorber layers prepared by sputtering based methods; Thin Film Solar Cells: Current Status and Future Trends; 2010 Nova Science Publishers, Inc; ISBN 978-1-61668-326-9.